2013

Superfast three-dimensional (3D) shape measurement with binary defocusing techniques and its applications

Yajun Wang
Iowa State University

Superfast three-dimensional (3D) shape measurement with binary defocusing techniques and its applications

by

Yajun Wang

A dissertation submitted to the graduate faculty

in partial fulfillment of the requirements for the degree of

DOCTOR OF PHILOSOPHY

Major: Mechanical Engineering

Program of Study Committee:

Song Zhang, Major Professor

Ming-Chen Hsu

Yan-Bin Jia

James H. Oliver

Eliot H. Winer

Iowa State University

Ames, Iowa

2013

TABLE OF CONTENTS

LIST OF TABLES vii

LIST OF FIGURES viii

ACKNOWLEDGEMENTS xi

ABSTRACT xii

CHAPTER 1. GENERAL INTRODUCTION 1

1.1 Overview 1

1.2 Contributions 4

1.3 Dissertation Organization 7

1.4 Conclusion 8

CHAPTER 2. LITERATURE REVIEW 9

2.1 Relevant Literature on 3D Shape Measurement Techniques 9

2.1.1 Contact Techniques 10

2.1.2 Non-Contact Techniques 10

2.2 Relevant Literature on High-Speed 3D Shape Measurement 18

2.3 Relevant Literature on DFP System Calibration 21

2.4 Conclusion 23

CHAPTER 3. OPTIMAL PULSE WIDTH MODULATION FOR SINUSOIDAL FRINGE GENERATION WITH PROJECTOR DEFOCUSING 24

3.1 Abstract 24

3.2 Introduction 25
3.3 Principle 26
3.4 Experimental Results 29
3.5 Conclusion 31

CHAPTER 4. SUPERFAST MULTIFREQUENCY PHASE-SHIFTING TECHNIQUE WITH OPTIMAL PULSE WIDTH MODULATION 33

4.1 Abstract 33
4.2 Introduction 34
4.3 Principle 35
4.3.1 Three-Step Phase-Shifting Algorithm 35
4.3.2 Multifrequency Phase-Shifting (MFPS) Algorithm 36
4.3.3 Optimal Pulse Width Modulation (OPWM) Technique 38
4.4 Experimental Results 40
4.5 Conclusion 43

CHAPTER 5. 3D SHAPE MEASUREMENT WITH BINARY DITHERING TECHNIQUES 44

5.1 Abstract 44
5.2 Introduction 44
5.3 Phase-Shifting Algorithm 47
5.4 Binary Dithering Technique 47
5.5 Simulation Results 49
5.6 Experimental Results 52
5.7 Conclusion 54

CHAPTER 6. OPTIMAL FRINGE ANGLE SELECTION FOR DIGITAL FRINGE PROJECTION TECHNIQUE 56

6.1 Abstract 56

6.2 Introduction . . . 57
6.3 Phase-Shifting Algorithm . . . 58
6.4 Optimal Fringe Angle Selection . . . 59
6.5 Experimental Results . . . 61
6.6 Discussions . . . 64
6.7 Conclusion . . . 66

CHAPTER 7. ACCURATE CALIBRATION FOR 3D SHAPE MEASUREMENT SYSTEM USING A BINARY DEFOCUSING TECHNIQUE . . . 67

7.1 Abstract . . . 67
7.2 Introduction . . . 68
7.3 Principle . . . 70
7.3.1 Nine-Step Phase-Shifting Algorithm . . . 70
7.3.2 Absolute Phase Recovery with Gray Coding . . . 70
7.3.3 Establishment of the Relationship Between Absolute Phase and Depth . . . 71
7.3.4 Camera Parameters Estimation for x and y Calibration . . . 72
7.4 Experiments . . . 74
7.4.1 System Setup . . . 74
7.4.2 z Coordinate Calibration . . . 75
7.4.3 x and y Coordinate Calibration . . . 77
7.4.4 3D Shape Reconstruction . . . 78
7.5 Conclusion . . . 79

CHAPTER 8. DIGITAL MICROMIRROR TRANSIENT RESPONSE INFLUENCE ON SUPERFAST 3D SHAPE MEASUREMENT . . . 81

8.1 Abstract . . . 81
8.2 Introduction . . . 82

8.3 Principle 84
8.3.1 Two-Frequency Phase-Shifting Technique for Absolute Phase Retrieval 84
8.3.2 Fundamentals of the DLP Technology 85
8.3.3 Fundamentals of the Binary Defocusing Technique 86
8.4 Experiments 87
8.4.1 Experimental System Setup 87
8.4.2 Transient Response of the DMD with Binary Image Input 88
8.4.3 Coupling Effect 90
8.4.4 Phase Measurement Error Analysis 92
8.4.5 3D Shape Measurement for Static Object 94
8.4.6 Superfast 3D Shape Measurement 95
8.5 Conclusion 96

CHAPTER 9. 3D ABSOLUTE SHAPE MEASUREMENT OF LIVE RABBIT HEARTS WITH A SUPERFAST TWO-FREQUENCY PHASE-SHIFTING TECHNIQUE 99

9.1 Abstract 99
9.2 Introduction 100
9.3 Principle 102
9.3.1 Two-Frequency Phase-Shifting Technique for Absolute Phase Retrieval 102
9.3.2 Optimal Pulse Width Modulation (OPWM) Technique to Modulate High-Frequency Patterns 103
9.3.3 Error-Diffusion-Based Dithering Technique to Modulate Low-Frequency Patterns 104
9.4 Experiments 106
9.4.1 Experimental System Setup 106

9.4.2 Live and Fixed Rabbit Heart Preparation 108
9.4.3 Experimental Verification 109
9.5 Conclusion 113
CHAPTER 10. GENERAL CONCLUSION 117
10.1 Conclusions 117
10.2 Future Work 120
APPENDIX
EVALUATION OF PHASE QUALITY AT DIFFERENT DEPTHS FOR THE SBM, OPWM, AND DITHERING TECHNIQUES . . . 122
BIBLIOGRAPHY 127

LIST OF TABLES

Table 7.1 Measurement accuracy verification for four corner points. ♯ values are obtained from a high-accuracy digital caliper 79

LIST OF FIGURES

Figure 2.1 Classifications of 3D shape measurement techniques. 10

Figure 2.2 Principle of a stereo vision system. 12

Figure 3.1 Quarter-wave symmetric OPWM waveform. 27

Figure 3.2 Cross sections of SBM, SPWM and OPWM patterns. 29

Figure 3.3 Fringe patterns when $P = 120$ pixels. 30

Figure 3.4 3-D shape measurement of a sculpture. The first row shows the results when $P = 30$ pixels, and the second row shows the results when $P = 60$ pixels. 32

Figure 4.1 Quarter-wave symmetric OPWM waveform. 39

Figure 4.2 Captured fringe patterns and related phase maps. 40

Figure 4.3 3D result of the sculpture. 42

Figure 5.1 Binary dithering technique for 8-bit grayscale images. 46

Figure 5.2 Binary dithering techniques for a 8-bit grayscale image. 50

Figure 5.3 Simulation results of the proposed technique. 51

Figure 5.4 Phase errors with varying amount of defocusing by simulations. . 52

Figure 5.5 Phase errors with varying amount of defocusing by experiments. 53

Figure 5.6 Experimental results of measuring a complex 3D object. 55

Figure 6.1 Calculation of the optimal fringe angle. 61

Figure 6.2 Phase measurements using horizontal and vertical fringe patterns. 62

Figure 6.3 Results for the fringe patterns with the worst and the optimal fringe angles. 63
Figure 6.4 Sculpture results under different fringe angles. 65

Figure 7.1 Absolute phase $\Phi(x, y)$ vs. depth z for four arbitrary pixels. . . . 72
Figure 7.2 Calibration system setup. 74
Figure 7.3 Average depth error per plane using different curve fitting methods. 76
Figure 7.4 Example of four images of plane used in camera calibration set at different angles. 77
Figure 7.5 The measured diagonals. 78
Figure 7.6 3D shape measurement result of a step-height object. 80
Figure 7.7 3D shape measurement results of a complex object. 80

Figure 8.1 Optical switching principle of a digital micro-mirror device (DMD). 86
Figure 8.2 Binary defocusing patterns with different defocusing levels. . . . 87
Figure 8.3 The 3D shape measurement system. 88
Figure 8.4 Transient responses of the DMD of DLP LightCommander projector. 90
Figure 8.5 Captured low spatial frequency fringe patterns that shows the coupling effect under different conditions. 91
Figure 8.6 Cross sections of the fringe patterns shown in Fig. 8.5. 92
Figure 8.7 Phase measurement error under different different conditions. These figures show the same cross sections of the corresponding phase error maps. 93
Figure 8.8 Experimental results of a static object. 94
Figure 8.9 3D shape measurement results of the sculpture shown in Fig.8.10 under different conditions. 97
Figure 8.10 Experimental results of a pendular ball. 98

Figure 8.11 3D shape measurement results of a moving pendular ball under different conditions. 98

Figure 9.1 Quarter-wave symmetric OPWM waveform. 104

Figure 9.2 Comparison of Bayer dithering and error-diffusion dithering. . . 107

Figure 9.3 Photograph of live heart measurement system. 108

Figure 9.4 Wrapped phase maps for dead heart measurement. 110

Figure 9.5 Unwrapped phase map for dead heart measurement. 111

Figure 9.6 Comparison of different spectrum for fixed heart measurements. 112

Figure 9.7 Comparison of different spectrum for beating heart measurements. 115

Figure 9.8 Comparison of different speed for beating heart measurements. . 116

Figure A.1 The system setup. 123

Figure A.2 The captured patterns with the fringe period of $T = 18$ pixels when the board is at different depths. 124

Figure A.3 Experimental results of the SBM, OPWM and dithering techniques when the board is at different depths. 125

ACKNOWLEDGEMENTS

I would like to take this opportunity to express my thanks to those who helped me with various aspects of conducting research and the writing of this dissertation. First and foremost, thanks to Dr. Song Zhang for his guidance, patience and support throughout this research and the writing of this dissertation. His insights and attitudes for research have often inspired me and renewed my hopes for completing my graduate education.

I would like to thank my committee members for their efforts and contributions to this work: Dr. Ming-Chen Hsu, Yan-Bin Jia, James H. Oliver and Dr. Eliot H. Winer. Dr. Hsu and Dr. Jia provided a lot of valuable comments on the dissertation writing. Dr. Oliver helped me very much for his kind support and encouragement. And Dr. Winer has been instrumental in leading the Deere project and also helped me to formulate the dissertation writing. I would also like to thank Dr. Z.J. Wang and Dr. Abhijit Chandra for their valuable suggestions when serving in my committee.

I would like to thank my friends and colleagues in the lab. Laura Ekstrand helped me polish the dissertation writing. Beiwen Li provided a lot of help for the experiments. Thanks to Willima Lohry and Nikolaus Karpinsky for their valuable discussions and opinions to solve the technical problems. Also, I want to thank Tyler Bell, Morgan Hoke and other lab members for their helpful comments to my dissertation.

Finally, thanks goes to my family members for their consistent encouragement, support and love.

ABSTRACT

High-speed and high-accuracy three-dimensional (3D) shape measurement has enormous potential to benefit numerous areas including advanced manufacturing, medical imaging, and diverse scientific research fields. For example, capturing the rapidly pulsing wings of a flying insect could enhance our understanding of flight and lead to better and safer aircraft designs. Even though there are numerous 3D shape measurement techniques in the literature, it remains extremely difficult to accurately capture rapidly changing events.

Due to the potential for achieving high speed and high measurement accuracy, the digital fringe projection (DFP) techniques have been exhaustively studied and extensively applied to numerous disciplines. Real-time (30 Hz or better) 3D shape measurement techniques have been developed with DFP methods, yet the upper speed limit is typically 120 Hz, the refresh rate of a typical digital video projector. 120 Hz speed can accurately measure the slowly changing objects, such as human facial expressions, but it is far from sufficient to capture high-speed motions (e.g., live, beating hearts or flying insects). To overcome this speed limitation, the binary defocusing technique was recently proposed. Instead of using 8-bit sinusoidal patterns, the binary defocusing technique generates sinusoidal patterns by properly defocusing squared 1-bit binary patterns. Using this technique, kilo-Hertz (kHz) 3D shape measurement rate has been achieved. However, the binary defocusing technique suffers three major limitations: 1) low phase quality due to the influence of high-frequency harmonics; 2) smaller depth measurement range; and 3) low measurement accuracy due to the difficulty of applying existing calibration methods to the system with an out-of-focus projector.

The goal of this dissertation research is to achieve superfast 3D shape measurement by overcoming the major limitations of the binary defocusing technique. Once a superfast 3D shape measurement platform is developed, numerous applications could be benefited. To this end, this dissertation research look into verifying its value by applying to the biomedical engineering field. Specifically, this dissertation research has made major contributions by conquering some major challenges associated with the binary defocusing technique.

The first challenge this dissertation addresses is associated with the limited depth range and low phase quality of the binary defocusing method. The binary defocusing technique essentially generates quasi-sinusoidal fringe patterns by suppressing high-frequency harmonics through lens defocusing. However, the optical engines of the majority of digital video projectors are designed and optimized for applications with large depth of focus; for this reason, good quality sinusoids can only be generated by this technique within a very small depth region. This problem is exacerbated if the fringe stripes are wide. In that case, the high-frequency harmonics cannot be properly suppressed through defocusing, making it almost impossible to generate reasonable quality sinusoids.

To alleviate this problem associated with high-frequency harmonics, an optimal pulse width modulation (OPWM) method, developed in power electronics, is proposed to improve the fringe pattern quality. Instead of projecting squared binary structures, the patterns are optimized, in one dimension perpendicular to the fringe stripes, by selectively eliminating the undesired harmonics which affect the phase quality the most. Both simulation and experimental data demonstrate that the OPWM method can substantially improve the squared binary defocusing technique when the fringe periods are between 30-300 pixels. With this technique, a multi-frequency phase-shifting algorithm is realized that enables the development of a 556-Hz 3D shape measurement system capable of capturing multiple rapidly moving objects.

The OPWM technique is proved successful when the fringe stripe widths are within a certain range, yet it fails to achieve higher-quality fringe patterns when the desired fringe period goes beyond the optimal range. To further improve the binary defocusing technique, binary dithering techniques are proposed. Unlike the OPWM method, the dithering technique optimizes the patterns in both x and y dimensions, and thus can achieve higher-quality fringe patterns. This research demonstrates the superiority of this technique over all aforementioned binary defocusing techniques for high-quality 3D shape measurement even when the projector is nearly focused and the fringe stripes are wide.

The second challenge this dissertation addresses is accurately calibrating the DFP system with an out-of-focus projector. The binary defocusing technique generates quasi-sinusoidal patterns through defocusing, and thus the projector cannot be perfectly in focus. In the meantime, state-of-the-art DFP system calibration assumes that the projector is always in focus. To address this problem, a novel calibration method is proposed that directly relates depth z with the phase pixel by pixel without the requirement of projector calibration. By this means, very high accuracy depth measurement is achieved: for a depth measurement range of 100 mm, the root-mean-squared (rms) error is approximately 70 μm.

The third challenge this dissertation addresses is associated with the hardware limitation for the superfast 3D shape measurement technique. The high refresh rate of the digital micro-mirror device (DMD) has enabled superfast 3D shape measurement, yet a hardware limitation has been found once the speeds go beyond a certain range. This is because the DMD cannot completely turn on/off between frames, leading to coupling problems associated with the transient response of the DMD chip. The coupling effect causes substantial measurement error during high-speed measurement. Fortunately, since this type of error is systematic, this research finds that such error can be reduced to a negligible level by properly controlling the timing of the projector and the camera.

The superfast 3D shape measurement platform developed in this research could ben-

efit numerous applications. This research applies the developed platform to the measurement of the cardiac motion of live, beating rabbit hearts. The 3D geometric motion of the live, beating rabbit hearts can be successfully captured if the measurement speed is sufficiently fast (i.e. 200 Hz or higher for normal beating rabbit hearts). This research also finds that, due to the optical properties of live tissue, caution should be given in selecting the spectrum of light in order to properly measure the heart surface.

In summary, the improved binary defocusing techniques are overwhelmingly advantageous compared to the conventional sinusoidal projection method or the squared binary defocusing technique. We believe that the superfast 3D shape measurement platform we have developed has the potential to broadly impact many more academic studies and industrial practices, especially those where understanding the high-speed 3D phenomena is critical.

CHAPTER 1. GENERAL INTRODUCTION

1.1 Overview

Conventionally, two-dimensional (2D) or static 3D information are sufficient for many applications. However, in recent decades, there are increasing demands for accurately measuring 3D information of high-speed motions. High-speed and high-accuracy 3D shape measurement techniques are crucial to many application areas, such as medical imaging, quality control, and entertainment.

Medical imaging: The motion or shape changes of human organs, like heart or lung, can provide significant information of the condition of human health. With better knowledge on 3D geometric motions, doctors could diagnose the diseases more accurately and provide better treatments. For example, the electrocardiogram (ECG) signal is traditionally used for the diagnosis of heart-related diseases. The ECG signal only contains the electrical activity information, which might not be enough for the diagnosis of some complex cardiac arrhythmias. By using advanced high-speed 3D shape measurement technology, the mechanical information of the heart could also be obtained. Combining the electro-physiology and mechanics information, doctors or researchers could better understand the mechanisms of cardiac arrhythmias and thus find better treatments for the cardiac diseases.

Quality control: Quality control is of vital importance to the manufacturing companies. It can impact the financial success of a company by ensuring that only high-quality products are released and delivered to the customers. Quality control and in-line inspec-

tion can be streamlined with the advanced high-speed 3D shape measurement equipment. For example, for the complex task of assembling a modern car, since it consists of many parts that must fit together at the very end of the production line, the optimal performance of this process is guaranteed by quality control systems. The geometry of the metal parts are required to be checked in order to ensure that they have the correct dimensions, fit together and finally work reliably. For this purpose, high-speed and high-accuracy 3D shape measurement techniques could be applied to modeling the parts' surfaces during manufacturing production line in situ, and such information can then be used for the comparison against the designed values to ensure quality.

Entertainment: High-speed 3D shape measurement technology has the potential to transform the entertainment industry. Recently, after the huge success of the movie Avatar, 3D films have become the mainstream. With new 3D technologies, 3D models can be more easily created with low cost and high speed. In addition, 3D technology has also been extensively used in creating and interacting with video games, like the Microsoft Kinect. Because the user can control a world that looks like his or her own, 3D video games could provide a deeper feeling of interaction.

Over the past decades, numerous high-speed 3D shape measurement techniques have been developed. Time-of-flight (TOF) is one of the popular high-speed techniques that are commercially successful. However, the achieved depth accuracy, spatial resolution and the measurement speed are usually not high due to the fundamental limitations of the TOF technique. Utilizing the advanced digital cameras for 3D reconstruction, the stereo vision technique has the potential for very high speed measurement since it could reach the camera's maximum frame rate (Lazaros et al., 2008). However, the measurement accuracy of this method is still not very high due to the classical challenging correspondence establishment problem, especially for measuring objects without rich texture information. To overcome these limitations of the stereo vision technique, some active techniques have been developed, such as the speckle projection method which has

shown its potential for very high speed 3D shape measurement (Schaffer et al., 2011, 2013). However, it is difficult for this technique to reach the camera-pixel level of spatial resolution due to the area correlation requirement of this technique.

Structured light techniques increase the measurement capability by actively projecting known structured patterns onto the objects, and thus the correspondence can be established easily with high accuracy. However, conventional structured light techniques are limited with their spatial resolution to be larger than both the projector and the camera pixel. Since fringe projection techniques utilize the patterns that have intensities that vary continuously from point to point , they boost the structured light techniques from projector-pixel resolution to camera-pixel resolution. Because of the advantages of using digital projectors and the potential for high-speed, high-accuracy 3D shape measurement, the digital fringe projection (DFP) techniques have been recently extensively studied and increasingly employed in many fields (Zhang, 2010b). Real-time (30 Hz or better) 3D shape measurement systems have been developed with DFP methods (Zhang and Huang, 2006a; Weise et al., 2007; Liu et al., 2010; Li et al., 2010), yet the upper speed limit is typically 120 Hz, the refresh rate of a typical digital video projector. 120 Hz speed can accurately measure the slowly changing objects, such as human facial expressions, but it is far from sufficient to capture high-speed motions such as the beating hearts and flying insects. To overcome this speed limitation, the binary defocusing technique was recently proposed (Lei and Zhang, 2009). Instead of using 8-bit sinusoidal patterns, the binary defocusing technique generates sinusoidal patterns by properly defocusing squared 1-bit binary patterns. Using the binary defocusing technique, kilo-Hertz (kHz) 3D shape measurement rate has been achieved (Zhang et al., 2010). However, the squared binary defocusing technique suffers the following three major limitations: 1) low phase quality due to the influence of high-frequency harmonics; 2) smaller depth measurement range due to the stringent requirement of sinusoidal fringe patterns through defocusing; and 3) low measurement accuracy due to the difficulty of applying existing calibration methods

to the system with an out-of-focus projector.

In order to achieve superfast 3D shape measurement with high accuracy, these limitations or challenges of the binary defocusing technique must be conquered. Meanwhile, when operating under high speed, there will be problems associated with the hardware limitations especially for the digital projector. To address these challenges, this dissertation presents our novel research on the improvements of the squared binary defocusing technique, the development of the superfast 3D shape measurement platform and its application in biomedical engineering field to precisely capture live, beating rabbit hearts.

1.2 Contributions

This dissertation research has made breakthroughs in high-speed and high-accuracy 3D shape measurement using DFP methods with the binary defocusing technique. Specifically, this dissertation research has made the following major contributions:

1. **An optimal pulse width modulation (OPWM) method to improve the measurement quality of the squared binary defocusing technique.** The squared binary defocusing technique can significantly simplify 3D shape measurement system development, and drastically improve its speed. However, the measurement range is limited because the projector can only be properly defocused in a small range. Meanwhile, it is very difficult for this technique to achieve high-quality measurement when the fringe stripes are wide (more than 30 pixels). To alleviate this problem, an OPWM method is proposed by selectively eliminating high-frequency harmonics induced by a squared binary pattern. By this means, better sinusoidal fringe patterns can be generated with a small amount of defocusing even for wide fringe patterns. Simulation and experiments have verified the success of this proposed technique. This fundamental theory of this work has been published in the Journal of Optics Letters (Wang and Zhang, 2010), and the thor-

ough comparison between the OPWM method and the squared binary method has been published in the Journal of Applied Optics (Wang and Zhang, 2010, 2012a).

2. **A multi-frequency phase-shifting (MFPS) algorithm to measure multiple rapidly moving objects.** It is challenging for the squared binary defocusing technique to realize a multi-frequency phase-shifting (MFPS) algorithm because it is difficult to simultaneously generate high-quality sinusoidal fringe patterns with different periods under the same amount of defocusing. Since our proposed OPWM method has the merits of generating different breadths of fringe patterns even with nearly focused projector, we propose to realize an MFPS algorithm utilizing the OPWM technique. We successfully developed a 556 Hz 3D shape measurement system utilizing a three-frequency phase-shifting algorithm for simultaneously measuring multiple rapidly moving objects. This work has been published in the Journal of Optics Express (Wang and Zhang, 2011).

3. **The binary dithering techniques for further improvement of 3D shape measurement quality.** The previously proposed binary defocusing technique and its variations (e.g., OPWM) have proven successful for high-quality three-dimensional (3D) shape measurement when fringe stripes are within a certain range, yet they also fail to achieve high-quality measurement when fringe stripes are very wide (more than 300 pixels). To conquer this challenge, the binary dithering techniques are proposed. Both simulation and experimental results showed the phase error is always less than 0.6% even when the fringe stripes are wide (about 600 pixels) and the projector is nearly focused. This work has been published in the Journal of Applied Optics (Wang and Zhang, 2012b).

4. **An optimal fringe angle selection method for DFP technique.** The existing DFP systems mainly either use horizontal or vertical fringe patterns for three-dimensional (3D) shape measurement. However, our research found that these

two fringe directions are usually not optimal where the phase change is the largest to a given depth variation, i.e., the sensitivity is not the highest. Therefore, a novel and efficient method is proposed to determine the optimal fringe angle by projecting a set of horizontal and vertical fringe patterns onto a step-height object and by further analyzing two resultant phase maps. Our research demonstrated the existence of the optimal angle and the success of the proposed optimal angle determination method. This work has been published in the Journal of Applied Optics (Wang and Zhang, 2013).

5. **A novel calibration method for the binary defocusing technique with high accuracy.** Due to the use of an out-of-focus projector, the existing calibration methods can not be directly adopted for this technique since they typically require the projector to be in focus or nearly in focus.To address this challenge, a novel calibration method is proposed that relates depth z with the phase pixel by pixel without the requirement of projector calibration. And the camera is calibrated using the standard flat checkerboard method. Since this method does not require estimation of the projector's parameters, it can be adopted for any phase measurement systems including those employing out-of-focus projectors. Experimental results demonstrated that the proposed method can achieve very high accuracy depth measurement: for a depth measurement of 100 mm, the root-mean-squared (rms) error is approximately 70 μm. This work has been published in the Journal of Optics and Lasers in Engineering (Merner et al., 2013).

6. **A method to solve the problems associated with the hardware limitations when conducting superfast 3D shape measurement.** The high refresh rate of the digital micro-mirror device (DMD) has enabled superfast 3D shape measurement using the binary defocusing technique, yet a hardware limitation has been found once the speeds go beyond a certain range. The transient response of

the DMD induces a coupling effect (i.e., two neighboring patterns blend together) that may cause substantial measurement error. Fortunately, this type of error is systematic, and our research find that such error can be reduced to a negligible level by properly controlling the timing of the projector and the camera. A paper about this work has already been submitted to the Journal of Optics and Lasers in Engineering.

7. **A superfast 3D shape measurement platform with the application to the dynamic shape measurement of live rabbit hearts.** Utilizing the proposed binary defocusing techniques such as the OPWM and dithering techniques, a superfast 3D shape measurement platform is developed with a two-frequency binary phase-shifting algorithm. This research further applies the platform to the measurement of the cardiac motion of live, beating rabbit hearts. The 3D geometric motion of the live rabbit hearts can be successfully captured if the measurement speed is sufficiently fast. This research also finds that, due to the optical properties of live tissue, caution should be given in selecting the spectrum of light in order to properly measure the heart surface. This work has been published in the Journal of Optics Express (Wang et al., 2013a).

1.3 Dissertation Organization

Chapter 2 presents the basic principles for some popular 3D shape measurement techniques especially those with high-speed potentials. Since the digital fringe projection (DFP) system calibration is crucial for high-accuracy 3D shape measurement, the literature review on system calibration is also conducted.

Chapter 3-5 presents the methodologies we developed to improve the fringe quality of the binary defocusing technique including the OPWM technique (Chapter 3), the dithering technique (Chapter 5), and the multi-frequency phase-shifting technique (Chapter

4). Chapter 6 describes a method to further improve the DFP method by determining the optimal fringe angle. Chapter 7 presents a novel method for accurately calibrating the DFP system even with an out-of-focus projector.

Chapter 8 discusses one of the problems associated with the hardware itself, i.e., the DMD, that enables the superfast 3D shape measurement. However, the transient response of the DMD could introduce measurement error when the speeds go beyond a certain range. This chapter will discuss a viable solution to overcome this problem.

The high-speed superfast 3D shape measurement platform has many applications, Chapter 8 presents one of the applications that we explored: measuring the live rabbit hearts for cardiac mechanics study. Finally, Chapter 10 summarizes the contributions of this research and proposes the future research directions.

1.4 Conclusion

High-speed and high-accuracy 3D shape measurement is of great importance in numerous application areas. Though many techniques have been developed, it remains extremely difficult to capture rapidly changing events. The recently proposed binary defocusing technique has the potential for high-speed and high-accuracy 3D shape measurement. However, it still has several major limitations. This dissertation research work has proposed some methods to overcome some of these limitations and to improve the robustness and accuracy of the binary defocusing technique. Meanwhile, by solving the problem associated with hardware limitations under the high-speed operation, a superfast 3D shape measurement platform is successfully developed. This dissertation research also applies the developed platform to the biomedical engineering field by precisely measuring live, beating rabbit hearts.

CHAPTER 2. LITERATURE REVIEW

Driven by the increasing demands for high-speed and high-accuracy 3D shape measurement, numerous techniques have been developed over the past decades. However, only a few methods can simultaneously achieve high speed and high accuracy. Even though each technique comes with its own advantages to meet particular application needs, it also carries its own limitations. This chapter presents the basic principles of some extensively adopted 3D shape measurement techniques with a focus on high-speed 3D measurement techniques since they are closely related to this dissertation research. In the meantime, since the calibration process is crucial for high-accuracy measurement, this chapter also reviews the literature on 3D shape measurement systems with the digital fringe projection (DFP) techniques that was utilized in this dissertation research.

2.1 Relevant Literature on 3D Shape Measurement Techniques

In reverse engineering, the first step of creating a digital replica of a real-world 3D object could be realized through 3D shape measurement. Real objects can be as small as cells or as large as buildings. The different requirements of object properties (e.g., size, materials) have driven the development of various techniques for acquiring 3D geometrical shape information.

A well-established classification of 3D shape measurement techniques is to divide them into two categories, contact and non-contact methods; and the non-contact 3D techniques

can be further classified into two main categories, passive and active techniques. This section will give an overview of the techniques under each category.

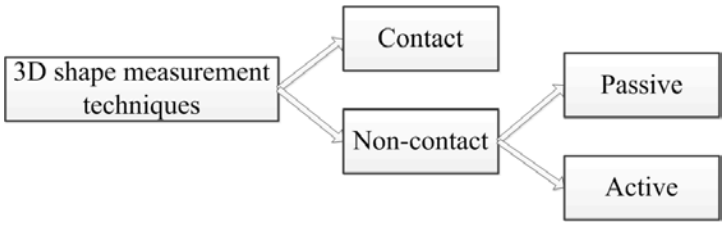

Figure 2.1 Classifications of 3D shape measurement techniques.

2.1.1 Contact Techniques

For a contact 3D shape measurement technique, the system generally probes the target through physical touch when the measured object is in contact with or resting on a flat surface plane. If the measured object is not flat or cannot rest stably on a flat surface, it will be then supported or held firmly in place by a fixture. A coordinate measuring machine (CMM) is a representative example of using contact 3D shape measurement techniques. CMMs have been widely used in the manufacturing area because they can provide very high-accuracy measurements. However, due to the requirement of contacting with the measured object, one disadvantage of CMM technique is that it might modify or damage the object surface. This issue could be very significant if it is used to measure delicate or valuable objects such as historical artifacts. The other disadvantage of CMM technique is that they are relatively slow due to the physical movement of the robot arms and due to the reality that it only measures one point at a time.

2.1.2 Non-Contact Techniques

To overcome the limitations of contact techniques, numerous non-contact methods have been developed. Since there is no requirement for physical touch, these techniques can be used to measure soft or deformable objects and thus substantially expand their

application areas. The non-contact 3D shape measurement techniques can be broken down further into passive and active methods.

2.1.2.1 Passive Techniques

The passive techniques do not actively emit any kind of radiation, but rather rely on the ambient radiation for the depth information recovery. Two representative techniques in this category are introduced: depth from defocus (DFD) and stereo vision.

(1) Depth from Defocus

The majority of 3D shape measurement techniques assume that all depths of a measured scene are in focus simultaneously. However, in a practical optical system, only finite depths are in focus. Some areas of the captured image are sharp and in focus while others are blurred or out of focus. In other words, the points in the scene of object are imaged with different amount of defocusing/blurring. If the blurring due to defocus can be quantified, the defocus information can be used to recover the depth or the shape. Since the amount of blur depends on depth of the scene, this technique is called shape from defocus or depth from defocus (Subbarao and Surya, 1994; Pentland, 1987).

To obtain a unique reconstruction of the scene, one defocused image is not sufficient unless additional information is available. Generally, two or more defocused images obtained with different focus settings are used (Favaro and Soatto, 2005). Since no active illumination is used and no active control on the focus setting is performed for the DFD technique, some real-time systems have been developed (Watanabe et al., 1996; Ben-Ari and Raveh, 2011). However, since this technique requires strong texture information for analysis of blurring effects, its resolution and sensitivity are usually not high (Schechner and Kiryati, 1998), resulting in limited application areas.

(2) Stereo Vision

Stereo vision techniques are based on the analysis of two or more images of the same scene, seen from different perspectives. When two cameras view a 3D scene from

two distinct positions, there are a number of geometric relations between the 3D points and their projections onto the 2D images that lead to constraints between the image points. These relations are derived based on the assumption that the cameras can be approximated by the pinhole camera model; and the geometric constraint used is usually called epipolar geometry.

To determine to geometric constraint and further obtain 3D information, the camera parameters (extrinsic parameters: position, orientation; intrinsic parameters: focal length, optical center, and distortion parameters) need to be determined through calibration. In general, this step is performed before any measurement, using a number of particular calibration scenes, such as checkerboards to estimate those parameters. If the corresponding points on different images are known, the 3D point can be reconstructed from two or more 2D images using triangulation.

Figure 2.2 illustrates the principle of a stereo vision technique. If the points X_L and X_R are known, their projection lines are also known. If those two image points correspond to the same 3D point X, the projection lines must intersect precisely at X. This indicates that X can be calculated from the coordinates of the two image points given the geometric constraint information for the cameras.

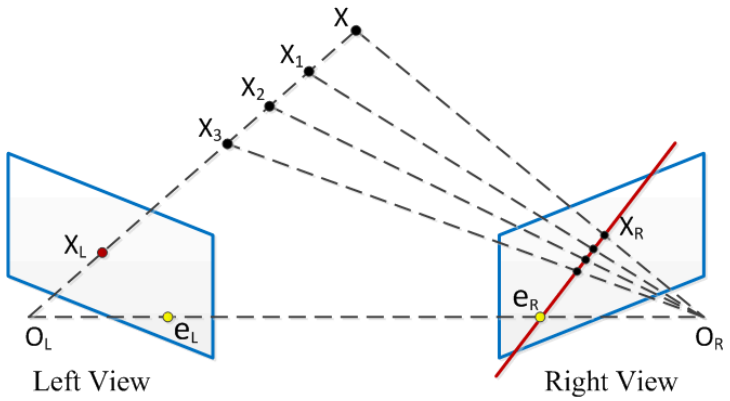

Figure 2.2 Principle of a stereo vision system.

Camera calibration has been extensively studied over a long period of time (Tsai,

1987; M.A.Sidahmed and Boraie, 1990; Weng et al., 2010; T.A.Clarke and J.G.Fryer, 1998; Zhang, 2000). The camera is typically modeled as a pinhole model that relates the 3D points, (X, Y, Z), to the 2D image point, (u, v), through its intrinsic and extrinsic parameters. Mathematically, the relationship can be described as,

$$s \begin{bmatrix} u \\ v \\ 1 \end{bmatrix} = \begin{bmatrix} \alpha & \gamma & u_0 \\ 0 & \beta & v_0 \\ 0 & 0 & 1 \end{bmatrix} \begin{bmatrix} R & t \end{bmatrix} \begin{bmatrix} X \\ Y \\ Z \\ 1 \end{bmatrix}, \tag{2.1}$$

where (u_0, v_0) is the coordinate of the principle point, α and β the focal lengths of the lens in image u and v axes, and these describe the intrinsic parameters of the camera. (R, t) describes the extrinsic parameters: R is a 3×3 rotation matrix and t is the 3×1 translation vector.

From two camera images, if the correspondence is established, four linear equations represent an over-determined set of equations that can be solved in the least square sense to yield the (X, Y, Z) information for a 3D point. The measurement accuracy is associated with multiple factors: the camera resolution, the calibration accuracy, and the ability to accurately determine correspondence.

The main advantages of this technique are the low cost of the hardware and potential for high-speed measurement, since only two cameras are required. However, the major problem of this kind of technique is the computation cost of the corresponding feature points for 3D reconstruction. Due to the fact that large regions with constant luminance exist (e.g. untextured regions or repetitive patterns), there will be problems for uniquely matching two points.

2.1.2.2 Active Techniques

Merely relying on the ambient radiation, passive techniques might fail to provide high-accuracy measurement results if the surface texture is not varying drastically from one

point to another. To overcome these limitations, active techniques have been developed by emitting some kind of radiation onto the objects for correspondence establishment. By capturing and analyzing the interaction between the object and the radiation, the coordinates of the points or 3D information can be obtained. Several extensively used active techniques, including time of flight (TOF), laser triangulation and structured light, are introduced as follows.

(1) Time of Flight (TOF)

TOF is an optical analogy to a bat's ultrasonic system rather than a human's stereo vision (Kolb et al., 2010; Filiberto et al., 2009). TOF cameras involve active illumination, and deliver range (or depth) by measuring the time needed for a light signal to travel from the camera light source to the scene and back to the camera sensor. Present TOF cameras are based on the continuous emission of a periodic signal. By modulating the phase at a constant frequency, and then recording the phase with the detector, the time can be accurately determined using the phase difference. The key component is an array sensor which can measure both the intensity and distance information to the target pixel wise in parallel without scanning (Lange and Seitz, 2001).

Since the projection and recorded units are from the same view angle, TOF technique does not have the occlusion problem; and the hardware system is very compact comparing with other techniques such stereo vision systems where a certain base line distance is required for two cameras. However, the major limitation of this technique is that the resolution of the detector is usually low, because special sensors need to be designed with the requirement of measuring both intensity and distance information.

(2) Laser Triangulation

Laser triangulation system can achieve higher spatial resolution than the TOF system. In general, a laser triangulation system contains a laser, a detector and a lens in front of the detector to focus the laser beam onto the detector. When conducting measurement, the laser emits a light onto the surface of the measured object. Then the laser beam

is reflected from the surface and falls on the detector through the lens. Based on the position of the beam on the detector and its emitting location, the depth z from the sensor to the target surface can be calculated through triangulation. To speed up the acquisition process, in most cases a laser stripe, instead of a single laser dot, is swept across the object (Franca et al., 2005). The most critical element in such a system is the detector, which can be of the two forms: a position sensitive device (PSD) or charge coupled device (CCD). PSD triangulation has been around for more than 20 year, but it is susceptible to spurious reflections from changing surface conditions, which can reduce the measurement accuracy. In contrast, the most advanced CCD technology can overcome many of the limitations of the PSD technology.

The accuracy of laser triangulation systems is relatively high (up to less than a micrometer). In addition, the measurement range is large allowing such systems to fulfill a variety of application requirements (e.g., large building measurements). However, using this kind of scanning systems to scan objects in motion will be very difficult because only one point or one line can be measured at a time.

(3) Structured Light

Structured light method is quite similar to the passive stereo vision technique, except that in the fundamental system, one of the cameras is replaced with a projecting unit. Typically, the projected patterns consist of many stripes at once, or of arbitrary structures (Salvi et al., 2004). If observed from a different viewpoint from the projection, the pattern appears geometrically distorted due to the object surface shape (Gorthi and Rastogi, 2010). The displacement of the stripes allows for an exact retrieval of the 3D coordinates of the object's surface.

Since the structured light system uses the projector to project certain types of designed patterns, it is easy to identify the correspondence between the images from different views regardless of the natural surface texture; and thus it overcomes the difficult correspondence problem in a passive stereo vision system. Meanwhile, the structured

light method is capable of high-speed 3D shape measurement since the computation cost is also substantially reduced due to the actively projected patterns; and, instead of scanning one point or one line at a time, multiple points or the entire field of view can be measured at once. This reduces or eliminates the problem of distortion from motion. Furthermore, this technique can provide relatively high-accuracy measurement since correspondence can be accurately determined (Zhang, 2010b).

Depending on the information used for correspondence establishment, the structured light techniques can be further divided into two major categories: intensity-based and phase-based techniques.

The intensity-based methods use the grayscale values or ratios for the correspondence identification. Binary coding is one of the well-known intensity-based methods that projects multiple binary coded patterns (Posdamer and Altschuler, 1982; Inokuchi et al., 1984). Since only two illumination levels ('0' and '1') are used, it is relatively robust to the noise for the codeword identification. However, the resolution is not very high because the projection stripe is always larger than one projector's and camera's pixel. Moreover, it typically requires many (> 3) patterns to achieve high resolution, which slows down the measurement speed. To improve the measurement speed, multi-level gray coding and intensity ratios methods have been proposed to reduce the number of required patterns for 3D reconstruction (Caspi et al., 1998; Carrihill and Hummelr, 1985; Horn and Kiryati, 1999). The intensity ratio method uses all grayscale levels and the intensity ratio is used for correspondence identification. Though the measurement speed can be improved, the intensity-based methods are highly sensitive to camera noise and image defocus.

For the phase-based techniques or fringe projection techniques, instead of using the intensity information, the depth or 3D information is extracted from the phase values encoded in the fringe patterns. A popular method to obtain the phase information is by using several fringe patterns with certain phase shifts, which is called phase-shifting

techniques (Srinivasan et al., 1984; Huang and Zhang, 2006). These methods are more robust to the camera noises and illumination variations. There are several approaches to generate and project fringe patterns: Laser interference, Moiré contouring, and digital fringe projection.

The laser interference method uses two wide planar laser beams to generate regular sinusoidal patterns through interference. To realize continuous or discrete phase shifts, numerous methods have been proposed. For example, Kothiyal and Delisle (1985) developed a polarization technique by rotating a half-wave plate; Wyant and Shagam (1978) proposed to use diffraction gratings and tilted glass to generate phase shifts; and Wyant (1982) proposed to realize phase shifts by using a mirror pushed by a piezo-electric transducer (PZT). The advantage of the laser interference is the exact generation of very fine patterns with unlimited depth of field. However, it requires high cost of the implementation and the typical laser artifacts (e.g., speckle noise) will affect measurement quality.

Moiré effect is another approach to generate sinusoidal fringe patterns. Moiré pattern is generated by shooting light onto two overlaid gratings while they are displaced or rotated with a small amount from one to another. Depending on the different setups for Moiré pattern formation, Moiré contouring techniques include shadow Moiré, projection Moiré and reflection Moiré. A shadow Moiré pattern forms between the reference grating and its shadow (Yoshizawa and Tomisawa, 1993; Jin et al., 2000). The setup of shadow Moiré is easy, but it is usually difficult to measure large objects. Projection Moiré uses two identical gratings: one for projection and the other for the reference (Harding and Harris, 1983). The projection Moiré technique can handle larger objects compared with the shadow Moiré technique. The reflection Moiré method is used for the objects with mirror-like surfaces (Chiang and Treiber, 1970; Fujiwara et al., 1996). Though applied extensively in industrial fields, the primary limitation of Moiré techniques is the tedium associated with obtaining quantitative height information and the requirements

of additional accurate controls if the phase shifting technique is adopted.

Recently, without using any physical gratings or interferometry, fringe patterns can be projected through digital devices, such as a liquid-crystal-display (LCD) projector or a digital mirror device (DMD) projector based on Digital Light Processing (DLP) technology. The technique of projecting sinusoidal fringe patterns with a digital video projector is called the digital fringe projection method. Because this technique utilizes the digital technologies, it provides dramatic advantages over the conventional methods: 1) different kinds of patterns can be easily generated by computer software; 2) there are no error caused by the mechanical devices for phase shifting; and 3) it can be easily combined with other systems and applied in different areas since the projection unit is a digital device. Because of these advantages and the potential for high-speed, high-accuracy 3D shape measurement, the DFP method has been recently extensively studied and increasingly employed in many fields.

2.2 Relevant Literature on High-Speed 3D Shape Measurement

With the increasing demand for measuring 3D information of high-speed motion, extensive research has been done and numerous high-speed 3D shape measurement systems have been developed. With the excellence in high speed and high accuracy, optical non-contact techniques remain to be the mainstreams. As discussed in the previous sections, some of the 3D shape measurement techniques have the potential for high-speed applications, and the DFD technique is one of those. However, considering the influence and scope of applications, several representative types of high-speed 3D shape measurement techniques are presented in this section, including TOF, stereo vision, speckle projection and fringe projection.

TOF is one of the techniques that are commercially used. Based on the TOF tech-

niques, several commercial products have been developed for real-time 3D depth measurement, such as DS325 from SoftKinetic (http://www.softkinetic.com), the second generation Kinect from Microsoft. However, the achieved depth accuracy, spatial resolution and the measurement speed are usually not high due to the fundamental limitations of the TOF technique.

Instead of using the specially designed sensors for the TOF technique, the stereo vision technique utilizes the standard digital cameras for 3D reconstruction. With the development of advanced camera technology, high-speed video cameras can achieve several million frames per second (fps) using either a charge-coupled device (CCD) (Chin et al., 2003) or a complementary metal-oxide-semiconductor (CMOS) sensor (e.g., Phantom v12.1). Taking advantages of the advanced camera technology, real-time and high-speed 3D measurement using the stereo vision principle has been developed with different hardware implementations (Lazaros et al., 2008). For example, Yang and Pollefeys (2003) proposed a multi-resolution real-time stereo vision algorithm by using a standard Graphic Processor Unit (GPU); Li and Jia (2006) presented a stereo vision system implemented by a Field Programmable Gates Array (FPGA) device at a video rate with the image size of 320 $\times$ 240 pixles; Calderon et al. (2010) recently presented a parallel hardware accelerator implemented by a FPGA device at the speed of 142 fps for 3D reconstruction with an image resolution of 320 $\times$ 240; and Woodll et al. (2004) developed an architecture for a stereo vision system implemented in a DeepSea processor with very high frame rates (up to 200 fps for 512 $\times$ 480 images). The stereo vision technique has the major advantage of achieving very high speed measurement since it reaches the camera's maximum frame rate. However, the measurement accuracy of this method is still not very high due to the classical challenging correspondence establishment problem, especially for measured objects without rich texture information.

To overcome the limitations of stereo vision methods, active techniques have been developed, such as the speckle projection method. Instead of using the ambient lighting,

it projects a speckle pattern to the measured object to assist correspondence establishment. The advantage of projecting a random texture (or speckle) pattern is that the randomness ensures that there is alway a unique pattern on which the correspondence can be found for different views of the cameras. Therefore, it can enhance the reliability and robustness of the conventional stereo vision technique and also improve the measurement accuracy. Previous studies on this technique were mainly based on the use of digital projectors, and only slow 3D measurement speeds were achieved (Siebert and Marshall, 2000; D'Apuzzo and Zurich, 2002; Chen and Chen, 2003). Recently, high-speed 3D shape measurement has been achieved by using laser speckle technologies. Schaffer et al. (2010) proposed a novel projection system that could project statistical speckle patterns at 500 Hz and reach a 3D measurement rate of 17 fps. Grosse et al. (2011) proposed an improved method with the 3D measurement speed up to 713 fps by shifting a fixed speckle pattern using a motor-driven wobbling mirror. Schaffer et al. (2011, 2013) also presented other approaches to increase the measurement speed by using an acousto-optical defector with a projection rate of nearly 200 kHz. Such systems could achieve a very high speed 3D measurement. However, it is difficult for them to reach camera-pixel spatial resolution because the matching regions used for correspondence establishment are typically larger than one camera pixel.

Structured-light technologies increase the measurement capability by actively projecting known structured patterns onto the objects, and thus the correspondence can be found easily with high accuracy. Though these techniques have been able to achieve tens of Hz, their spatial resolution is limited to being larger than a single projector pixel (Guan et al., 2003; Zhang et al., 2004; Davis et al., 2005). For fringe projection techniques, since the patterns have intensities that vary continuously from point to point in a known manner, they boost the structured light techniques from projector-pixel resolution to camera-pixel resolution (Zhang, 2010b). Due to the low cost, high speed and simplicity for development, the DFP technique has been a very active research area

within the past decade and a number of real-time systems have been developed by various researchers (Zhang and Huang, 2006a; Weise et al., 2007; Zhang and Yau, 2006; Liu et al., 2010; Li et al., 2010). However, the measurement speed of this technique is limited to the digital projector's refreshing rate (typically 120 Hz), which is not sufficient for many high-speed applications. To overcome the speed limitation, Lei and Zhang (2009) recently proposed a binary defocusing technique. Instead of using 8-bit sinusoidal patterns, the binary defocusing technique generates sinusoidal patterns by properly defocusing the squared 1-bit binary patterns. Since only 1-bit binary patterns are required, kilo-Hertz (kHz) 3D shape measurement rate has been achieved (Zhang et al., 2010). However, the binary defocusing technique suffers three major limitations: 1) low phase quality due to the influence of high-frequency harmonics; 2) smaller depth measurement range; and 3) low measurement accuracy due to the difficulty of applying existing calibration methods to the system with an out-of-focus projector.

The objective of this dissertation research thus is to overcome the major limitations of the binary defocusing technique without sacrificing its speed merit, and to develop a superfast 3D shape measurement platform for various applications. Since the calibration accuracy is crucial for 3D shape measurement accuracy, the following section will review the existing calibration methods for the DFP technique.

2.3 Relevant Literature on DFP System Calibration

In order to reconstruct 3D shape, the DFP system must be calibrated prior to any measurement. Over the years, numerous calibration methods have been developed, and they can generally be classified into three major categories. The first type of calibration method is to accurately calibrate the system parameters, like the positions and orientations of the camera and projector, and then retrieve the depth information based on these calibrated parameters (Hu et al., 2003; Mao et al., 2007; Zappa and Busca, 2009).

Though they could achieve good measurement accuracy, the key issue of this type of calibration methods is that it is difficult to obtain the system parameters with high accuracy without extremely expensive and complex calibration setup (e.g., involving the use of CMMs). Consequently, the recovered shape measurement accuracy is inevitably limited if all these high standards are not met.

To improve this, another sort of calibration approach is to establish a general governing equation that relates the depth information to the phase value. For example, by adopting least-squares methods, the constant parameters or coefficients in the relationship equation(s) can be estimated through calibration. Guo et al. (2006) presented a least-squares fitting scheme by using a rational function. Du and Wang (2007) proposed a more generalized mathematical model and solved the coefficients with a nonlinear least-squares algorithm. Researches have also been carried out to further improve the accuracy and calibration flexibility (Huang et al., 2010; Vo et al., 2012).

The third popular type of calibration approach is to use a stereo-vision-based method by treating the projector as an inverse of a camera, in which the homologous points are established with the aid of the absolute phase map. Legarda-Saenz et al. (2004) proposed to establish a rigid constraint based on the unique coordinate systems in the structured light system and estimate the system parameters using least-squares optimization methods, such as the Levenberg-Marquardt method. Zhang and Huang (2006b) proposed a novel calibration method by enabling the projector to 'capture' images like a camera and thus adopt the well-established calibration procedures to calibrate both the projector and camera. To improve Zhang's method, Li et al. (2008) presented a method by using a precalibrated lookup table and a linear interpolation algorithm for projector calibration and Yin et al. (2012) proposed to use the bundle adjustment strategy for coordinates adjustments.

The existing calibration methods could achieve high accuracy, but they always assume the projector to be at least nearly in-focus, in order to establish the relationship between

the depth and absolute phase information or directly or indirectly calibrate the projector as a reverse camera. However, for the recently developed binary defocusing technique, a new accurate calibration method is required since the projector is significantly out of focus. There is one simple approximation calibration method described in Ref. (Xu et al., 2011) which could be used for the defocusing system. However, the accuracy is very low and far from sufficient for high-accuracy 3D shape measurement. Therefore, in order to achieve superfast high-accuracy 3D shape measurement based on the binary defocusing technique, the dissertation research aims to develop a novel accurate calibration method for the DFP system using an out-of-focused projector.

2.4 Conclusion

This chapter examined the basic principles of different 3D shape measurement techniques and especially the studies conducted on high-speed 3D measurements. Since the calibration process is crucial to high-accuracy measurement, the calibration methods for the DFP technique are also reviewed in this chapter. Though numerous 3D shape measurement techniques have been developed, few of them can simultaneously achieve high speed and high accuracy. The recently proposed binary defocusing technique has the potential for high-speed and high-accuracy 3D shape measurement. However, it still has three major limitations: low phase quality due to the influence of high-frequency harmonics, limited depth measurement range, and low measurement accuracy due to the difficulty of applying existing calibration methods to the system with an out-of-focus projector. Furthermore, there are also problems associated with hardware limitations when the measurement speeds go beyond a certain range. All of these challenges have to be simultaneously conquered in order to achieve superfast and high-accuracy 3D shape measurement, which is the main focus of this dissertation research.

CHAPTER 3. OPTIMAL PULSE WIDTH MODULATION FOR SINUSOIDAL FRINGE GENERATION WITH PROJECTOR DEFOCUSING

A paper published in the Journal of Optics Letters in December 2010.[1]

Yajun Wang[2,4] and Song Zhang[3,4]

3.1 Abstract

Recently study showed that generating sinusoidal fringe patterns by properly defocusing binary ones can significantly simplify 3-D shape measurement system development, and drastically improve its speed. However, when the fringe stripes are very wide, it is very difficult for this technique to achieve high-quality measurement. This letter presents a method to improve this technique by selectively eliminating high-frequency harmonics induced a squared binary pattern. By this means, better sinusoidal fringe patterns can be generated with a small degree of defocusing even for wide fringe stripes. Simulation and experiments will be presented to verify the performance of this proposed technique.

[1]This paper was published in the Journal of Optics Letters and is made available as an electronic reprint with the permission of OSA. The paper can be found at the following URL on the OSA website: http://www.opticsinfobase.org/ol/abstract.cfm?URI=ol-35-24-4121. Systematic or multiple reproduction of distribution to multiple locations via electronic or other means is prohibited and is subject to penalties under law.

[2]Primary researcher and author.

[3]Assistant professor and advisor.

[4]Department of Mechanical Engineering, Iowa State University.

3.2 Introduction

In recent years, digital fringe projection techniques have received significant attention for non-contact 3-D shape measurement, because of its high speed, flexibility, low cost and potentially high accuracy (Gorthi and Rastogi, 2010). To achieve high measurement accuracy, ideal sinusoidal fringe patterns have to be generated by the projector. This is not always easy because the commercial video projector is a nonlinear device. Recently, we proposed a new technique that is to generate sinusoidal fringe patterns by properly defocusing binary structured ones (Lei and Zhang, 2009). In this letter, we called this technique squared binary method (SBM). This new fringe generation method has numerous advantages over a traditional fringe generation method (Lei and Zhang, 2010): (1) it is less sensitive the synchronization between the camera and the projector; (2) the nonlinear gamma of the projector do not affect the measurement; (3) the exposure time can be much shorter than the projector's single channel projection time of an off-the-shelf digital light processing (DLP) projector (Gong and Zhang, 2010); and (4) it enables a superfast 3-D shape measurement technique (Zhang et al., 2010).

However, this technology is not trouble free. We found that it performs well only when the fringe stripe is narrow, but shows significant problems if the fringe stripe is wide. This limits its measurement capability especially when a step height object is to be measured. Actually, sinusoidal pulse width modulation method (SPWM) is a well-known technique of electrical engineering for the generation of sinusoidal waveforms using low-pass filtered structured binary signals (Williams, 2006). Recently, the SPWM method was proposed to greatly improve the defocusing technique when the fringe stripe is wide (Ajubi et al., 2010). In brief, SPWM modulate the squared binary patterns by comparing the desired sinusoidal pattern with a high-frequency triangular waveform. By this means, the high-frequency harmonics are shifted further away from the fundamental frequency, thus are easier to be suppressed by a low-pass filter. Therefore, SPWM could

generate better sinusoidal pattern even with a small degree of defocusing. However, we found that SPWM outperforms the the binary method only when the fringe stripes is within a certain range of pixel number. This may be caused by the discrete fringe generation nature of a digital fringe projection technique.

In this letter, we propose a technique called optimal pulse width modulation (OPWM) to further improve the defocusing technique by selectively eliminating undesired harmonics. Because this technique can remove any harmonics that are affecting the measurement quality the most, it has the potential to generate high-quality sinusoidal fringe patterns. Both simulation and experimental results showed that this technique outperforms the SPWM or the SBM method with a very large range of fringe stripe size.

3.3 Principle

Phase-shifting methods are widely used in optical metrology because of their speed and accuracy (Malacara, 2007). We use a three-step phase-shifting algorithm to find the phase value, thereby the phase error. Three fringe images with a phase shift of $2\pi/3$ can be written as:

$$I_1(x,y) = I'(x,y) + I''(x,y)\cos(\phi - 2\pi/3), \tag{3.1}$$

$$I_2(x,y) = I'(x,y) + I''(x,y)\cos(\phi), \tag{3.2}$$

$$I_3(x,y) = I'(x,y) + I''(x,y)\cos(\phi + 2\pi/3). \tag{3.3}$$

Where $I'(x,y)$ is the average intensity, $I''(x,y)$ the intensity modulation, and $\phi(x,y)$ the phase to be solved for. The phase can be solved for from these equations as

$$\phi(x,y) = \tan^{-1}\left[\sqrt{3}(I_1 - I_3)/(2I_2 - I_1 - I_3)\right]. \tag{3.4}$$

This equation provides the wrapped phase ranging from $-\pi$ to $+\pi$ with 2π discontinuities. This 2π phase jumps can be removed to obtain the continuous phase map by adopting a phase unwrapping algorithm (Ghiglia and Pritt, 1998).

In a digital fringe projection system, sinusoidal patterns can be projected directly using digital video projector. Usually, gamma calibration is necessary and the projection speed is limited because of a commercial video projector is a nonlinear device and the digital fringe generation nature. To circumvent these problems, sinusoidal fringe pattern generation by properly defocusing binary ones is proposed (Lei and Zhang, 2009). SPWM also belongs to binary method but it improves the performance of the conventional SBM method. However, it still has limitations when the fringe stripes are wide.

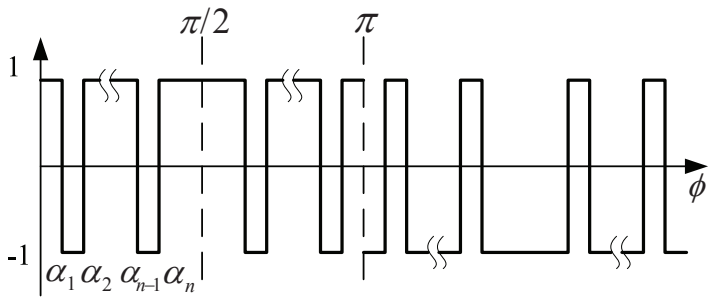

Figure 3.1 Quarter-wave symmetric OPWM waveform.

To further improve the defocusing technique, we proposed this OPWM method. This technique is to selectively eliminate undesired frequency components to generate ideal sinusoidal fringe pattern by projector defocusing. Figure 3.1 illustrates a general quarter-wave symmetric OPWM pattern. The square wave is chopped n times per-half cycle. For a periodic waveform with a period of 2π, the Fourier series coefficients are:

$$a_0 = \frac{1}{2\pi}\int_{\theta=0}^{2\pi} f(\theta)d\theta, \tag{3.5}$$

$$a_k = \frac{1}{\pi}\int_{\theta=0}^{2\pi} f(\theta)\cos(k\theta)d\theta, \tag{3.6}$$

$$b_k = \frac{1}{\pi}\int_{\theta=0}^{2\pi} f(\theta)\sin(k\theta)d\theta. \tag{3.7}$$

Because the half-cycle symmetry of an OPWM wave, only odd order harmonics exist, i.e, $a_0 = 0$, and $a_k = 0$. Furthermore, b_k can be simplified as:

$$b_k = \frac{4}{\pi}\int_{\theta=0}^{\pi/2} f(\theta)\sin(k\theta)d\theta. \tag{3.8}$$

For the binary OPWM waveform, $f(\theta)$, we have

$$\begin{aligned} b_k &= \frac{4}{\pi}\int_0^{\alpha_1}\sin(k\theta)d\theta - \frac{4}{\pi}\int_{\alpha_1}^{\alpha_2}\sin(k\theta)d\theta \\ &\quad + \frac{4}{\pi}\int_{\alpha_2}^{\alpha_3}\sin(k\theta)d\theta \ldots \frac{4}{\pi}\int_{\alpha_n}^{\pi/2}\sin(k\theta)d\theta \end{aligned} \tag{3.9}$$

The n chops in the waveform afford n degrees of freedom. It is easy to eliminate $n-1$ selected harmonics whilst to keep the fundamental frequency component within a certain magnitude. To do this, one can set the corresponding coefficients in the above equation to be desired values (0 for the $n-1$ harmonics to be eliminated and the desired magnitude for the fundamental frequency), and solve for the angles for all notches (Agelidis et al., 2004). Some research has been conducted to solve for transcendental equations (Chiasson et al., 2004). Due to the ability to eliminate undesired high-order harmonics, OPWM waveform could become sinusoidal after applying a low-pass filter, which is similar to a small degree of defocusing. Therefore, this technique can be realized by a real measurement system.

Simulation was conducted to very the effectiveness of the proposed method. A Gaussian filter is used to approximate the defocusing effect. In this research, a Gaussian filter with size of 5 and standard deviation of 2 pixels is applied twice for all fringe patterns generated by different method. From above analysis, there are numerous options for OPWM patterns having different number of notches for a fringe patterns with a certain fringe pitch P, the number of pixels per fringe stripe. Therefore, it is interesting to find the best OPWM pattern to optimize the measurement quality. The best OPWM pattern was defined as it will have the minimum phase error if it is used to perform a measurement. In this research, the phase is calculated by using a three-step phase-shifting algorithm, and the phase error is determined by comparing against the phase result from ideal sinusoidal fringe patterns with the same number of fringe pitch. A simulation was performed to compare the phase error within different methods under exactly the same degree of defocusing. Fig. 3.2(a) shows the cross-sections of the SBM, SPWM and OPWM patterns. And Fig.3.2(b) are the results after defocusing, or smoothing by

a Gaussian filter. It should be noted that the SPWM was also optimized to minimize the phase error by selecting the proper modulation frequency.

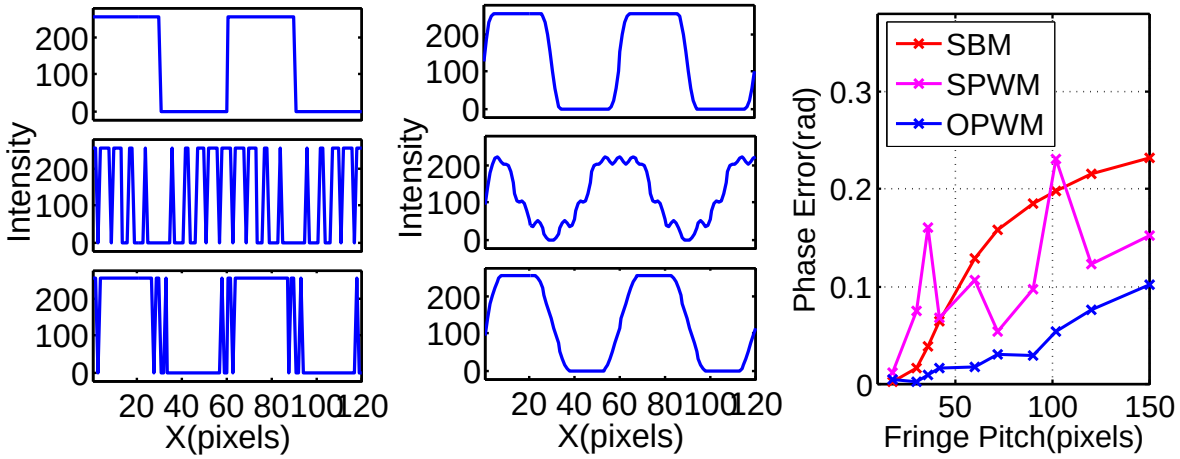

(a) (b) (c)

Figure 3.2 (a) The cross sections of the SBM, SPWM and OPWM pattern; (b) Corresponding defocused results; (c) RMS errors with different fringe pitches.

Fig. 3.2(c) shows the RMS errors for different methods when the fringe pitch varies from 18 to 150 pixels. This simulation result shows that the OPWM gives the smallest phase error in almost all range and SPWM performs better than SBM only when the period is large enough. This also indicates that when the fringe stripe is narrow, such as 18 pixels or less in pitch, SBM performs the best. This is because the fringe pattern is generated discretely, it does not have sufficient pixels to set proper notches for further improvement.

3.4 Experimental Results

Experiments were also performed to verify the proposed approach. We developed a 3-D shape measurement system includes a DLP projector (Samsung P310) and a digital USB CCD camera (The Imaging Source DMK 21BU04). The camera is attached with a 12 mm focal length Mega-pixel lens (Computar M1214-MP). The resolution of the

camera is 640 ×480, with a maximum frame rate of 60 frames/sec. The projector has a resolution of 858 × 600 with a lens of F/2.0 and f = 16.67 mm.

We first evaluate the phase error by measuring an uniform white flat surface. Phase-shifted fringe patterns with exactly the same fringe pitch generated are captured to obtain the phase value for each of them. Fig. 3.3(a)-3.3(c) show the fringe patterns with a pitch of 120 pixels. In addition, the ideal sinusoidal fringe patterns are also used to obtain the grand truth phase values to compare against. The phase errors shown in Fig. 3.3(e) are obtained by getting the phase differences between the associated method with the sinusoidal method. It should be noted the projector's nonlinear gamma was corrected to generate the ideal sinusoidal fringe patterns.

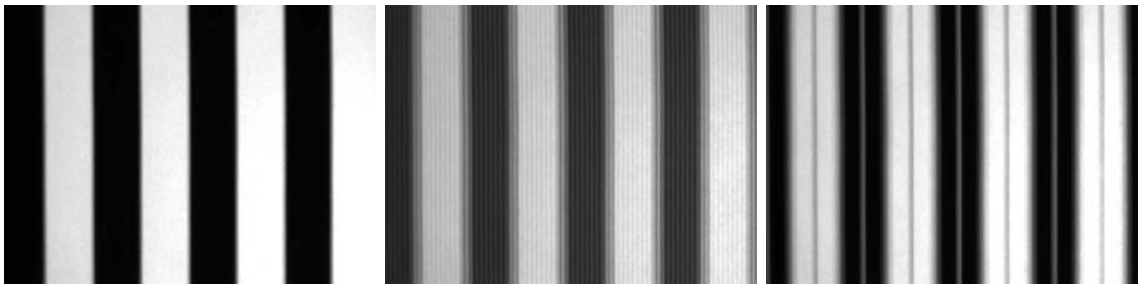

(a) (b) (c)

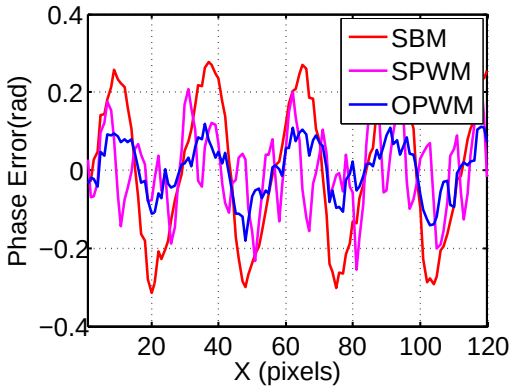

(d)

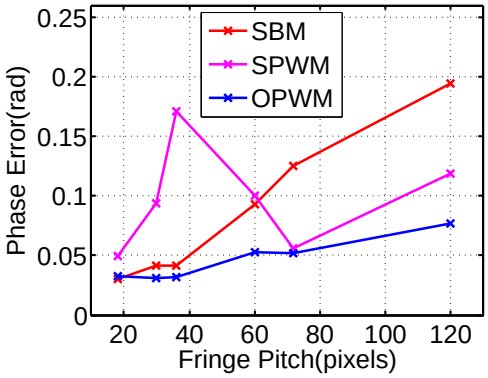

(e)

Figure 3.3 First row shows fringe patterns when $P = 120$ pixels. (a) SBM pattern; (b) SPWM pattern; (c) OPWM pattern; (d) Cross sections of phase errors when $P = 120$ pixels; (f) RMS errors for different fringe pitches.

Figure 3.3(e) clearly shows that when the fringe pitch number is small (e.g., 30 pixels), the SPWM cannot perform as well as either the SBM or OPWM method. However, when fringe pitch increases to 120 pixels, the OPWM gives the best result. Fig. 3.3(d) shows the cross sections of the phase errors for each method when the pitch is 120 pixels.

To further compare the measurement quality using these method. A complicated 3-D sculpture was measured. Figure 3.4 shows the measurement results. It can be seen that when the fringe stripes are narrow, the SBM and the OPWM method outperforms the SPWM, and the former two give similar quality of measurement. However, when the fringe pitch increases, the OPWM produces the best result.

3.5 Conclusion

This letter has introduced an OPWM technique to generate high-quality sinusoidal fringe patterns by slightly defocusing binary ones. This technique is to selectively eliminate undesired high-frequency high harmonics of a standard squared binary patterns. Both simulation and experiment results have verified that the method indeed could significantly improve the measurement quality if the fringe stripes are more than 18 pixels.

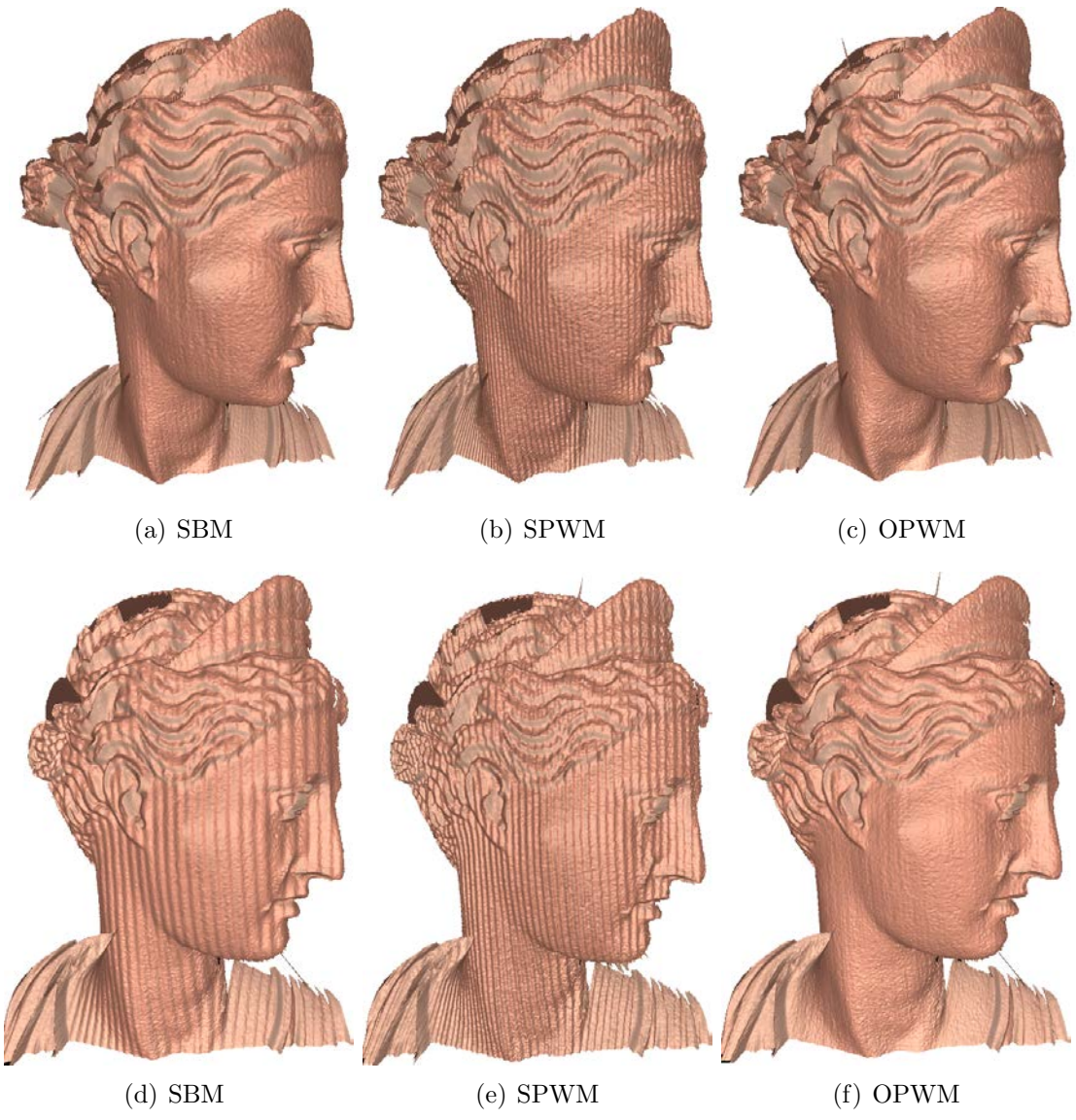

(a) SBM (b) SPWM (c) OPWM

(d) SBM (e) SPWM (f) OPWM

Figure 3.4 3-D shape measurement of a sculpture. The first row shows the results when $P = 30$ pixels, and the second row shows the results when $P = 60$ pixels.

CHAPTER 4. SUPERFAST MULTIFREQUENCY PHASE-SHIFTING TECHNIQUE WITH OPTIMAL PULSE WIDTH MODULATION

A paper published in the Journal of Optics Express in March 2011.[1]

Yajun Wang[2,4] and Song Zhang[3,4]

4.1 Abstract

The technique of generating sinusoidal fringe patterns by defocusing squared binary structured ones has numerous merits for high-speed three-dimensional (3D) shape measurement. However, it is challenging for this method to realize a multifrequency phase-shifting (MFPS) algorithm because it is difficult to simultaneously generate high-quality sinusoidal fringe patterns with different periods. This paper proposes to realize an MFPS algorithm utilizing an optimal pulse width modulation (OPWM) technique that can selectively eliminate high-order harmonics of squared binary patterns. We successfully develop a 556 Hz system utilizing a three-frequency algorithm for simultaneously measuring multiple objects.

[1]This paper was published in the Journal of Optics Express and is made available as an electronic reprint with the permission of OSA. The paper can be found at the following URL on the OSA website: http://www.opticsinfobase.org/oe/abstract.cfm?URI=oe-19-6-5149. Systematic or multiple reproduction of distribution to multiple locations via electronic or other means is prohibited and is subject to penalties under law.

[2]Primary researcher and author.

[3]Assistant professor and advisor.

[4]Department of Mechanical Engineering, Iowa State University.

4.2 Introduction

Three-dimensional (3D) shape measurement is quite important in many areas ranging from manufacturing to medicine. Numerous techniques have been developed including Moiré, holography, and fringe projection (Gorthi and Rastogi, 2010). Among these methods, the digital fringe projection technique has been exhaustively studied and widely used in many fields due to its simple setup, automatic data processing, high-speed and high-resolution measurement capabilities.

For a digital fringe projection system, ideal sinusoidal fringe patterns are used to retrieve 3D information. Su et al. (Su et al., 1992) and Lei and Zhang (Lei and Zhang, 2009) has proposed a technique that is to generate sinusoidal fringe patterns by properly defocusing squared binary structured ones using a mechanical grating (former) or a digital video projector (latter), which we call a squared binary method (SBM). The SBM has numerous advantages for 3D shape measurement especially for high-speed applications (Lei and Zhang, 2010): (1) It is less sensitive to the synchronization between the camera and the projector; (2) The nonlinear gamma of the projector does not affect the measurement quality; (3) The exposure time can be much shorter than the projector's single channel projection time for an off-the-shelf digital light processing (DLP) projector, thus it could enable a superfast 3D shape measurement technique.

For the measurement of a single object without step heights, SBM can perform well if the projector is properly defocused (Lei and Zhang, 2010). To extend the measurement range of the defocusing technique, Zhang proposed a method to obtain absolute phase by introducing binary coded patterns (Zhang, 2010a). Because it permits point-by-point absolute phase extraction, the defocusing technique is further enhanced and the high-speed multi-object measurement becomes possible. However, this method is not trouble free. Because sinusoidal fringe patterns are generated by defocusing, the binary coded ones are blurred, which makes it difficult to correctly determine the designed code. As

a result, the perfectly designed code might not work. This problem is deteriorated for high-speed applications since motion could introduce additional misalignment.

To further improve the capability of high-speed multi-object measurement, this paper proposes a multifrequency phase-shifting (MFPS) method with an optimal pulse width modulation (OPWM) technique. OPWM is a recently developed technique to improve the fringe quality for the SBM (Wang and Zhang, 2010). The SBM performs well only when the fringe stripes are narrow but shows significant problems if the fringe stripes are wide. Moreover, an MFPS cannot be realized because it is impossible to obtain high quality sinusoidal fringe patterns with different breadth under the same defocusing degree. By selectively eliminate undesired harmonics, OPWM technique permits the generation of high-quality fringes with different breadths under a slightly defocused projector. Therefore, the MFPS method, an effective and widely-adopted approach for multi-object measurement, becomes feasible using the defocusing technique. Moreover, because OPWM still uses binary patterns, it maintains the aforementioned advantages of the defocusing technique. In this research, we have developed a 5,000 Hz fringe projection system, that could realize 556 Hz 3D shape measurement using a three-frequency phase-shifting method for simultaneous multiple objects measurement.

4.3 Principle

4.3.1 Three-Step Phase-Shifting Algorithm

Phase-shifting algorithms are widely used in optical metrology because of their measurement speed and accuracy (Malacara, 2007). Numerous phase-shifting algorithms have been developed including three step, four step, double three step, and five step. In this paper, we use a three-step phase-shifting algorithm with a phase shift of $2\pi/3$.

Three fringe images can be described as,

$$I_1(x,y) = I'(x,y) + I''(x,y)\cos(\phi - 2\pi/3), \tag{4.1}$$

$$I_2(x,y) = I'(x,y) + I''(x,y)\cos(\phi), \tag{4.2}$$

$$I_3(x,y) = I'(x,y) + I''(x,y)\cos(\phi + 2\pi/3). \tag{4.3}$$

Where $I'(x,y)$ is the average intensity, $I''(x,y)$ the intensity modulation, and $\phi(x,y)$ the phase to be solved for. The phase,$\phi(x,y)$, and the texture, $I'(x,y)$, can be solved for from these equations

$$\phi(x,y) = \tan^{-1}\left[\sqrt{3}(I_1 - I_3)/(2I_2 - I_1 - I_3)\right], \tag{4.4}$$

$$I'(x,y) = (I_1 + I_2 + I_3)/3. \tag{4.5}$$

Equation (9.4) provides the phase ranging $[-\pi,\ \pi)$ with 2π discontinuities. This 2π phase jumps can be removed to obtain the continuous phase map by adopting a phase unwrapping algorithm (Ghiglia and Pritt, 1998). However, such a spatial phase unwrapping algorithm has limitations: it could not used when large step height exists which may cause the phase change more than π, or multiple objects need to be measured simultaneously.

4.3.2 Multifrequency Phase-Shifting (MFPS) Algorithm

As aforementioned, the phase we obtain from a single-frequency method is within the range of [-π, π). When a fringe pattern contains more than one stripes, the phase need to be unwrapped to obtain the continuous phase map. This means that if another set of wider fringe patterns (a single fringe stripe can cover the whole image) is used to obtain a phase map without 2π discontinuities. The second phase map can be used unwrap the other one point by point without spatial phase unwrapping. To obtain the phase of the wider fringe patterns, there are two approaches: (1) use very long wavelength directly; and (2) use two short wavelengths to generate an equivalent long one. The former is not

very commonly used because it is difficult to generate high-quality wide fringe patterns due to noises or hardware limitations. Thus the latter is more frequently adopted. This subsection will briefly explain the principle of this technique.

Theoretically, the relationship between the absolute phase Φ and the wavelength λ, and the height $h(x, y)$ can be written as

$$\Phi = [C \cdot h(x, y)/\lambda] \cdot 2\pi. \tag{4.6}$$

Here C is a system constant. Therefore, for $\lambda_1 < \lambda_2$ with absolute phase being Φ_1 and Φ_2, respectively, their difference is

$$\Delta\Phi_{12} = \Phi_1 - \Phi_2 = [C \cdot h(x, y)/\lambda_{12}^{eq}] \cdot 2\pi. \tag{4.7}$$

Here, $\lambda_{12}^{eq} = \lambda_1\lambda_2/|\lambda_2 - \lambda_1|$ is the equivalent wavelength between λ_1 and λ_2. If $\lambda_2 \in (\lambda_1, 2\lambda_1)$, we have $\lambda_{12}^{eq} > \lambda_2$. In reality, we only have the wrapped phase, ϕ_1 and ϕ_2. We know that the relationship between the absolute phase is Φ and the wrapped phase $\phi = \Phi \pmod{2\pi}$ with 2π discontinuities. Here the modulus operator is to convert the phase to a range of $[0, 2\pi)$. Taking the modulus operation on Eq.(4.7) will lead to

$$\Delta\phi_{12} = [\Phi_1 - \Phi_2] \pmod{2\pi} = [\phi_1 - \phi_2] \pmod{2\pi}. \tag{4.8}$$

$\Delta\phi_{12} = \Delta\Phi_{12} \pmod{2\pi}$. If the wavelengths are properly chosen, so that the resultant equivalent wavelength λ_{12}^{eq} is large enough to cover the whole range of image (i.e., $|C \cdot h(x, y)/\lambda_{12}^{eq}| < 1$). In this case, the modulus operator does not affect anything, thus no phase unwrapping is required.

However, because the existence of noises, two-frequency technique is usually not sufficient (Creath, 1987). Practically, at least three frequency fringe patterns are required for point by point absolute phase measurement. The multifrequency technique is designed so that the equivalent widest fringe stripe can cover the whole image (Towers et al., 2003).

Assume another set of fringe patterns with wavelength (λ_3) are used, the equivalent wavelength between λ_1 and λ_3 will be $\lambda_{13}^{eq} = \lambda_1\lambda_3/|\lambda_3 - \lambda_1|$. We will have

$$\Delta\phi_{13} = [\phi_1 - \phi_3] \pmod{2\pi} = \{[C \cdot h(x,y)/\lambda_{13}^{eq}] \cdot 2\pi\} \pmod{2\pi}, \quad (4.9)$$

$$\Delta\phi_{123} = (\Delta\phi_{13} - \Delta\phi_{12}) \pmod{2\pi} = \{[C \cdot h(x,y)/\lambda_{123}^{eq}] \cdot 2\pi\} \pmod{2\pi}. \quad (4.10)$$

Here $\lambda_{123}^{eq} = \lambda_{12}^{eq}\lambda_{13}^{eq}/|\lambda_{13}^{eq} - \lambda_{12}^{eq}|$. Now we only need $|C \cdot h(x,y)/\lambda_{123}^{eq}| < 1$ to ensure that the absolute phase can be obtained without spatial phase unwrapping. Once the absolute phase of the longest equivalent wavelength is obtained, it can reversely unwrap the phase of other wavelengths. The phase of shortest wavelength is usually used to recover 3D information because the measurement accuracy is approximately inversely proportional to the wavelength.

4.3.3 Optimal Pulse Width Modulation (OPWM) Technique

The aforementioned MFPS technique requires to generate sinusoidal fringe patterns with different frequencies. A conventional fringe projection system uses a computer to generate sinusoidal fringe patterns that are sent to a projector. However, when 8-bit sinusoidal patterns are used, there are many limitations due to the commercial projectors such as gamma calibration and capturing speed (Lei and Zhang, 2010). The defocusing technique has the potential to alleviate these limitations.

However, the SBM performs well only when the fringe stripe is narrow. When the fringe stripe becomes wide, it is difficult to obtain high-quality sinusoidal pattern by defocusing projector. This is because the binary square wave contains numerous harmonics. When the fringe stripe is wide, the high-order harmonics are closer to the fundamental one, thus it is difficult to drastically suppress them by the defocusing effect. However, to realize an MFPS algorithm, sinusoidal patterns with wide fringe stripes are required. Moreover, under the same degree of defocusing, it is practically impossible to generate high quality sinusoidal fringe patterns with different wavelengths. Thus, a conventional

SBM method cannot realize an MFPS algorithm.

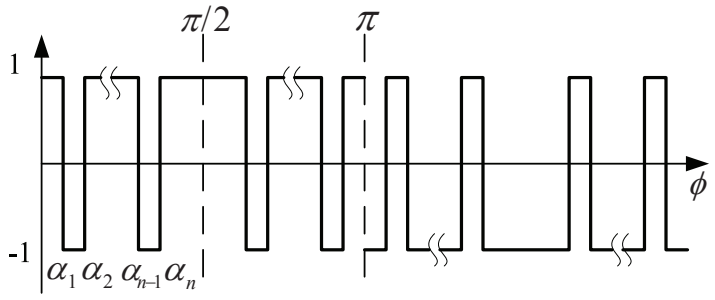

Figure 4.1 Quarter-wave symmetric OPWM waveform.

To achieve high quality 3D shape measurement with wide fringe stripes, the OPWM technique was proposed (Wang and Zhang, 2010). This technique is to selectively eliminate undesired frequency components by inserting different types of notches in a conventional binary square wave. Then with slightly projector defocusing, high-quality sinusoidal fringe patterns can be generated. Figure 4.1 illustrates a general quarter-wave symmetric OPWM pattern. The square wave is chopped n times per-half cycle. For a periodic waveform with a period of 2π, because it is an odd function, only the sine terms are left with the coefficients being described as:

$$b_k = \frac{4}{\pi} \int_{\theta=0}^{\pi/2} f(\theta) \sin(k\theta) d\theta. \tag{4.11}$$

The n chops in the waveform provide n degrees of freedom to eliminate $n-1$ selected harmonics whilst keeping the fundamental frequency component within a certain magnitude (Agelidis et al., 2004). Due to the ability to eliminate undesired high-order harmonics, OPWM waveform could become sinusoidal after applying a small low-pass filter, which is similar to a small degree of defocusing. Our previous research has shown that (1) the OPWM technique can be used to generate high-quality sinusoidal patterns even with very wide fringe stripes; and (2) it is not very sensitive to the degree of defocusing. Here, the degree of defocusing corresponds to the depth measurement range. The less sensitive to the degree of defocusing indicates that less phase error is generated

within the same depth range. In other words, under the same degree of defocusing, it is possible for this technique to generate high-quality sinusoidal fringe patterns with different periods. By this means, an MFPS method can be realized.

4.4 Experimental Results

We have developed a superfast system that is composed of a DLP Discovery projection system, a high-speed CMOS camera, and a self-developed synchronization circuit. The DLP Discovery projection system includes a DLP Discovery board (D4000), an ALP High Speed and an optical module (S3X). The camera used in this system is Phantom V9.1. The synchronization circuit takes the projection timing signal and generate timing signal to trigger the camera.

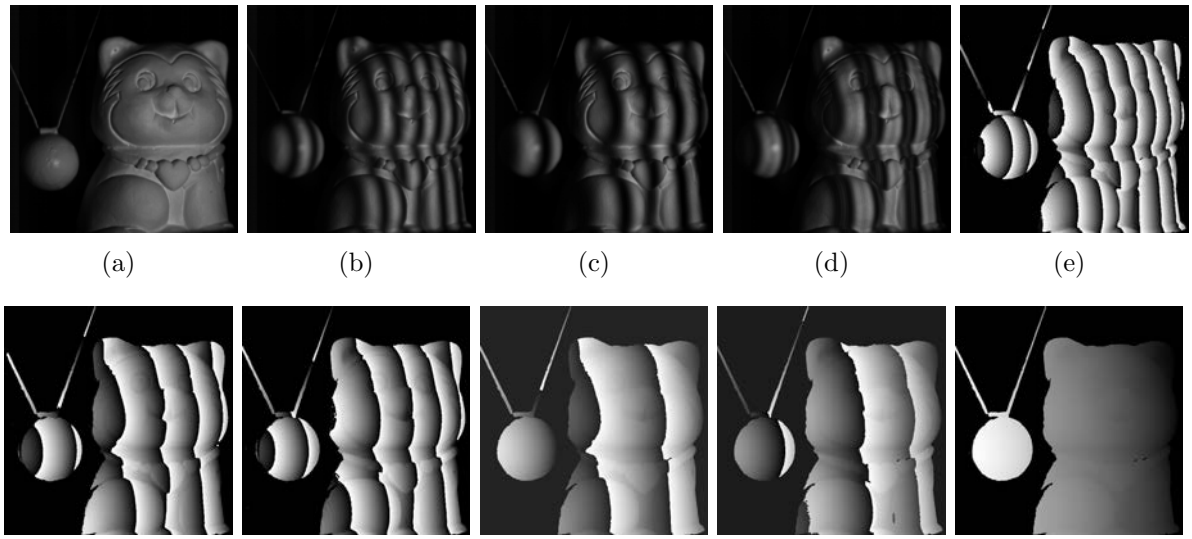

Figure 4.2 (a) Photograph of the captured scene; (b) One fringe pattern ($\lambda_1 = 60$ pixels); (c) One fringe pattern ($\lambda_2 = 90$ pixels); (d) One fringe pattern($\lambda_3 = 102$ pixels); (e) Wrapped phase ϕ_1; (f) Wrapped phase ϕ_2; (g) Wrapped phase ϕ_3; (h) Equivalent phase difference $\Delta\phi_{12}$; (i) Equivalent phase difference $\Delta\phi_{13}$; (j) Resultant phase $\Delta\phi_{123}$.

To test the proposed algorithm, we chose three frequency fringe patterns with $\lambda_1 =$

60, $\lambda_2 = 90$, and $\lambda_3 = 102$ pixels. It can be found that the resultant equivalent fringe wavelength is 765 pixels. In other words, if we use the projector to generate 765 pixel wide fringe patterns, no spatial phase unwrapping is needed to recover absolute phase.

To demonstrate that this technique can be used to perform superfast 3D shape measurement for multiple objects, we chose our system to switch and capture 2D fringe patterns at 5,000 Hz, and measured two separate objects. The camera image resolution is set as 576 $\times$ 576 pixels. In this experiment, there are two separate objects, a static sculpture on the right, and a swinging pendulum ball on the left, as shown in Fig. 4.2(a). The diameter of the spherical ball is about 17 mm, the stature is approximately 60 (H) $\times$ 45 (W) mm in the viewing volume of the camera. Figure 4.2(b)-4.2(d) show the distorted OPWM fringe patterns with different frequencies. Figures 4.2(e)-4.2(g) respectively show the wrapped phase maps extracted from those frequencies. The corresponding equivalent wrapped phase for λ_1 and λ_2 is shown in Fig. 4.2(h), and that for λ_1 and λ_3 is shown in Fig. 4.2(i). Finally, the phase map of the longest equivalent wavelength can be obtained from these two equivalent phase maps, and the result is shown in Fig. 4.2(j). It can be seen from this figure that this phase map has no 2π discontinuities, thus no spatial phase unwrapping is needed.

From this longest equivalent wavelength phase map, the shortest one with $\lambda_1 = 60$ pixels can be unwrapped point by point that can then be used to recover 3D information. In this research, we use the calibration technique introduced in Ref. (Zhang et al., 2010) to calibrate our system. Because this is an approximation method, the accuracy is not very high. We found that with the defocusing technique, the measurement error is approximately root-mean-squared (rms) 0.19 mm over a measurement depth range of 6.35 mm. We cannot implement any existing high-accuracy structured light system calibration technique because they all require the projector to be in focus, which is not the case for our system. We are exploring a new method to accurately calibrate a defocused projector. If successful, it will significantly improve the measurement accuracy of our

system. At current stage, we believe our measurement accuracy is not as high as other high-speed 3D shape measurement techniques such as the one described in Ref. (Schaffer et al., 2010).

Figure 4.3(a) shows the image after averaging three fringe patterns with the shortest wavelength. Fig. 4.3(b) shows the reconstructed 3D result. It can be seen that even though OPWM technique can recover 3D shape very well, it shows some artifacts on the averaged texture image. This is because the operation of OPWM is in phase domain without considering the texture information. It can be seen that the proposed method can be used to obtain absolute phase point by point, and can be used to simultaneously measure multiple objects.

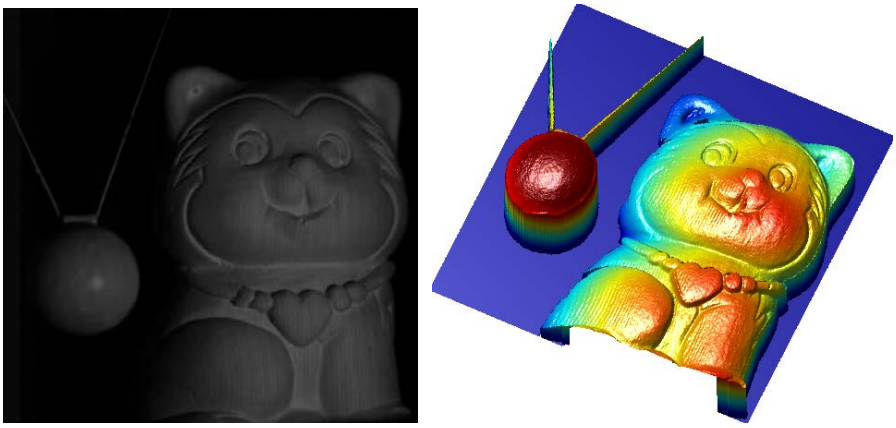

(a) (b)

Figure 4.3 (a) Averaged image of the object (Media 1); (b) 3-D result (Media 2).

Since the fringe images are captured at 5,000 Hz, and a three-frequency phase-shifting algorithm is used, the 3D shape measurement speed is actually $5{,}000/9 = 556$ Hz, which is sufficient to capture the rapid motion, such as a pendulum system. From 900 2D images, 100 3D frames can be recovered. Media 1 shows the video of the averaged texture images, the video is played at 25 fps, which is approximately 1/22 of the capturing speed. The textured images, $I'(x, y)$ in Eq. (4.5), are generated by averaging three shortest wavelength phase-shifted fringe patterns. Medias 2 shows the 3D reconstructed results at 25

fps. This experiment clearly demonstrated that by combining the OPWM technique with the defocusing technique, a superfast MFPS algorithm can be realized. This proposed technique can be used to measure multiple rapidly moving objects simultaneously.

4.5 Conclusion

This paper has presented a multifrequency phase-shifting method with an optimal pulse width modulation technique to conduct superfast simultaneous multiple objects measurement. We have developed a 556 Hz 3D shape measurement system using a three-frequency phase-shifting algorithm. Experiments have been conducted and proved the success of the proposed technique.

CHAPTER 5. 3D SHAPE MEASUREMENT WITH BINARY DITHERING TECHNIQUES

A paper published in the Journal of Applied Optics in September 2012.[1]

Yajun Wang[2,4] and Song Zhang[3,4]

5.1 Abstract

The previously proposed binary defocusing technique and its variations have proven successful for high-quality three-dimensional (3D) shape measurement when fringe stripes are relatively narrow, but they suffer if fringe stripes are wide. This paper proposes to utilize the binary dithering technique to conquer this challenge. Both simulation and experimental results show the phase error is always less than 0.6% even when the fringe stripes are wide and the projector is nearly focused.

5.2 Introduction

The recently proposed binary defocusing technique (Lei and Zhang, 2009) and its variations (Wang and Zhang, 2010; Ajubi et al., 2010) have demonstrated their supe-

[1]This paper was published in the Journal of Applied Optics and is made available as an electronic reprint with the permission of OSA. The paper can be found at the following URL on the OSA website: http://www.opticsinfobase.org/ao/abstract.cfm?URI=ao-51-27-6631. Systematic or multiple reproduction of distribution to multiple locations via electronic or other means is prohibited and is subject to penalties under law.

[2]Primary researcher and author.

[3]Assistant professor and advisor.

[4]Department of Mechanical Engineering, Iowa State University.

riorities over conventional sinusoidal fringe projection techniques for three-dimensional (3D) shape measurement. Yet, it is very difficult for them to produce high-quality 3D shape measurement when the fringe stripes are wide and when the projector is nearly focused (Wang and Zhang, 2012a). This is because for the binary defocusing techniques, binary patterns are fed to the projector and sinusoidal patterns are generated by properly defocusing the projector. However, due to the hardware limitation (projector lens can only be changed to a certain level), when the fringe stripes are wide, it is very difficult to generate high-quality sinusoidal patterns from these binary patterns through defocusing.

The aforementioned improved binary defocusing techniques (Wang and Zhang, 2010; Ajubi et al., 2010) are, after all, modifying the patterns in one dimension; yet the desired sinusoidal fringe patterns are two dimensional in nature. This indicates that if the binary patterns are modified in both dimensions, better sinusoidal patterns could be generated. Xian and Su demonstrated the area-modulated patterns can indeed generate high-quality sinusoidal fringe patterns with precise micro-manufacturing technique (Xian and Su, 2001). However, this technique requires the cell to be about 1 μm, which is still difficult to realize in a digital fringe projection system as the pixels are typically about ten times larger. William and Zhang proposed to approximate the triangular waveform by modifying 2×2 pixels (Lohry and Zhang, 2012), which showed the promise of improving 3D shape measurement quality when fringe stripes are narrow, but suffers if the fringe stripes are wide.

Dithering (Schuchman, 1964), also called halftoning, is the process of representing an image with fewer colors or bits than they are in the real image. This technique has been extensively employed in digital signal (e.g. audio, video) processing. Figure 5.1 shows the binary dithered images and their original grayscale ones. It indicates that the dithered images could represent the original images with good quality; and the binary pattern appears sinusoidal even before any processing. However, to our knowledge, there is no prior attempt to apply such a technique to 3D shape measurement. This paper is

thus the first to introduce the dithering technique to this community.

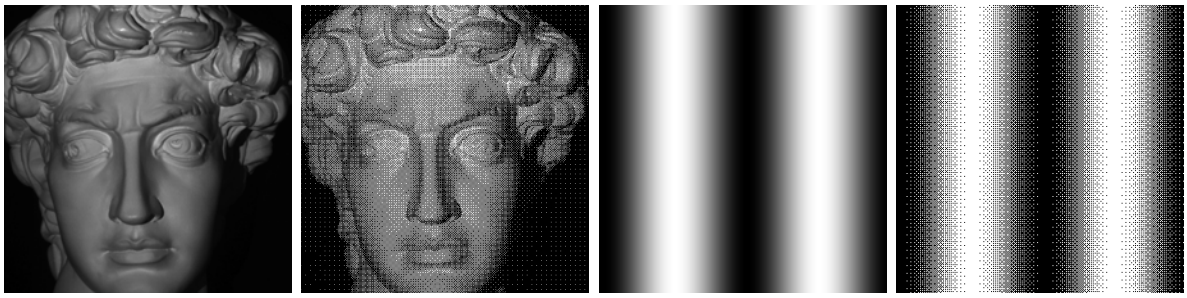

(a) (b) (c) (d)

Figure 5.1 Binary dithering technique for 8-bit grayscale images. (a) Original 8-bit image of David head; (b) Binary dithered image of (a); (c) Original 8-bit sinusoidal structured pattern; (d) Binary dithered pattern of (c).

We propose to apply the dithering technique to optimize binary patterns so that high-quality fringe patterns can be generated even when the stripes are very wide. Specifically, the desired sinusoidal fringe patterns are binarized using the ordered-dithering algorithm proposed by Bayer (Bayer, 1973). These binary dithered structured patterns are then sent to a nearly-focused or slightly defocused projector to produce ideal sinusoidal patterns, and then a fringe analysis technique can be used for high-quality 3D shape measurement. It is important to note that this paper only focuses on generating high-quality sinusoidal patterns with wide stripes for 3D shape measurement to overcome the problem of the existing binary defocusing technique, albeit the narrow ones can also be realized.

Section 5.3 presents the phase-shifting algorithm we are going to use. Section 5.5 shows some simulation result. Section 9.4 shows some experimental results, and Section 9.5 summarizes this paper.

5.3 Phase-Shifting Algorithm

We used a five-step phase-shifting algorithm to verify the performance of the the proposed technique. For a five-step phase-shifting algorithm with a phase shift of $2\pi/5$, the fringe patterns can be described as,

$$I_n(x,y) = I'(x,y) + I''(x,y)\cos(\phi + 2\pi n/5). \tag{5.1}$$

Where $n = 1, 2, ..., 5$, $I'(x,y)$ is the average intensity, $I''(x,y)$ the intensity modulation, and $\phi(x,y)$ the phase to be solved for using the following equation.

$$\phi(x,y) = \tan^{-1}\left[\frac{\sum_{n=1}^{5} I_n(x,y)\sin(2\pi n/5)}{\sum_{n=1}^{5} I_n(x,y)\cos(2\pi n/5)}\right]. \tag{5.2}$$

The arctangent function will result a value ranging $[-\pi, +\pi)$ with 2π discontinuities. A spatial or temporal phase unwrapping algorithm can be used to remove the 2π discontinuities, and then 3D shape can be reconstructed from the unwrapped phase if the system is calibrated.

5.4 Binary Dithering Technique

Conventionally, sinusoidal patterns are generated by the computer and projected by the projector in a digital fringe projection system. Recently, our research showed that the binary patterns can also be used for for high-quality 3D shape measurement when the projector is properly defocused. This technique is called the binary defocusing technique. The binary defocusing technique has many potential advantages: (1) no requirement for gamma calibration since only two grayscale values are used (Lei and Zhang, 2010); (2) no strict requirement for camera exposure time even when the digital-light-processing (DLP) projector is utilized (Gong and Zhang, 2010); and (3) possibilities of achieving unprecedentedly high-speed 3D shape measurement (Zhang et al., 2010). However, the binary defocusing technique is not trouble-free especially when the fringe stripes are wide

where the high-order harmonics cannot be effectively suppressed by defocusing due to the limitation of the projector lens (Wang and Zhang, 2012a).

Dithering, which is one technique used to achieve satisfactory image rendering and color reduction, has the potential to tackle the aforementioned problem of the squared binary technique. A structured sinusoidal fringe pattern is typically stored as an 8-bit image with 256 gray-scale values. In contrast, a binary pattern is an 1-bit image that only requires 2 gray-scale values to represent. To approximate a sinusoidal pattern with a binary pattern, various dithering techniques can be used, such as the simple thresholding (Purgathofer et al., 1994), the random dithering (Purgathofer et al., 1994), the Bayer-ordered dithering (Bayer, 1973), and the error-diffusion dithering (Kite et al., 2000) techniques. For the simple thresholding method (Purgathofer et al., 1994), each pixel grayscale value is compared against a fixed threshold value: if it is larger than the threshold, the pixel is set to be 1, otherwise to be 0. This technique is very simple, yet it results in immense loss of details and contouring. The random dithering technique (Purgathofer et al., 1994) could alleviate the problem of thresholding to some extent by comparing each pixel value against a random threshold. However, this technique still cannot preserve the details of the original image. The error-diffusion dithering technique (Kite et al., 2000) involves area operation since the quantization error residuals distribute to the neighboring pixels that have not been processed. Though working well for representing the grayscale images, the algorithm is not efficient since it is difficult to operate in a parallel manner.

Due to its good performance and easy operation, the Bayer ordered dithering technique (Bayer, 1973) was adopted in this paper. The ordered dithering consists of comparing blocks of the original image to a 2-D grid of thresholds called dither patterns. Each element of the original block is quantized according to the corresponding threshold value in the dither pattern. The values in the dither matrix are fixed, but are typically different from each other. Because the threshold changes between adjacent pixels, some

de-correlation from the quantization error is achieved. Bayer has shown that if the sizes of the matrices are 2^N (N is an integer), there is an optimal dither pattern that results in the pattern noise being as high-frequency as possible. It is well know that the high-frequency noise can be effectively reduced by applying a low-pass filter. The Bayer patterns can be obtained as follows,

$$M_1 = \begin{bmatrix} 0 & 2 \\ 3 & 1 \end{bmatrix}, \tag{5.3}$$

which is the smallest 2×2 base dither pattern. Larger dither patterns can be obtained using

$$M_{n+1} = \begin{bmatrix} 4M_n & 4M_n + 2U_n \\ 4M_n + 3U_n & 4M_n + U_n \end{bmatrix}, \tag{5.4}$$

where U_n is n-dimensional unit matrix. Using these standard dither patterns, a grayscale image can be efficiently quantized depending upon the chosen size of dither pattern.

Figure 5.2 shows the differences of different dithering techniques. Figure 5.2(b) shows the result after applying the simple thresholding technique to binarize the image. It can be seen that almost all details are lost. The random dithering technique improves the simple thresholding technique, yet a lot details are still missing, as shown in Fig. 5.2(c). The ordered Bayer dithering technique can well preserve most features of the original image. Figure 5.2(d) shows the result after applying the ordered Bayer dithering technique. The binarized image of Fig. 5.2(e) using the error-diffusion dithering technique can also well represent the original image.

5.5 Simulation Results

We firstly verified the performance of the proposed technique through simulations. Fringe patterns with wide fringe stripes are generated by the binary dithering algorithm (Bayer, 1973). Figure 5.3 shows two examples: one fringe pattern has a fringe

(a) (b) (c) (d) (e)

Figure 5.2 Binary dithering techniques for a 8-bit grayscale image. (a) Original 8-bit image of the David head; (b) Binary dithered image of (a) by applying the thresholding technique; (c) Binary dithered image of (a) by applying random dithering technique; (d) Binary dithered image of (a) by applying the Bayer ordered dithering technique; (e) Binary dithered image of (a) by applying the error-diffusion dithering technique.

pitch (T), number of pixels per fringe period, of 600, and the other has a fringe pitch of 150. Figures 5.3(a) and 5.3(d) show the dithered patterns and their associated Gaussian smoothed patterns. It is interesting to see that even before applying a Gaussian smoothing filter, the patterns visually appear good sinusoidality. Even though the Gaussian filter is quite small (size of 9×9 pixels with a standard deviation of 3.0 pixels), the resultant patterns depict clear sinusoidal structures. Figures 5.3(b) and 5.3(e) show the horizontal cross sections of the blurred patterns. To better visualize the sinusoidality of these blurred patterns, the frequency-amplitude spectra of cross sections were plotted in Figs. 5.3(c) and 5.3(f). These figures clearly show that high-frequency harmonics almost completely disappear, which means that they are good-quality sinusoidal.

We further simulated the influence of different amounts of defocusing by varying the Gaussian filter size (F_s) with the standard deviation being always $F_s/3$. The phase was calculated by using the aforementioned five-step phase-shifting algorithm; and the resultant phase errors are calculated by comparing with the phase obtained from the ideal sinusoidal fringe patterns. Figure 5.4(c) shows the root-mean-square (rms) error percentages. The error percentages were calculated as the ratios based of rms error and the total phase for the same size image. In our case, $T = 150$ has a total phase of 8π

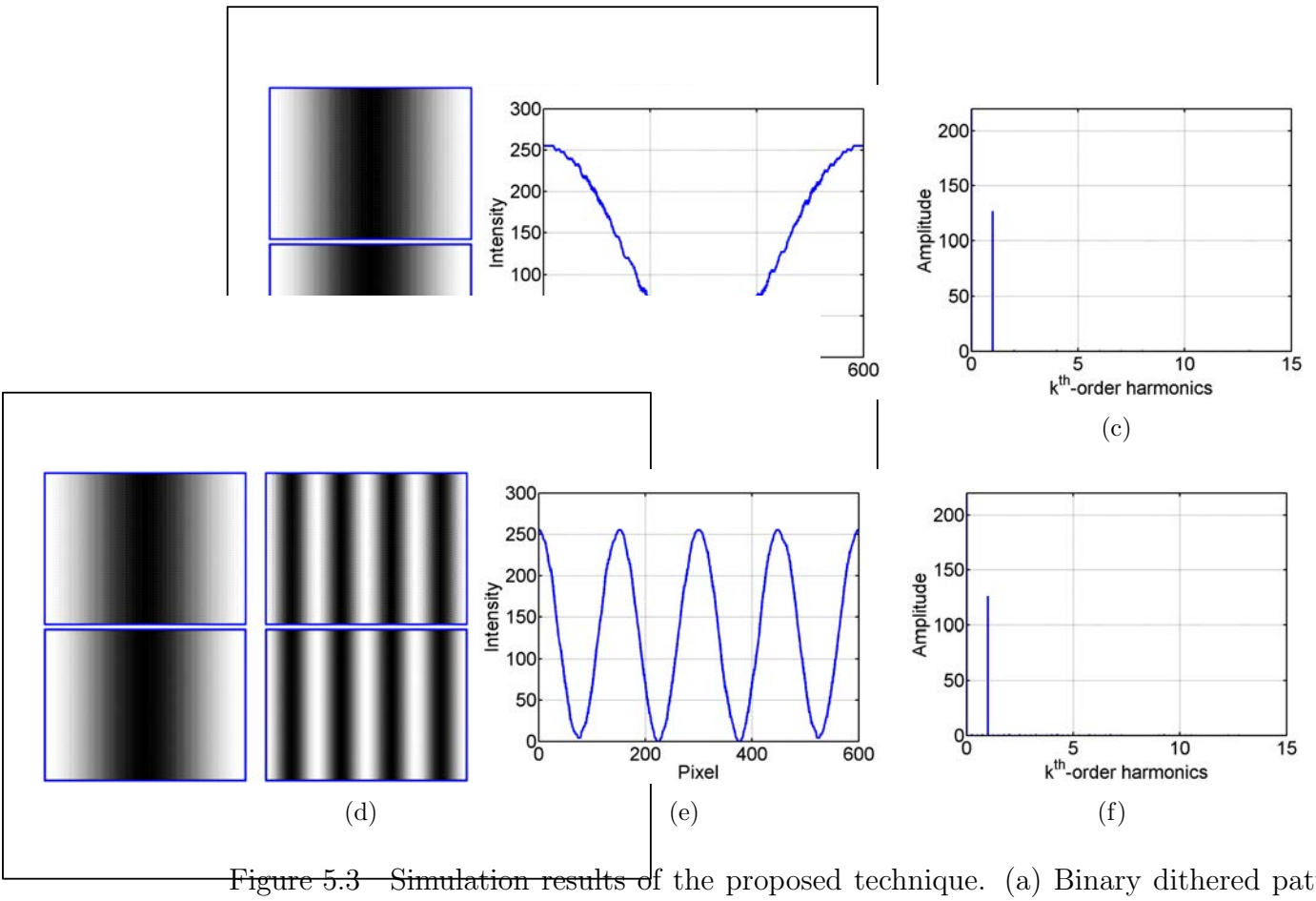

Figure 5.3 Simulation results of the proposed technique. (a) Binary dithered pattern and its smoothed pattern ($T = 600$), top image shows the dithered pattern and the bottom image shows the smoothed pattern; (b) Cross section of the blurred pattern; (c) Fourier spectrum of the cross section shown in (b); (d)-(f) Corresponding results to above image when $T = 150$.

and $T = 600$ has 2π since the image has a resolution of 600×600. In these simulations, we used filter sizes of $F_s = 5, 7, 11, 15, 19, 23, 27, 39$ pixels, for levels 1 through 8. These simulations show that 1) the phase errors are all very small (approximately 0.4% for $T = 600$ pixels) even when fringe patterns are almost in focus (top images in Figs. 5.4(a) and 5.4(b)); and 2) the phase error reduces when the patterns with the increase of amount of defocusing. This means that the proposed technique can be used for large depth range 3D shape measurement, because the measurement can start from almost in focus to signficantly defocused.

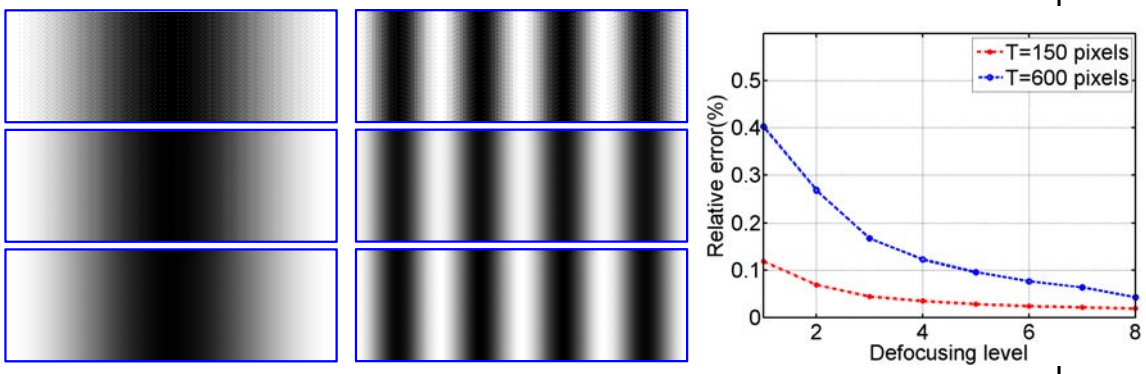

(b) (c)

Figure 5.4 Phase errors with varying amount of defocusing by simulations. (a) Fringe patterns ($T = 600$); (b) Fringe patterns ($T = 150$); (c) Phase error percentage. (a) and (b) from top to bottom show defocusing levels of 1, 4, 8, respectively.

5.6 Experimental Results

We also developed a 3D shape measurement system to verify the proposed method. In this system, we utilized a digital-light-processing (DLP) projector (Samsung SP-P310MEMX) and a digital CCD camera (Jai Pulnix TM-6740CL). The camera is attached with a 16 mm focal length Mega-pixel lens (Computar M1614-MP) with an image resolution is 640 × 480. The projector has 800 × 600 resolution and has 0.49-2.80 m projection distance.

The phase error caused by different amounts of defocusing was experimented first. In this experiment, a white flat board was measured, and the amount of defocusing was realized by manually adjusting the focal length of the projector. The projector was adjusted from nearly focused to significantly defocused. We used the dithered patterns generated in Fig. 5.3 and two fringe pitches ($T = 600$ and $T = 150$) to determine the phase error percentage for each case. The phase error is calculated, again, by comparing the phase obtained from the dithered patterns with the phase obtained the ideal sinusoidal fringe patterns. To reduce the noise influence of the ideal sinusoidal fringe patterns, the fringe pitch used for the ideal sinusoidal fringe patterns is much smaller ($T = 30$). Figure 5.5

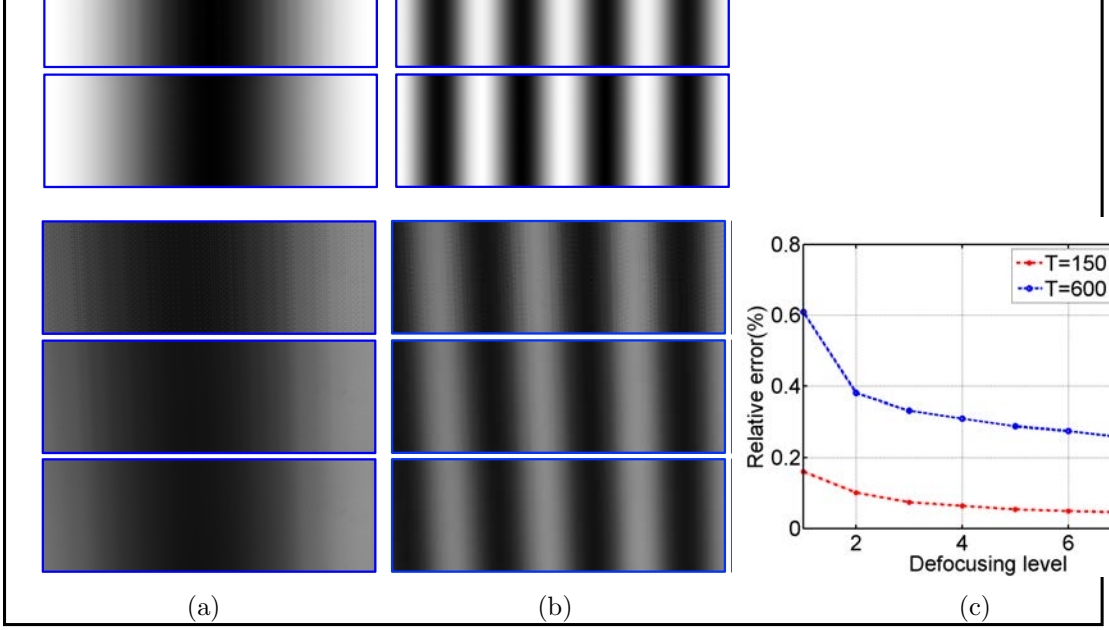

Figure 5.5 Phase errors with varying amount of defocusing by experiments. (a) Fringe patterns ($T = 600$); (b) Fringe patterns ($T = 150$); (c) Phase error percentage. (a) and (b) from top to bottom show defocusing levels of 1, 4, 8, respectively.

shows the results. It can be seen that the projector starts with nearly focused to significantly defocused, but the phase error all remain small (less than 0.6% even for the wide fringe, $T = 600$). Clearly, these experimental results are similar to our simulation results, and thus confirmed one merit of the proposed technique: suitable for large depth range 3D shape measurement.

We also measured a complex 3D object, David head shown in Fig. 5.1(a). Figure 5.6 shows the measuring results with different fringe breadths ($T = 600$, 150, and 60). During all the measurements, the projector and the camera remain untouched. To test our proposed technique, we firstly used the dithered patterns with projector being slightly defocused. Figures 5.6(a)-5.6(c) shows the representative captured fringe patterns with different fringe breadths. Five phase-shifted dithered patterns are captured and used to recover the 3D shape. Figures 5.6(d)-5.6(f) show the 3D result for each case. It is not necessary to unwrap the phase from the widest fringe patterns, because the single fringe covers the whole measurement range. The narrower phase maps are unwrapped with the assistance of the phase from the largest fringe period using a temporal phase-unwrapping algorithm. To convert the unwrapped phase to depth, we used a simple

phase-to-height conversion algorithm described in Reference (Xu et al., 2011). It is well known that when fringe stripes are wide, the random noise is very large; and with the fringe period decreasing, the quality of the 3D results becomes better. The experimental results shows that the 3D shape measurements are of very high-quality when the fringe period is $T = 60$.

To evaluate the measurement quality, we also did experiment using sinusoidal fringe patterns. Figures 5.6(g)-5.6(i) show the corresponding results with the same fringe size and the same phase-shifting algorithm. The nonlinearity of the projector was corrected using the approach described in Reference (Huang et al., 2003). This experiment clearly shows that the measurement quality using the proposed technique is comparable to that using the conventional techniques after projector's nonlinearity corrections; but the proposed technique does not need any nonlinearity correction because it naturally utilizes the binary patterns.

5.7 Conclusion

We have presented a novel 3D shape measurement technique using the binary dithered patterns and the phase-shifting technique. This method overcomes one of the challenges of the existing binary defocusing techniques: difficult to generate high-quality sinusoidal fringe pattern when fringe stripes are very wide. Both simulation and experimental results have demonstrated the success of the proposed method. This work was funded by National Science Foundation under projects number CMMI: 1150711.

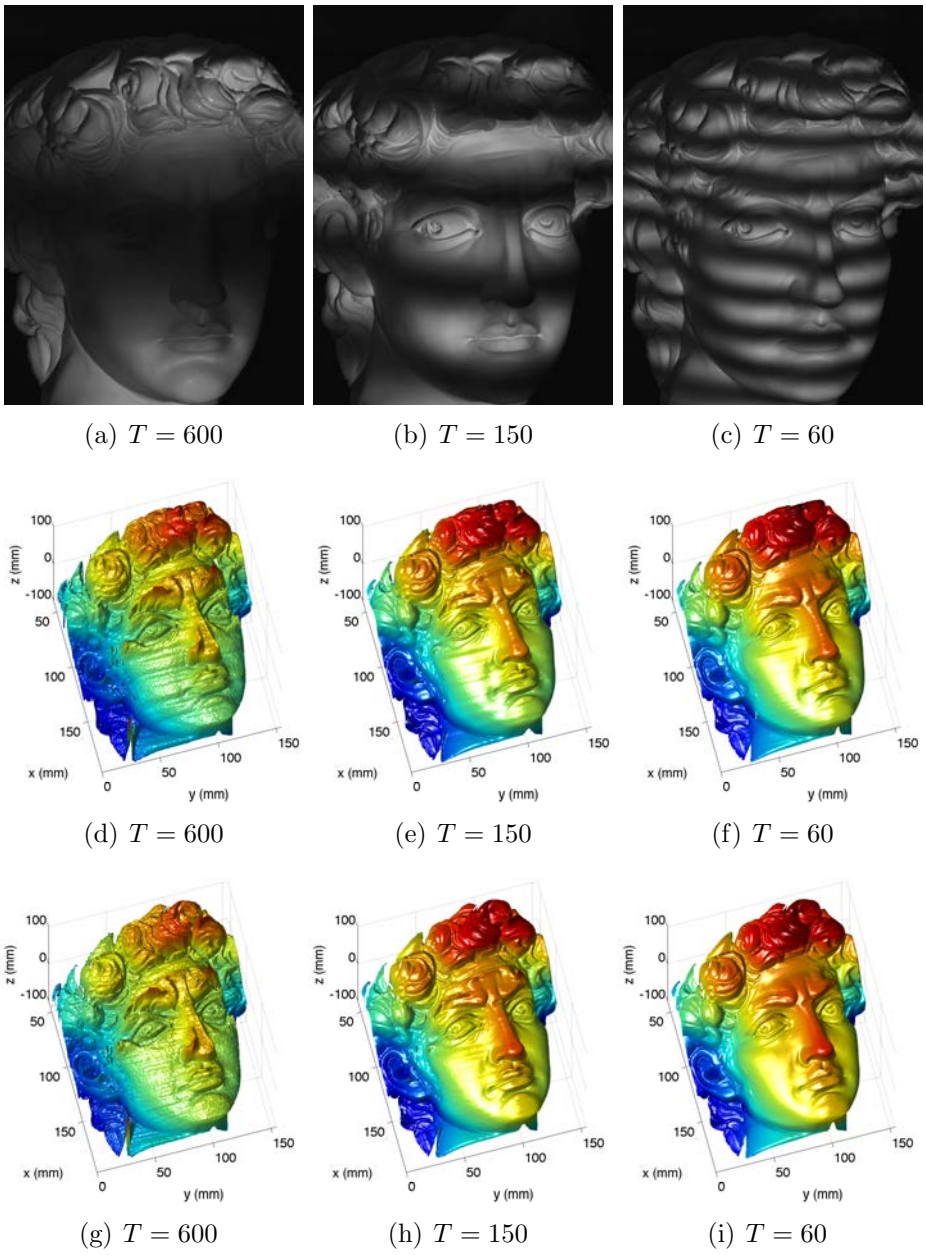

(a) $T = 600$ (b) $T = 150$ (c) $T = 60$

(d) $T = 600$ (e) $T = 150$ (f) $T = 60$

(g) $T = 600$ (h) $T = 150$ (i) $T = 60$

Figure 5.6 Experimental results of measuring a complex 3D object. (a)-(c) Representative captured dithered patterns; (d)-(f) 3D results using the dithered patterns; (g)-(h) 3D results using ideal sinusoidal patterns.

CHAPTER 6. OPTIMAL FRINGE ANGLE SELECTION FOR DIGITAL FRINGE PROJECTION TECHNIQUE

A paper published in the Journal of Applied Optics in October 2013.[1]

Yajun Wang[2,4] and Song Zhang[3,4]

6.1 Abstract

Existing digital fringe projection (DFP) systems mainly either use horizontal or vertical fringe patterns for three-dimensional (3D) shape measurement. Yet, this paper will reveal that these two fringe directions are usually not optimal where the phase change is the largest to a given depth variation. We propose a novel and efficient method to determine the optimal fringe angle by projecting a set of horizontal and vertical fringe patterns onto a step-height object and by further analyzing two resultant phase maps. Experiments demonstrate the existence of the optimal angle and the success of the proposed optimal angle determination method.

[2]Primary researcher and author.

[3]Assistant professor and advisor.

[4]Department of Mechanical Engineering, Iowa State University.

6.2 Introduction

Three-dimensional (3D) shape measurement is of great importance to the fields ranging from manufacturing to medicine (Quan et al., 2002; Hanafi et al., 2005). Numerous techniques have been developed including Moiré, holography, and digital fringe projection (DFP) techniques (Zhang, 2013). Among these 3D shape measurement methods, the DFP techniques have started to be a mainstream and be more adopted due to their simple setup, high-speed, and high-resolution measurement capabilities (Gorthi and Rastogi, 2010; Geng, 2011).

Conventionally, a DFP system usually uses a projector to project horizontal and/or vertical fringe patterns onto the surface of the object to be measured (Huang and Zhang, 2006; Su and Chen, 2001; Zhang and Su, 2005). By analyzing the captured distorted fringe images by a camera, the phase map can be obtained, from which the 3D depth information can be further retrieved if the system is calibrated. It is well known that the design of such a system is usually not easy and often involves complicated trial-and-error procedures. The optimal design essentially will provide the best sensitivity to depth variation. In other words, the phase changes are the largest for a given depth variation (i.e., maximize $\partial\Phi/\partial z$). To our knowledge, there is no attention has been paid towards orienting the projected fringe patterns such that the system can achieve the optimal performance.

This paper will reveal that the fringe angle plays a vital role in determining the optimal performance of the 3D shape measurement system with a DFP technique, and simply projecting horizontal or vertical fringe patterns may not be the best option. It becomes crucial to determine the optimal fringe angle for a given system setup without changing its mechanical design. This paper proposes a novel and efficient method to determine the optimal fringe angle. Specifically, by projecting a set of horizontal and vertical fringe patterns onto a step-height object, we obtain two phase maps, from which

the phase differences between the top and the bottom surface of the step height objects can be calculated. Finally, the mathematical vector operation on these phase differences can be used to determine the optimal projection angle. Our further study indicate that if the projected fringe stripes have the optimal angle, the phase is the most sensitive to the depth variations. On contrast, if the fringe stripes are perpendicular to the optimal fringe direction, the system is the least sensitive to the depth variations.

6.3 Phase-Shifting Algorithm

Phase-shifting methods are widely used in optical metrology because of their speed and accuracy (Malacara, 2007). A three-step phase-shifting algorithm with equal phase shifts can be described as,

$$I_1(x,y) = I'(x,y) + I''(x,y)\cos(\phi - 2\pi/3), \tag{6.1}$$

$$I_2(x,y) = I'(x,y) + I''(x,y)\cos(\phi), \tag{6.2}$$

$$I_3(x,y) = I'(x,y) + I''(x,y)\cos(\phi + 2\pi/3). \tag{6.3}$$

Where $I'(x,y)$ is the average intensity, $I''(x,y)$ the intensity modulation, and $\phi(x,y)$ the phase to be solved for. Simultaneously solving Eqs. (9.1)-(9.3) leads to:

$$\phi(x,y) = \tan^{-1}\left[\sqrt{3}(I_1 - I_3)/(2I_2 - I_1 - I_3)\right]. \tag{6.4}$$

The arctangent function will generates the phase value ranging $[-\pi, +\pi)$ with 2π discontinuities. A spatial phase unwrapping algorithm (Ghiglia and Pritt, 1998) can be used to remove the 2π discontinuities but has problems when the object surface has abrupt changes, or contains multiple isolated patches. This research adopted the multi-frequency algorithm using a temporal phase unwrapping algorithm to obtain the absolute phase map, $\Phi(x,y)$ (Wang and Zhang, 2011).

6.4 Optimal Fringe Angle Selection

A DFP system usually contains a digital video projection unit, a digital camera imaging unit, and a fringe processing or analysis unit. In a conventional DFP system, the computer generated fringe patterns are usually either horizontal or vertical, which are then projected by the video projector on the object surface. The camera captured fringe patterns are then analyzed by the computer to obtain the phase map, which can be further converted to 3D shape information once the system is calibrated. However, our research found that simply projecting horizontal or vertical fringe patterns might not be *optimal* if the camera and the projector are not positioned perfectly. Here the optimal performance means that the system is the most sensitive to the depth changes of the object surface, i.e., $\partial\Phi/\partial z$ is the largest for a given setup.

It should be noted that the projected patterns generated by a computer can be perfectly horizontal or vertical, but the captured fringe patterns by the camera may have small angle error (i.e., the fringe patterns may not be perfectly horizontal or vertical). The proposed optimal fringe angle determination method was based off the computer generated fringe patterns before sending to the projector, and thus the angle error can be negligible. Practically, if the projected fringe patterns are close to optimal angle, the phase change is nearly the largest with a given depth variation. In contrast, if the fringe angle is close to being perpendicular to optimal angle, the phase change is close to being zero with the same depth change, meaning that the measurement sensitivity is very low and the measurement accuracy is drastically jeopardized due to factors such as system noise and/or phase error.

To achieve high sensitivity, one can adjust the relative position and orientation between the projector and the camera, which is usually not easy. Instead of mechanically re-designing the system, we propose to change the projected fringe stripe orientation such that the system can achieve the best sensitivity. Specifically, we propose the following

procedures to determine the optimal fringe angle:

(1) Project horizontal and vertical fringe patterns onto a step-height object and a uniform flat reference plane; and obtain four absolute phase maps by employing a multi-frequency phase-shifting algorithm: horizontal absolute phase map of the object Φ_{Ho}, vertical absolute phase map of the object Φ_{Vo}, horizontal absolute phase map of the reference plane Φ_{Hr}, and vertical absolute phase map of the reference plane Φ_{Vr}.

(2) Calculate the difference phase maps by subtracting the object phase maps with the corresponding reference phase maps

$$\Delta\Phi_{Hd} = \Phi_{Ho} - \Phi_{Hr}, \tag{6.5}$$

$$\Delta\Phi_{Vd} = \Phi_{Vo} - \Phi_{Vr}. \tag{6.6}$$

(3) Compute the phase difference between top and bottom surfaces of the step object using the following equations

$$\Delta\Phi_{H} = \Delta\Phi^{t}_{Hd} - \Delta\Phi^{b}_{Hd}, \tag{6.7}$$

$$\Delta\Phi_{V} = \Delta\Phi^{t}_{Vd} - \Delta\Phi^{b}_{Vd}, \tag{6.8}$$

(4) Determine the optimal fringe angle using the following equation, which is illustrated in Fig. 6.1.

$$\theta_o = \tan^{-1}\left[\Delta\Phi_V/\Delta\Phi_H\right]. \tag{6.9}$$

This is essentially the angle of the vector $\vec{v} = \Delta\Phi_H\vec{i} + \Delta\Phi_V\vec{j}$. Here $\vec{i}$ and $\vec{j}$ are the unit vector along x and y axis, respectively.

As explained previously, if the projected fringe patterns use the optimal angle θ_o, the phase changes the greatest with the same amount of depth variation. Therefore, such a system can be used to measure the smallest features on an object surface for a given hardware system configuration. This finding is especially valuable for a DFP system where the orienting of the projected fringe patterns can be easily realized.

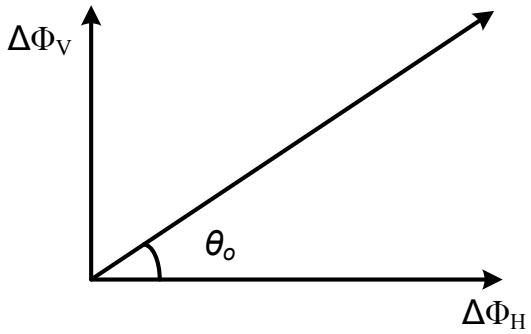

Figure 6.1 Calculation of the optimal fringe angle.

6.5 Experimental Results

We implemented such an optimal angle determination method to a DFP system. The system includes a digital-light-processing (DLP) projector (Samsung SP-P310MEMX) and a digital CCD camera (Jai Pulnix TM-6740CL). The camera uses a 16 mm focal length Mega-pixel lens (Computar M1614-MP). The camera resolution is 640 × 480, with a maximum frame rate of 200 frames/sec. The projector has a resolution of 800 × 600 with a projection distance of 0.49-2.80 m.

We used a standard step-height block to determined the optimal angle of our DFP system. The block size is approximately 40 mm (H) × 40 mm (W) × 40 mm (D). Figure 6.2 shows the measurement results using horizontal and vertical fringe patterns. Figure 6.2(a) and 6.2(d) respectively shows one of the horizontal and vertical fringe images captured by the camera. Figures 6.2(b) and 6.2(e) show the corresponding phase difference maps (Φ_{Hd} and Φ_{Vd}), which were obtained using Eqs. (6.5)-(6.6). To better illustrate the phase difference maps, Figure 6.2(c) and 6.2(f) respectively shows the same cross section of the phase map shown in Fig. 6.2(b) and 6.2(e).

Taking the difference between the top surface of the block and the bottom surface of the block, we can obtain $\Delta\Phi_H$ and $\Delta\Phi_V$, from which we can determine the optimal angle (θ_o) using Eq. (6.9).It should be noted that we used the averaged phase values for the phase difference determination on the step-height object to alleviate the noise effect.

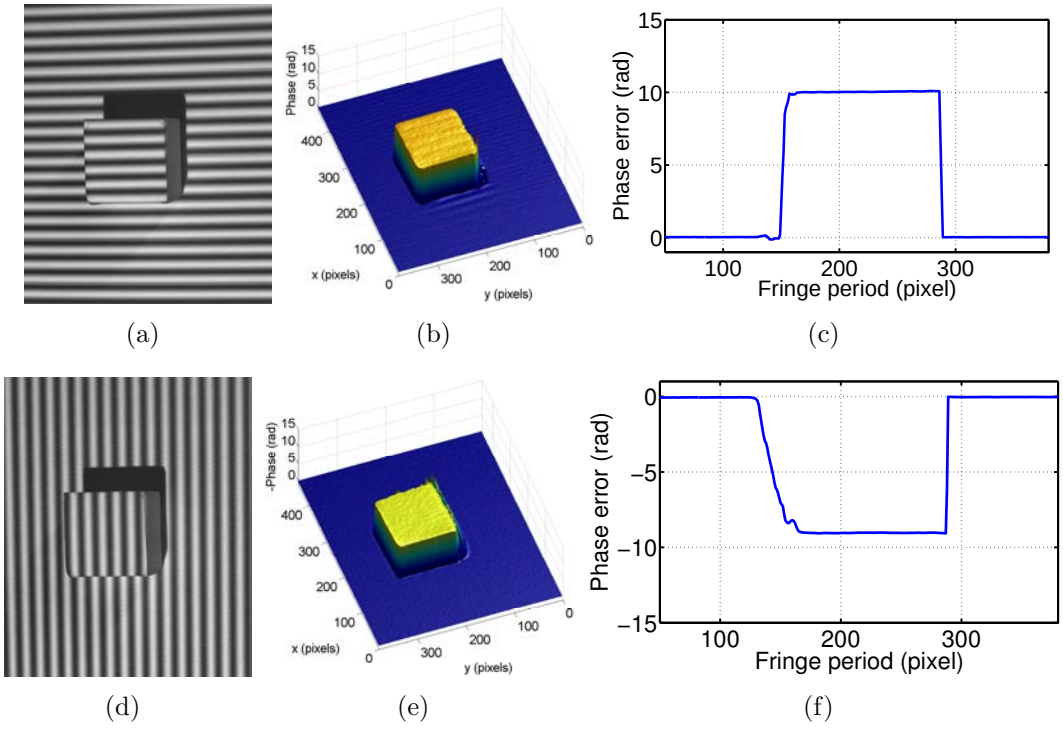

Figure 6.2 Phase measurements using horizontal and vertical fringe patterns. (a) One of the captured horizontal fringe patterns; (b) Phase difference map Φ_{Hd}; (c) 250-th row cross section of (b); (d) One of the captured horizontal fringe patterns; (e) Phase difference map Φ_{Vd}; (f) 250-th row cross section of (e).

Namely, we averaged the phase maps of a small area on the top surface and that on the bottom surface to calculate the phase difference for each fringe angle. In this case, the optimal fringe angle is approximately (θ_o = -0.73 rad). In contrast, if the fringe stripe is perpendicular to the optimal fringe stripe direction, the system is the least sensitive to the depth changes. In other words, if the fringe angle is (θ = 0.84 rad), the phase difference map of the step-height block should be close to zero.

We then experimentally verified the optimal angle we determined, and Figure 6.3 shows the results. Figure 6.3(a) and 6.3(d) respectively show one of the captured fringe images under the worst and optimal fringe angles. Figures 6.3(b) and 6.3(e) show the corresponding phase difference maps. The cross sections are shown in Fig. 6.3(c) and 6.3(f). These experiments shows that the phase difference is indeed close to zero if

the fringe direction is perpendicular to optimal fringe direction; and when the projected patterns use the optimal fringe angle, the phase difference is drastically larger than either the horizontal or the vertical fringe patterns we normally use, as illustrated in Fig. 6.2. It should be noted that during all experiments, the whole hardware system remained untouched, the object was positioned the same location, and the fringe period was the same. These data demonstrated that we can determine the optimal fringe angle, and the system is the most sensitive to the depth variation under the optimal condition.

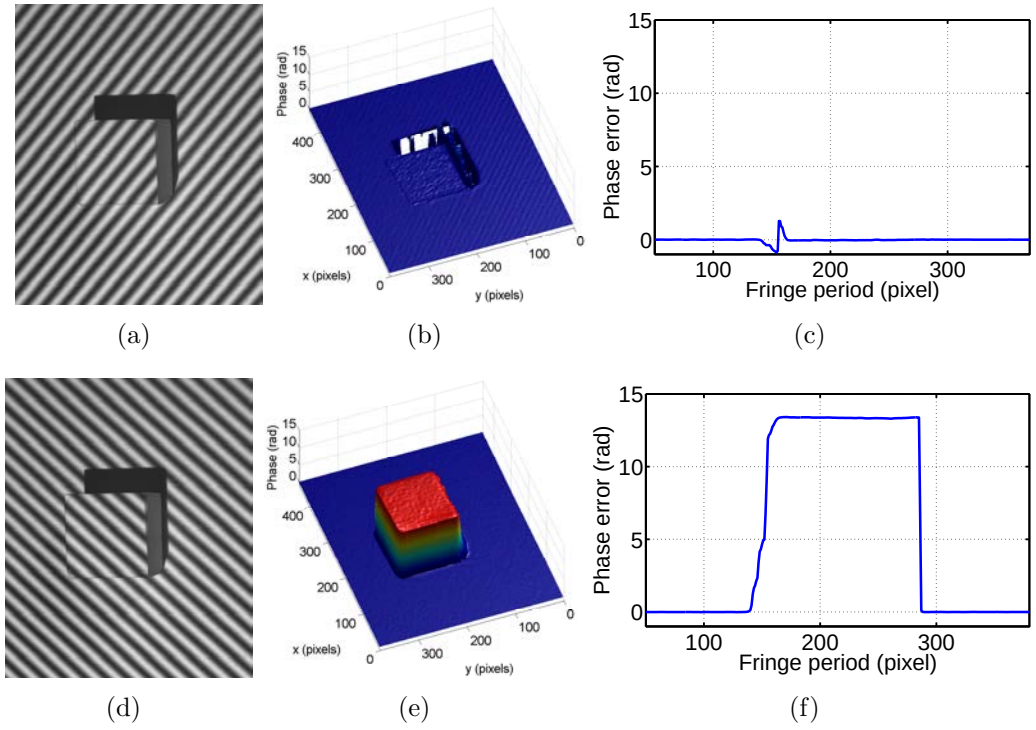

Figure 6.3 Results for the fringe patterns with the worst and the optimal fringe angles. (a) One of the captured fringe images with $\theta = 0.84$ rad, the worst fringe angle; (b) Phase difference map of (a); (c) 250-th row cross section of (b); (d) One of the captured fringe images with $\theta_o = -0.73$ rad, the optimal fringe angle; (e) Phase difference map of (d); (f) 250-th row cross section of (e).

A more complex sculpture was also measured using the optimal fringe angle and the worst fringe angle, as shown in Fig. 6.4. Figures 6.4(a) and 6.4(d) show one of the captured fringe patterns and Figs. 6.4(b) and 6.4(e) show the corresponding phase

difference maps. It can be seen that the phase difference map is nearly flat and no details are obvious on Fig. 6.4(b) when the worst fringe angle is used. In contrast, Figure 6.4(e) clearly shows the highly detailed features on the difference map when the fringe patterns use the optimal fringe angle. We further convert phase difference maps to the depth maps using the simple phase-to-height conversion algorithm discussed in Ref. (Xu et al., 2011). The depth scaling coefficient was obtained using optimal fringe angle, and applied to both phase difference maps. Figure 6.4(c) and 6.4(f) respectively shows the worst and the best result. It clearly shows that using the optimal fringe angle, the 3D object can be properly measured with details. Yet, if the fringe orientation rotates 90 degrees, 3D shape cannot be properly recovered at all since the phase difference map is close to be zero across the whole range.

6.6 Discussions

As demonstrated in Section 6.5, the phase sensitivity is significantly improved when the optimal angle is used. Theoretically, if the system is perfectly linear and the fringe angle is perpendicular to the optimal fringe angle, no 3D shape measurement can be performed since the fringe patterns will not be distorted by object surface geometry; and if no noise presents in a measurement system, even if the fringe angle is not optimal, the measurement accuracy probably will not be changed. However, practically, noise always presents, and the measurement accuracy could be affected by the fringe angle.

Assume the phase error caused by the system noise is $\delta\Phi_e$, which is the same once the system is setup for a given phase-shifted fringe patterns. For a simple reference-plane based calibration method, the relationship between the depth z and the phase difference is $z = z_0 + c \times \Delta\Phi$ (Xu et al., 2011), here z_0 is the constant shift, and c is the calibration constant. Therefore, the depth error caused by the system noise is approximately $\Delta z_e = c \times \delta\Phi_e$. This indicates that the larger the calibration constant, the

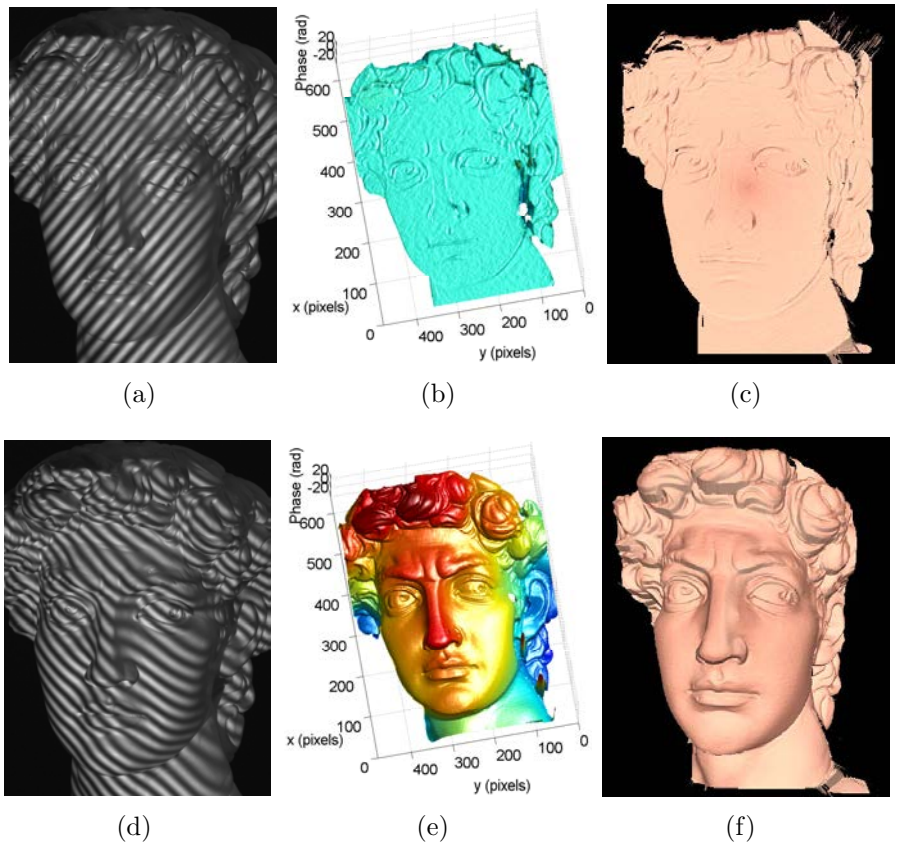

Figure 6.4 Sculpture results under different fringe angles. (a) One of the captured fringe patterns with the worst fringe angle $\theta = 0.84$ rad; (b) Phase difference map ($\theta = 0.84$ rad) (c) Recovered 3D shape ($\theta = 0.84$ rad); (d) One of the captured fringe patterns with the optimal fringe angle $\theta_o = -0.73$ rad; (e) Phase difference map ($\theta_o = -0.73$ rad); (f) Recovered 3D shape ($\theta_o = -0.73$ rad).

larger the measurement error will be induced by noise (i.e., the lower the measurement accuracy will be achieved). When the phase sensitivity ($\partial\Phi/\partial z$) is higher, the calibration constant c is smaller, and thus depth measurement accuracy is higher.

One may notice that Chen et al. (Chen et al., 2008) proposed a method to enhance the measurement quality by avoiding frequency aliasing of the Fourier transform profilometry (FTP) through changing fringe orientations. The objective of that paper was to avoid frequency aliasing. Since frequency spectrum is also affected by the object surface geometry, the fringe angle determined by such an approach depends on not only the

system set up, but also the object surface geometry. Therefore, the optimal fringe orientation should be determined for each individual measurement object. In contrast, our paper is a systematic approach that is completely independent of the measured object surface geometry. Once the system is setup, the optimal angle can be determined using the proposed approach.

6.7 Conclusion

We have presented a novel and effective method to determine the optimal fringe angle for a DFP technique. Experimental results have demonstrated the feasibility of the proposed method, and the capability of the proposed method to enhance the phase sensitivity to depth variations.

CHAPTER 7. ACCURATE CALIBRATION FOR 3D SHAPE MEASUREMENT SYSTEM USING A BINARY DEFOCUSING TECHNIQUE

A paper published in the Journal of Optics and Lasers in Engineering in May 2013.[1]

Leah Merner[2,5], Yajun Wang[3,5] and Song Zhang[4,5]

7.1 Abstract

This paper introduces a novel method to calibrate 3D shape measurement systems that use the binary defocusing technique. Specifically, this method calibrates the pixel-wise z as low-order polynomial functions of absolute phase; (x, y) coordinates are calculated from camera calibration with known z value; and the camera is calibrated using the standard flat checkerboard method. Because this method does not require estimation of the projector's parameters, it can be adopted for any phase measurement system including those employing out-of-focus projectors. Our experiment found that the root-mean-squared (rms) error for the depth measurement is less than 70 μm when the measurement depth range is about 100 mm, which is at the same level of the calibration

[1]This paper was published in the Journal of Optics and Lasers in Engineering and is made available as an electronic reprint with the permission of Elsevier. The paper can be found at the following URL on the Elsevier website: http://www.sciencedirect.com/science/article/pii/S0143816612003041. Systematic or multiple reproduction of distribution to multiple locations via electronic or other means is prohibited and is subject to penalties under law.

[2]Undergraduate student collaborator.

[3]Primary researcher and author.

[4]Assistant professor and advisor.

[5]Department of Mechanical Engineering, Iowa State University.

stage $\pm$ 50 μm.

7.2 Introduction

Precise measurement applications in manufacturing and medical sciences increasingly integrate real-time 3D shape measurement systems based on digital sinusoidal fringe projection. The DFP technique offers good measurement accuracy, improves computation speed over many other 3D shape measurement techniques, and eliminates image matching difficulties of traditional stereo-vision systems by replacing one camera with a projector (Zhang, 2010b). These advances in 3D shape measurement create opportunities for application of digital fringe technologies in high precision measurement. However, the drawbacks of a conventional DFP technique include projector nonlinear gamma errors, difficult synchronization between projector and camera, and speed limitations of the projector, which may drastically affect measurement quality (Lei and Zhang, 2010).

The recently proposed binary defocusing technique could alleviate the problems of conventional DFP techniques in that the projector nonlinearity does not affect measurement accuracy, the time modulation effect of the digital light-processing (DLP) technique is less sensitive to precise synchronization, and 1-bit instead of 8-bit data transfer reduces DLP projector's processing power demand (Xu et al., 2011). However, the binary defocusing technique introduces a new challenge: calibrating such a system becomes more difficult because of the use of an out-of-focused projector since most well-established, accurate calibration methods for structured light systems require the projector to be in focus (e.g. the least squares (Guo et al., 2005; Huang et al., 2010), projector image regeneration (Zhang and Huang, 2006b; Yang et al., 2008; Gao et al., 2008; Li et al., 2008), and camera-projector system optimization (Hu et al., 2003; Cuevas et al., 2000; Legarda-Saenz et al., 2004)). The calibration accuracy usually determines the accuracy of a 3D shape measurement system; thus, an accurate calibration method is vital to

any precision 3D shape measurement system. The reference-plane based phase-to-height conversion methods (Zhang et al., 2002) could be used if the depth measuring range is small (Zhang and Huang, 2006b). However, the calibration accuracy is low if the measuring depth range is large. Therefore, a new calibration technique must be developed for the binary defocusing technique before it can be extensively adopted.

We propose a novel method for accurately calibrating a 3D shape measurement system using the binary defocusing technique by a method that indirectly calibrates the defocused projector. Specifically, the proposed method includes two stages: depth z calibration and (x, y) coordinates calibration. The first stage is calibrating z coordinate information by translating a calibration plane over known depths, recording the depth z values and absolute phase values per pixel for each plane, and fitting a curve for each pixel across the entire depth range to establish the depth z and the absolute phase. We found that the depth z per pixel can be described as 3rd- or 4th- order polynomials of the absolute phase value; therefore, the depth z can be accurately recovered once the polynomial functions are calibrated. The second stage is to calibrate (x, y) coordinates, which is a standard camera calibration method. We employed the checkerboard camera calibration method proposed by Zhang (Zhang, 2000) and estimated the camera's intrinsic and extrinsic parameters using the Matlab software package developed by Bouguet (Bouguet,). If the camera calibration depth z is aligned with the first calibration procedure, (x, y) coordinates can be computed using the calibrated camera parameters. Our experiment found that the root-mean-squared (rms) error for the depth measurement is less than 70 μm, which is at the same level of the calibration stage ± 50 μm.

7.3 Principle

7.3.1 Nine-Step Phase-Shifting Algorithm

Phase-shifting algorithms are widely used in optical metrology because of their measurement speed and accuracy (Malacara, 2007). Numerous phase-shifting algorithms have been developed including three-step, four-step, double-three-step, and five-step algorithms. In this research, we use a nine-step phase-shifting algorithm to reduce the influence of random noises and high-frequency harmonics during defocusing. The nine phase-shifted fringe images can be described as

$$I_n(x,y) = I'(x,y) + I''(x,y)\cos(\phi + 2\pi n/9), \tag{7.1}$$

where $I'(x,y)$ is the average intensity, $I''(x,y)$ the intensity modulation, $\phi(x,y)$ the phase to be solved for, and $n = 1, 2, ..., 9$. The phase, $\phi(x,y)$ can be solved for as follows:

$$\phi(x,y) = \tan^{-1}\left[\frac{\sum_{n=1}^{9} I_n(x,y)\sin(2\pi n/9)}{\sum_{n=1}^{9} I_n(x,y)\cos(2\pi n/9)}\right]. \tag{7.2}$$

Equation 9.4 provides the phase ranging $[-\pi,\ \pi)$ with 2π discontinuities. This 2π phase jumps can be removed to obtain the continuous phase map by adopting a phase unwrapping algorithm, such as one of the algorithms described in Book (Ghiglia and Pritt, 1998). The phase unwrapping is essentially to determine the locations of the phase jumps and remove them by adding or subtracting multiples of 2π. However, the phase obtained by a spatial phase unwrapping is relative phase. In this research, absolute phase is required for accurate calibration.

7.3.2 Absolute Phase Recovery with Gray Coding

The conventional unwrapping method only recovers the relative phase for each pixel. It is sensitive to noise and cannot measure step heights greater than π, which may introduce large measurement errors. Instead, recovering the absolute phase, $\Phi(x,y)$, can

avoid these errors and provide a more robust solution. Methods such as two- or multi-wavelength (Creath, 1987; Cheng and Wyant, 1985), optimal multifrequency (Towers et al., 2003), temporal phase-unwrapping (Huntley and Saldner, 1993), and gray-coding plus phase-shifting (Sansoni et al., 1999) methods can recover the absolute phase. This chapter uses the gray-coding plus phase-shifting method to obtain the fringe order for absolute phase retrieval in order to maintain the merits of the binary defocusing technique where only binary patterns are needed. Specifically, a sequence of designed binary coding patterns uniquely defines the location of each 2π phase jump to create a fringe order, $k(x, y)$, so that the phase can be recovered pixel by pixel by referring to the binary coded patterns.

$$\Phi(x, y) = \phi(x, y) + k(x, y) \times 2\pi. \tag{7.3}$$

7.3.3 Establishment of the Relationship Between Absolute Phase and Depth

Previous research has shown that the absolute phase and the depth are monotonically related per camera pixel (Xu et al., 2011). Therefore, geometrical models can describe the relationship between the absolute phase and the depth, and vice versa (Mao et al., 2007). Then the calibration process is to retrieve the parameters in the models. However, due the complexity of the real projection system, the models are always not very accurate with some assumptions, which would bring errors for the final calibration accuracy. Previous research found that this relationship of the absolute phase and the depth is non-linear and can be approximated with low-order polynomials (Xu et al., 2011; Sitnik et al., 2002):

$$z(x, y) = \sum c_k(x, y) \cdot \Phi(x, y)^k. \tag{7.4}$$

Here $c_k(x, y)$ are constants to be estimated by calibration.

Figure 7.1 shows absolute phase and depth are related monotonically and nonlinearly, verifying that curve fitting calibration could accurately describe depth z coordinate information.

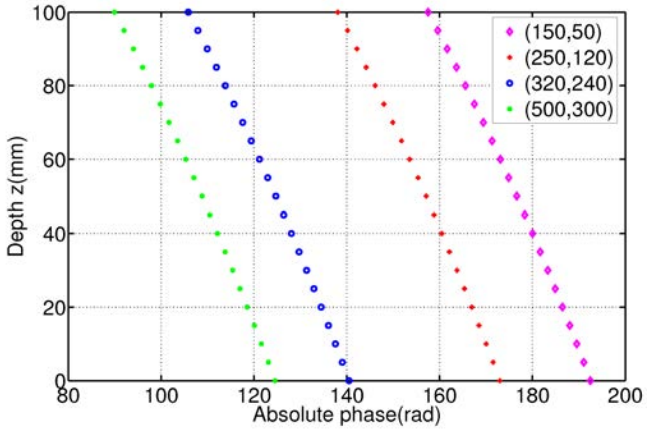

Figure 7.1 Absolute phase $\Phi(x, y)$ vs. depth z for four arbitrary pixels.

In our experiments, five different curve fitting cases were examined: linear interpolation, 2nd- , 3rd- , and 4th-order polynomials. The remaining experiments for this chapter use the best performing fitting method. It is interesting to note that Zhang et al. proposed a calibration technique that uses linear interpolation to define the relationship between *relative phase* and depth (Zhang et al., 2005). This technique could provide good accuracy if the increments between calibration planes are small enough (i.e., the nonlinear curves can be approximated as linear segments). However, as shown in Fig. 7.1, the relationship between phase and depth is nonlinear and other curve fitting methods could generate better calibration accuracy. By fitting a curve across all calibration planes that define the depth range, the z coordinate can be accurately calibrated per pixel.

7.3.4 Camera Parameters Estimation for x and y Calibration

Typically, the pinhole camera model describes a camera with intrinsic parameters, such as focal length, principle point, pixel skew factor; and extrinsic parameters defining camera rotation and translation between a world coordinate system used to unify x, y and z calibration and the camera coordinate system (Zhang, 2000). A 3D point in world coordinate system can be denoted by $M = [x,\ y,\ z]^T$, and the corresponding 2D point in camera coordinate system is $m = [\mu,\ \nu]^T$. By adding 1 as the last element, the

augmented vectors are: $\widetilde{M} = [x,\ y,\ z,\ 1]^T$ and $\widetilde{m} = [\mu,\ \nu, 1]^T$. The relationship between a 3D point $\widetilde{M}$ and its image projection m is given by

$$s\tilde{m} = A[R\ \ T]\tilde{M}, \tag{7.5}$$

where s is a scale factor, $[R, T]$ is the extrinsic matrix, R is the 3×3 rotation matrix, and T is the translation vector. A is the camera intrinsic matrix that can be described as

$$A = \begin{bmatrix} \alpha & \gamma & \mu_0 \\ 0 & \beta & \nu_0 \\ 0 & 0 & 1 \end{bmatrix}. \tag{7.6}$$

Here α and β are respectively the focal lengths along x and y axis, γ is the camera skew factor, and (u_0, v_0) is the principal point where the optical axis intersects with the camera sensor.

Once the extrinsic and intrinsic matrices are determined through calibration, the world coordinate system and camera coordinate system can be accurately matched. If camera parameters are obtained, x and y information can be determined by

$$s \begin{bmatrix} \mu \\ \nu \\ 1 \end{bmatrix} = A[R,\ T] \begin{bmatrix} x \\ y \\ z \\ 1 \end{bmatrix}. \tag{7.7}$$

In this equation, because z is a known value obtained through a curve fitting procedure, (x, y) can be uniquely solved. Because this technique does not require precise determination of the corresponding projector pixel, it can be used to calibrate any phase measurement system including the DFP system with projector being out-of-focus. It should be noted that direct projector calibration is not required; thus, the technique can be applied to any phase measurement system.

7.4 Experiments

7.4.1 System Setup

The structured light system used in our experiments consisted of a digital-light-processing (DLP) projector (Samsung SP-P310MEMX) and digital USB charge-coupled-device (CCD) camera (Jai Pulnix TM-6740CL). The camera uses a 16 mm focal length Mega-pixel lens (Computar M1614-MP). The camera resolution is 640 × 480 with a maximum frame rate of 200 frames/sec. The projector has a resolution of 800 × 600 with a projection distance of 0.49-2.80 m. Figure 7.2 shows the calibration system setup. The field of view of the projector and camera are respectively 405 mm × 295 mm and 220 mm × 160 mm.

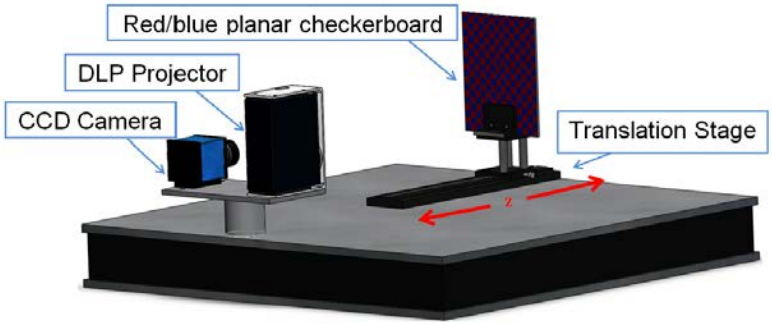

Figure 7.2 Calibration system setup.

The projector projected fringe pattern onto a laser-printed red/blue checkerboard pattern attached to a nearly planar surface. The planar surface was attached to a precision TECHSPEC Metric long travel linear translation stage. The stage is 250 mm long with a traveling accuracy of ±0.05 mm. The flat object with red/blue checkerboard attached is mounted on top of the translation stage and manually moved along the z (depth) axis.

7.4.2 z Coordinate Calibration

The translation stage was moved toward the structured light system and data was captured in 5 mm increments from $z_0 = 0$ mm (farthest point from camera and projector) to $z_{20} = 100$ mm. 21 calibration planes were captured. Of the 21 planes, 11 and 6 evenly spaced planes in the $z_0 - z_{20}$ range were used for curve fitting with different curve fitting methods (i.e. linear interpolation and polynomial fitting). Due to lens distortion and other factors, the absolute phase-depth curve for each pixel varies, so a curve was fit to each similar pixel on the calibration planes. With the remaining planes, the average fitting error per plane was calculated for each curve fitting method by subtracting the captured depth value from the experimental value determined through the curve fitting.

The accuracy of z calibration was evaluated for four different curve fitting methods: linear interpolation, 2nd-, 3rd-, and 4th-order polynomials. The average depth calibration error was calculated when using evenly spaced calibration planes for curve fitting, but the amount of space between the calibration planes was changed. Figure 7.3(a) shows calibration error for the four curve fitting methods when 11 interpolation planes were used. The planes were space 10 mm apart. Figure 7.3(b) shows calibration error for the four curve fitting methods when 6 interpolation planes were used spaced 20 mm apart.

From the experimental results, linear interpolation, 3rd-, and 4th-order polynomials fit the absolute phase-depth relationship with reasonable accuracy; however, 3rd- and 4th order polynomials produce a slightly more accurate fitting method (a maximum absolute average depth error of 0.064 mm for 3rd-order polynomial compared with 0.098 mm obtained by linear interpolation).

As the number of calibration planes decreases, low-order polynomial curve fitting represents the z coordinate data significantly more accurately compared to linear interpolation. Figure 7.3(b) shows the calibration depth errors when 6 interpolation planes were used. In this experiment, the maximum absolute average depth error for linear

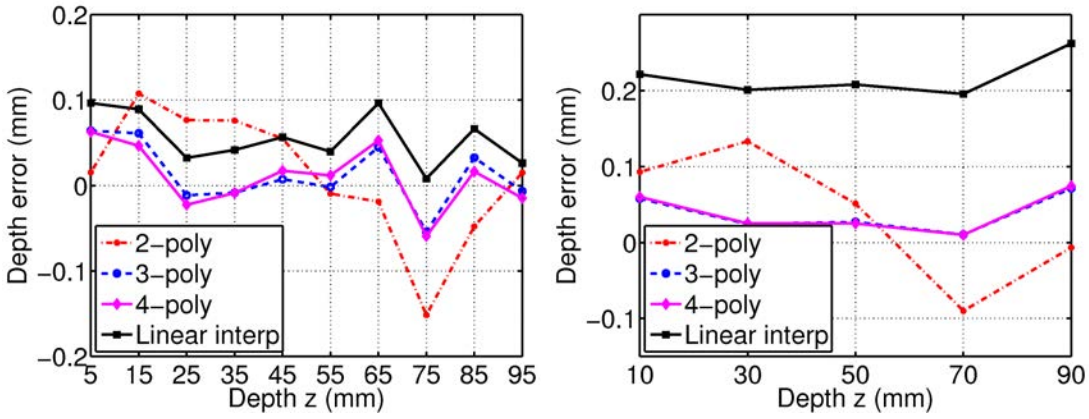

(a) (b)

Figure 7.3 Average depth error per plane using different curve fitting methods. (a) RMS error when 11 interpolation planes were used; (b) RMS error when 6 interpolation planes were used.

interpolation was 0.260 mm compared to 0.070 mm for 3rd-order polynomial. This is because the absolute phase-depth relationship is nonlinear, and if fewer calibration planes are used, the nonlinear effect is exaggerated and not well defined by linear interpolation.

For traditional sinusoidal fringe projection technique, it could be true that increasing the polynomial's order generates less error, albeit requires more calibration planes. However, for our binary defocusing technique, our experimental data showed that the error with 3rd-order polynomials already returns error close to that of the linear translation stage and using higher order polynomials will not lead to increased overall accuracy but will increase the depth z interpolation computation time and complexity. This finding was also experimentally verified by the prior study by Xu et. al (Xu et al., 2011). Therefore, the remaining experiments curve fit using 3rd-order polynomials.

It should be noted that during the depth z calibration stage, the projected fringe patterns are monochromatic so that the red/blue checkers will not appear. The red/blue printed color contrast was previously calibrated based on the system setup to ensure that when the projector is projecting monochromatic images, the checkers disappear.

7.4.3 x and y Coordinate Calibration

After z calibration, x and y coordinates can be calibrated using the procedure explained in Sec. 7.3.4. The z_0 plane, located at 0 mm for z calibration, is manually adjusted in the algorithms to $z_0 = 50$ mm. This step is essential to unify the coordinate systems used in z calibration and x and y calibration. Then, the captured calibration plane at location z_0 used in z interpolation is set as the reference for Zhang's optimization procedure (Zhang, 2000). It is important to notice that during this stage of calibration, the red/blue checkerboard was illuminated with red light so that the checkers will appear as regular checkerboard. 11 more images of the red/blue checkerboard calibration plane are captured at different orientations for calibrating the intrinsic and extrinsic parameters (see Fig. 7.4). The intrinsic and extrinsic parameters were optimized using the 12 captured images in an optimization algorithm.

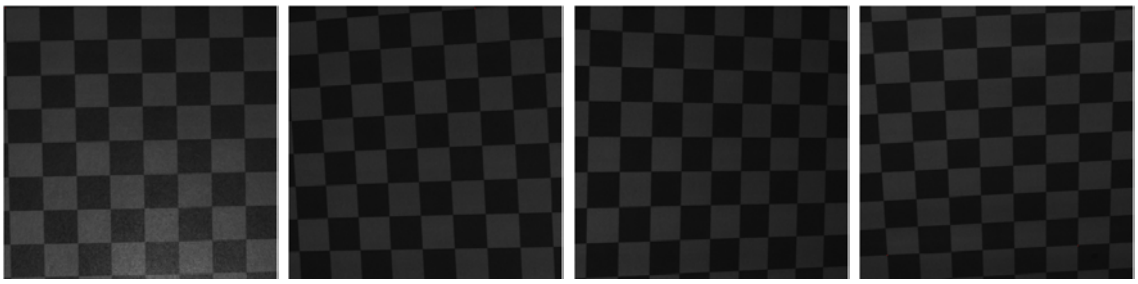

(a) (b) (c) (d)

Figure 7.4 Example of four images of plane used in camera calibration set at different angles.

To test the calibration accuracy, four pixels in the corners on the checkerboard were chosen, as shown in Fig. 7.5. The top left corner pixel and the bottom right pixel forms Diagonal 1 (line AD). The other two corner pixels form Diagonal 2 (line BC). From Eq. 7.7, (x, y, z) information of all the four corners can be obtained. Then the lengths of both diagonals can be calculated, as shown in Table 7.1.

From the results, the (x, y, z) coordinate measurement accuracy was fairly good:

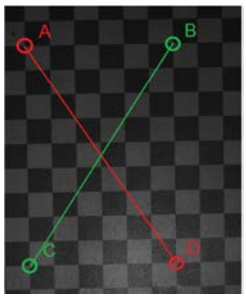

Figure 7.5 The measured diagonals.

approximately 1.6% error. However, comparing with depth z accuracy, (x, y) calibration accuracy is much lower. Moreover, one might notice that the average values calculated from Eq. 7.7 are smaller than the measured values. This could be caused by the camera calibration error. The variation of Diagonal 2 is larger than Diagonal 1. This could result from the distortion of camera lens, which was not considered in our camera calibration algorithm. One should notice that the goal is to provide a more accurate calibration method for depth z; thus, z calibration was given higher priority. If one wants to increase (x, y) calibration as well, a better camera calibration approach could be adopted.

7.4.4 3D Shape Reconstruction

To further verify the depth calibration accuracy, we also did an experiment to measure a step height object as shown in Fig. 7.6. Figure 7.6(a) shows the photo of the object, and the 3D reconstruction result is shown in Fig. 7.6(b). The step height is about 40.00 mm measured by a digital caliper, while the calibrated result is 40.29 mm. The relative error is about 0.7%.

Figure 7.7 shows the 3D shape reconstruction of a sculpture. Figure 7.7(a) shows one of the nine fringe patterns and Fig. 7.7(b) shows one of the coding patterns. Figure 7.7(c) shows the extracted absolute phase map, and the recovered 3D result is shown in Fig. 7.7(d). Figure 7.7 along with Fig. 7.6 demonstrate that the proposed calibration technique allows the 3D shape measurement system to accurately reconstruct 3D models

	Diagonal 1 (mm)	Diagonal 2 (mm)
1	134.51	134.52
2	134.16	135.93
3	134.08	136.43
4	134.80	133.36
5	135.33	132.86
6	136.33	132.55
7	135.94	137.90
8	135.39	137.28
9	135.26	136.59
10	134.05	132.22
11	134.00	133.06
12	134.33	135.93
Average	134.84	134.88
Variation	0.79	2.02
Measured$^\sharp$	137.01	137.18

Table 7.1 Measurement accuracy verification for four corner points. $^\sharp$ values are obtained from a high-accuracy digital caliper

with high resolution and accuracy.

7.5 Conclusion

This chapter has presented a novel method for calibrating a structured light system using the binary defocusing technique. Our procedure curve fits z coordinate information between selected planes in a known range. x and y coordinates are then calibrated by an optimization procedure to find extrinsic and intrinsic camera parameters. With the proposed method, we have demonstrated that a 3D model be accurately reconstructed. Proper calibration of a structured light system using the defocusing technique may help realize the advanced capabilities of defocusing technology over traditional sinusoidal fringe projection. This calibration method can also be adopted for traditional fringe projection techniques. It should be noted that badly defocused binary patterns will introduce significant phase errors that may couple and reduce measurement accu-

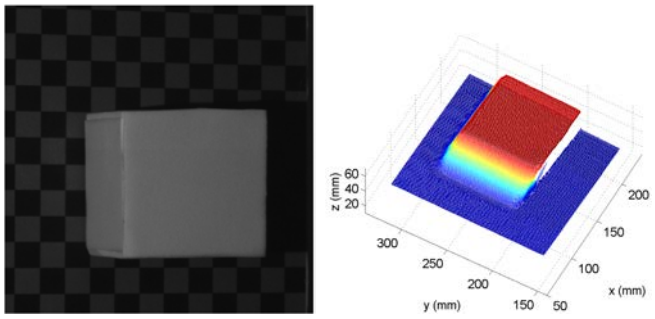

(a) (b)

Figure 7.6 3D shape measurement result of a step-height object. (a) Step-height object; (b) 3D result.

(a) (b) (c) (d)

Figure 7.7 3D shape measurement results of a complex object. (a) One fringe pattern; (b) One coding pattern; (c) Absolute phase map; (b) 3D reconstruction results.

racy. For our experiments, we used binary patterns with a small pitch as well as nine-step phase shifting to reduce errors introduced by the high order harmonics present in binary patterns. Future work may combine phase error compensation with the proposed calibration technique.

CHAPTER 8. DIGITAL MICROMIRROR TRANSIENT RESPONSE INFLUENCE ON SUPERFAST 3D SHAPE MEASUREMENT

A paper submitted to the Journal of Optics and Lasers in Engineering in October 2013.[1]

Yajun Wang[2,8], Bhaskar Bhattacharya[3,8], Eliot H. Winer[4,8], Peter Kosmicki[5,6], Wissam H. EI-Ratal[5,6], and Song Zhang[7,8]

8.1 Abstract

Nowadays, the high speed (kHz) refreshing rate of the digital micro-mirror device (DMD) has enabled superfast 3D shape measurement using the binary defocusing technique. This research finds that when the system reaches its extreme binary pattern refreshing rate, the transient response of the DMD induces a coupling effect (i.e., two neighboring patterns blend together) that may cause substantial measurement error. Since this transient response repeats itself, this systematic measurement error is substantially reduced to a negligible level when the timing between the projector and the camera is properly adjusted. Experimental results are presented to demonstrate the ob-

[1]This paper was submitted to the Journal of Optics and Lasers in Engineering in October 2013.
[2]Primary researcher and author.
[3]Graduate student collaborator.
[4]Associate professor and Bhaskar Bhattacharya's advisor.
[5]Collaborator.
[6]John Deere Product Engineering Center, Waterloo, IA.
[7]Assistant professor and Yajun Wang's advisor.
[8]Department of Mechanical Engineering, Iowa State University.

served phenomena, and the success of utilizing the proposed method to overcome the problems associated with the transient response of the DMD.

8.2 Introduction

The capture of 3D geometric motion of rapidly changing events is used considerably in academia. This new process started to impact the industry by enabling the acquisition of a new type of data that is vital to the development of new products. For instance, capturing the motion of a live beating heart is vital to understanding its mechanics and physiology (Wang et al., 2013a). Real-time 3D shape measurement has been realized by adopting the digital fringe projection (DFP) method facilitated by digital light processing (DLP) projectors (Zhang, 2010b; Li et al., 2010). However, it is extremely difficult for conventional DFP techniques to achieve rates higher than 120 Hz (which is the maximum refresh rate of a digital video projector). Therefore, it is difficult for such techniques to achieve high speed motion capture.

Recent advances in superfast 3D shape measurement have allowed high speed (in the order of kHz or higher) measurement rates by utilizing coherent laser interference and rotating mirrors (Schaffer et al., 2013), LED projection arrays (Heist et al., 2013), and digital binary pattern projection by the digital light processing (DLP) projectors (Zhang et al., 2010). All these technologies have utilized phase-shifting algorithms to achieve high-spatial resolution. The laser interference based technology (Schaffer et al., 2013) has the issue associated with the coherent lasers: speckle noise, albeit they partially reduced this problem by adding a second camera. The LED projection system (Heist et al., 2013) could reach 100 kHz, yet the system they developed only reached 47 Hz due to the camera they used, and possibly the brightness of the projectors and some transient response of the LED light used. We have successfully developed a system (Zhang et al., 2010) that could achieve 32 kHz using the DLP Discovery platform and the binary defocusing

technique (Lei and Zhang, 2009). However, the core of the DLP technology is the digital micro-mirror device (DMD) that is inherently a mechanical device that toggles the pixel ON or OFF by mechanically flipping the micro-mirrors from one position to the other. This transient response of the digital micro-mirrors could influence the measurement quality as well if its speed limit is reached.

The binary defocusing technique has enabled us to achieve high speed (in the order of tens of kHz) 3D shape measurement because it requires only 1-bit structured patterns rather than 8-bit grayscale patterns (Zhang et al., 2010). However, the measurement error is large if the projector is not properly defocused (Xu et al., 2011). Techniques based on 1-D pulse width modulation (PWM) (Wang and Zhang, 2010; Ajubi et al., 2010; Zuo et al., 2012, 2013), 2D area modulation (Xian and Su, 2001; Lohry and Zhang, 2012), and binary dithering (Wang and Zhang, 2012b) as well as the optimized dithering techniques (Lohry and Zhang, 2013; Dai et al., 2014) have been developed to improve the binary defocusing technique. They prove successful in attaining high-quality 3D shape measurement even if the projector is nearly focused; and if the projector is slightly defocused, the phase quality obtained from the binary patterns could be the same as that obtained from the traditional sinusoidal fringe patterns. Our prior knowledge tells us on how to reduce the phase measurement error to a negligible level caused by the binary defocusing itself. Therefore, the phase measurement error discussed in this paper is mainly caused by sources other than the defocused binary patterns.

This paper presents a new phenomena that we have never observed before for super-fast 3D shape measurement. Our experiments find that even if the binary patterns are properly selected and defocused, significant phase measurement error still occurs if the high-speed projectors (e.g., DLP LightCommander, DLP LightCrafter) operate under the structured light mode and pattern switching rate is at its maximum with the maximum illumination time. We discover that the transient response of the DMD causes pattern coupling (i.e., two neighboring patterns blend together) when the projector operates un-

der the aforementioned conditions. Further experiments find that the transient response is a systematic error (i.e., an error caused independent of the projection speed), and thus its influence on phase measurement error could be reduced if the proper method is developed. This paper presents a method that we have developed to mitigate this problem by changing the timing of the system: the exposure time of the projector, the starting time and exposure time of the camera. We will demonstrate that this method can reduce the phase measurement error to a negligible level.

Section 9.3 explains the principles of proposed techniques. Section 9.4 shows some experimental results, and Section 9.5 summarizes the paper.

8.3 Principle

8.3.1 Two-Frequency Phase-Shifting Technique for Absolute Phase Retrieval

Phase-shifting methods have been extensively adopted in optical metrology because of their measurement speed and accuracy. Over the years, a variety of phase-shifting algorithms have been developed, that include three-step, four-step, and least-square algorithms (Malacara, 2007). For high-speed 3-D shape measurement, a three-step phase-shifting algorithm with a phase shift of $2\pi/3$ is commonly used. The three fringe images can be described as:

$$I_1(x,y) = I'(x,y) + I''(x,y)\cos(\phi - 2\pi/3), \tag{8.1}$$

$$I_2(x,y) = I'(x,y) + I''(x,y)\cos(\phi), \tag{8.2}$$

$$I_3(x,y) = I'(x,y) + I''(x,y)\cos(\phi + 2\pi/3). \tag{8.3}$$

Where $I'(x,y)$ is the average intensity, $I''(x,y)$ the intensity modulation, and $\phi(x,y)$ the phase to be solved for. Simultaneously solving Eq. (9.1)-(9.3), the phase can be obtained

$$\phi(x,y) = \tan^{-1}\left[\sqrt{3}(I_1 - I_3)/(2I_2 - I_1 - I_3)\right]. \tag{8.4}$$

This equation provides the wrapped phase with 2π discontinuities. A spatial or temporal phase unwrapping algorithm can be applied to obtain continuous phase.

We utilized a two-frequency temporal phase-unwrapping algorithm to unwrap the phase. Essentially, two wrapped phase maps, low frequency phase ϕ^l and high-frequency $\phi^h(x, y)$ were used. $\phi^l(x, y)$ is obtained from wide fringe patterns with a single fringe covering the whole measuring range, such that no phase unwrapping is required. By referring to $\phi^l(x, y)$ point by point, $\phi^h(x, y)$ is unwrapped to obtain a continuous phase map, $\Phi(x, y)$. Because 3D information (i.e. the depth) is carried on by the phase, 3D shape can be reconstructed from the unwrapped phase $\Phi(x, y)$ using a phase-to-height conversion algorithm (Xu et al., 2011).

8.3.2 Fundamentals of the DLP Technology

Digital light processing (DLP) concept originated from Texas Instruments (TI) in the later 1980's. TI began its commercialized DLP technology in 1996. At the heart of every DLP projection system is an optical semiconductor called the digital micro-mirror device (DMD), which functions as an extremely precise light switch. The DMD chip contains an array of hinged, microscopic mirrors, each of which corresponds to one pixel of light in a projection image.

Figure 8.1 shows the working principle of the micro mirror. The micro mirror can be moved to $+\theta_L$ (ON) or $-\theta_L$ (OFF) , thereby modulating the output light corresponding to that cell. The rate of a mirror switching ON and OFF determines the brightness of the projected image pixel. Gray-scale values are produced by controlling the proportion ON and OFF times of the mirror during one projection period (black being 0% ON time and while white being 100% ON time).

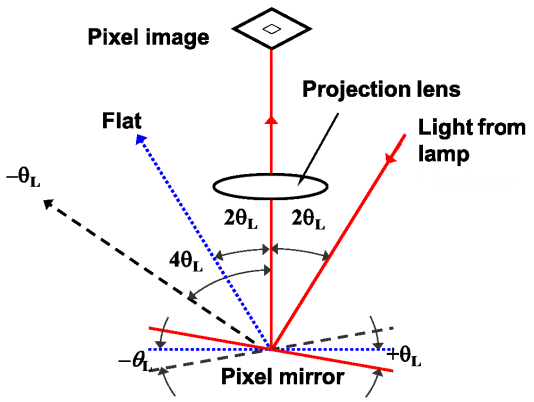

Figure 8.1 Optical switching principle of a digital micro-mirror device (DMD).

8.3.3 Fundamentals of the Binary Defocusing Technique

For a conventional DFP technique, sinusoidal patterns are projected and captured for 3D information extraction. Since it requires to project 8-bit sinusoidal patterns, the refresh rate of a digital video projector is typically limited to 120 Hz, which is not sufficient for high-speed motion measurement. The recently proposed binary defocusing technique is able to break the speed limitation for DFP technique. Instead of sending 8-bit sinusoidal patterns, 1-bit binary patterns are fed to the projector. By properly defocus the projector, the projected patterns will be pseudo-sinusoidal. Figure 8.2 shows the results with different defocusing levels. The first row of Fig. 8.2 shows the captured defocusing binary patterns, while the second row of Fig. 8.2 shows the corresponding cross sections.

Since only 1-bit binary patterns are used, there are some techniques which can be used for high-speed pattern projection. For example, the DLP LightCommander projector can switch binary patterns at 4 kHz, while it can only project sinusoidal patterns at about 700 Hz. By using the binary defocusing technique, we have demonstrated the feasibility for superfast motion capture (Zhang et al., 2010). However, when operating under high speed, there are limitations for some projectors, which may bring error to the final measurement result. In the following sections of this paper, we will demonstrate the

limitation of a DLP LightCommander projector along with our proposed solution.

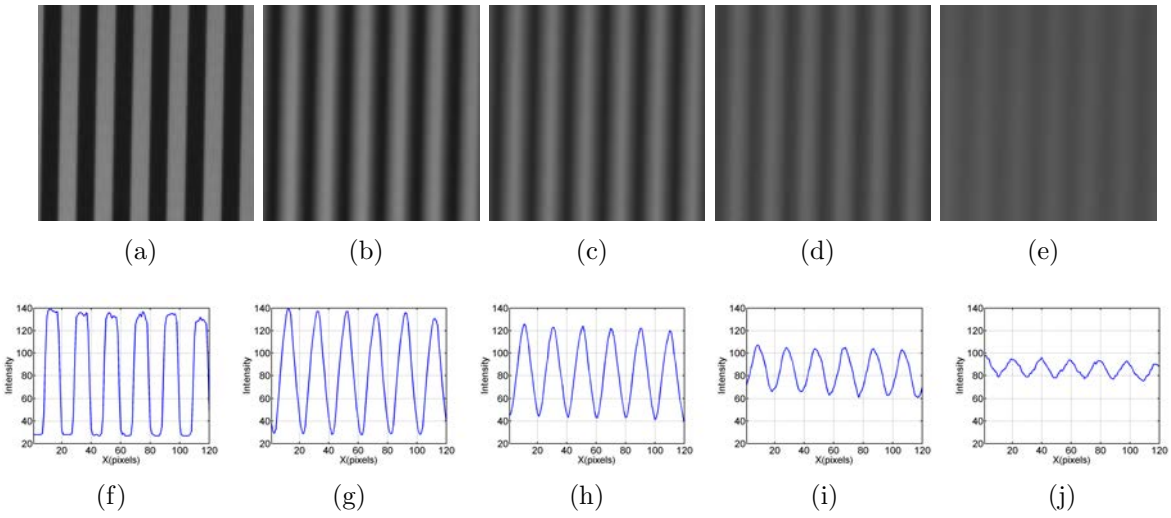

Figure 8.2 Binary defocusing patterns with different defocusing levels.

8.4 Experiments

8.4.1 Experimental System Setup

The developed 3D shape measurement system is composed of a DLP LightCommander projector (model: LightCommander, LogicPD, MN), a high-speed CMOS camera (model: Phantom V9.1, Vision Research, NJ). The projector contains a high performance light engine comprised of a core optical module and the LED illumination modules. It is capable for binary pattern projection up to 4 kHz, with a 1024 × 768 resolution. The camera offers 1016 frames per second (fps) at a full resolution of 1632 × 1200 pixels, up to 153846 fps maximum. In our experiments, we used a 576 × 576 image resolution. The synchronization circuit takes the projection timing signal and sends the trigger signal to the camera for simultaneous image acquisition. Both of the projector and the camera are attached with a Nikon 50 mm f/1.8 AF lens. Figure 8.3 shows the system that was developed.

The experimental results we will present are all based on the LogicPD LightCommander projector. However, our investigation on other high-speed DLP projectors (i.e., DLP LightCrafter 3000 and DLP LightCrafter 4500, Texas Instruments, TX) also observed similar phenomena, albeit at different significance levels. Therefore, the findings in this research is not limited to the DLP LightCommander projector.

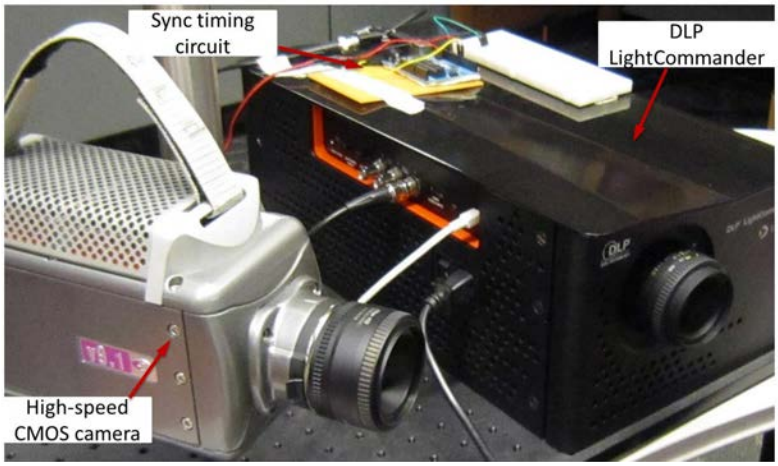

Figure 8.3 The 3D shape measurement system.

8.4.2 Transient Response of the DMD with Binary Image Input

In our previous research, we found that when the DLP LightCommander projector operates under a high speed (kHz) with the maximum exposure time, the patterns captured by a well synchronized high-speed camera will be coupled with adjacent frames. Since the phase information is extracted from several adjacent patterns, the coupling effect will cause phase errors. In order to understand the transient response of the DMD of the LightCommander projector, we carried out a simple experiment by placing a photodiode (model: Thorlabs FDS100; with a resistor:30 KΩ) in front of the projector. Care was taken that the photodiode was not placed too close to the projector where reflections becomes an issue or too far where the intensity of light was too dim. An oscilloscope (model: Tektronix TDS2024B) was used to visualize and record the signal of the photo-

diode system as the projector projected patterns under different speeds and illumination times.

In this experiment, two patterns of pure white and pure black were alternately sent to the projector. In an ideal case, a periodic square wave should be observed. During the white (first half) projection cycle the response should be high while during the black (second half) projection cycle, the response should fall immediately to zero. In other words, the recorded voltage signal should be as close to a square wave as possible. However, the voltage signals recorded under different projection speeds and illumination times as shown in the Fig. 8.4 are not ideal, which reveal the complex transient response of the DMD.

Figure 8.4(a)-8.4(c) shows the results of respectively 2 kHz, 1 kHz, and 500 Hz with their maximum allowed illumination time (494 μs , 994 μs, and 1994 μs). Figure 8.4(d)-8.4(f) shows the corresponding results by using a shorter illumination time (200 μs, 300μs, and 800 μs). As per Fig. 8.4(a)-8.4(c), we find if the maximum illumination time is used, when the projection pattern is switched from white to black, the DMD chips require a long time to respond by toggling to the off position. This effect which we term as a *coupling effect* is especially evident with projection speeds of over 1 kHz since the projected light is not able to fall to zero. However, if we use a shorter illumination time, the results begin to show improvement as shown in Fig. 8.4(d)-8.4(f). Take the result in Fig. 8.4(f) as an example, in the white projection cycle, the DMD chips toggle on for half the cycle and before the next half cycle, they have enough time to toggle off. Therefore, for the adjacent black cycle, the DMD chips always toggle off. In this way, if the camera is well synchronized with the projector, the captured patterns will have no coupling effects. It is worthwhile to note that, for the experiments in the following sections, the projector was set and compared at the same conditions with this section.

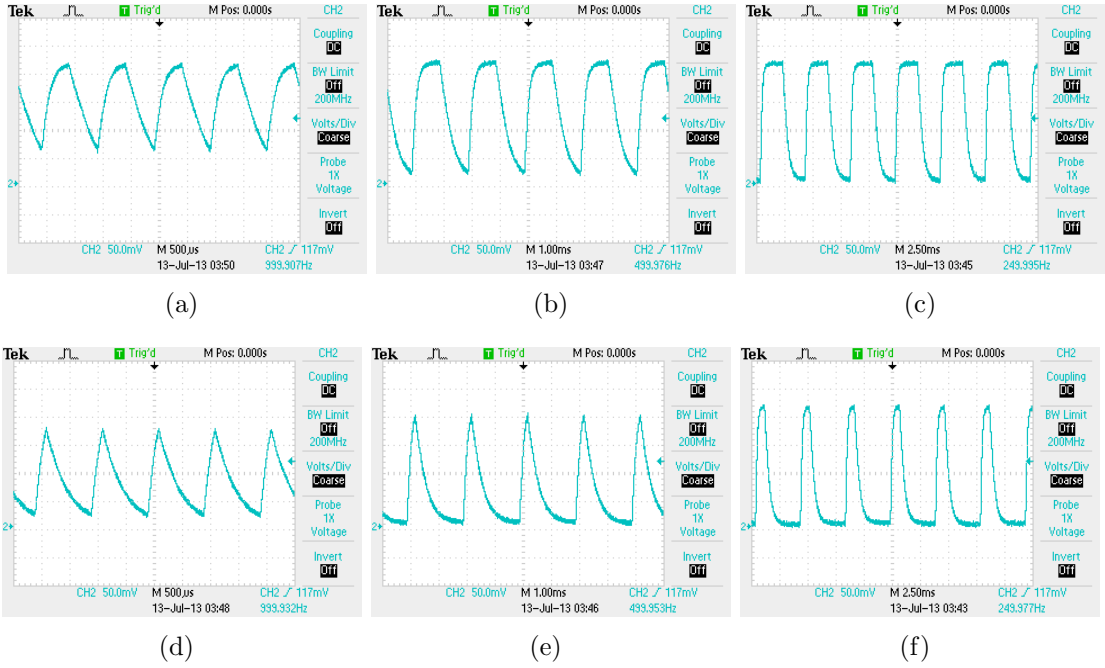

Figure 8.4 Transient responses of the DMD of DLP LightCommander projector. (a) 2000 FP (2 kHz projection rate with 494 μs illumination time); (b) 1000 FP (1 kHz projection rate with 994 μs illumination time); (c) 500 FP (500 Hz projection rate with 1994 μs illumination time); (d) 2000 SP (2 kHz projection rate with 200μs illumination time); (e) 1000 SP (1 kHz projection rate with 300μs illumination time); (f) 500 SP (500 Hz projection rate with 800μs illumination time).

8.4.3 Coupling Effect

To visually justify the coupling effects, we did experiments by projecting fringe patterns with two different fringe pitches (18 pixels and 300 pixels). In this experiments, the camera was synchronized with the projector, and the exposure time of the camera was set to the maximum under different speeds (i.e., 494 μs for 2 kHz, 994 μs for 1 kHz, and 1994 μs for 500 Hz). For the projector, we tested the same conditions as in Fig. 8.4. Figure 8.5 shows the patterns captured under those different conditions. Specifically, Fig. 8.5(a)- 8.5(c) shows the patterns captured under different projection speeds of respectively 2 kHz, 1 kHz, and 500 Hz with the maximum illumination time. It clearly shows that the patterns overlap with their adjacent neighbors. Fig. 8.5(d)-8.5(f)

show the corresponding patterns with a shorter illumination time. Unlike the previous case, these patterns are visibly unhindered, which means that the coupling effects are significantly alleviated.

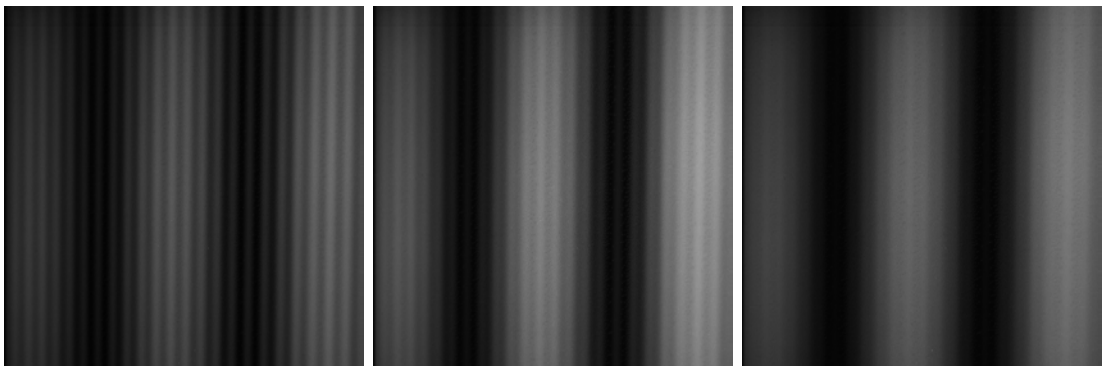

(a) (b) (c)

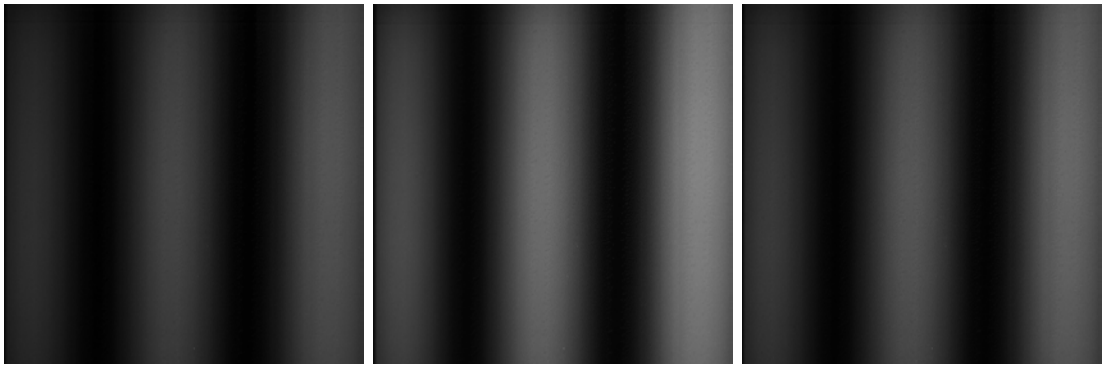

(d) (e) (f)

Figure 8.5 Captured low spatial frequency fringe patterns that shows the coupling effect under different conditions.(a) 2 kHz projection rate with 494 μs illumination time; (b) 1 kHz projection rate with 994 μs illumination time; (c) 500 Hz projection rate with 1994 μs illumination time; (d) 2 kHz projection rate with 200μs illumination time; (e) 1 kHz projection rate with 300μs illumination time; (f) 500 Hz projection rate with 800μs illumination time.

To better view the difference between those patterns shown in Fig. 8.5, their corresponding cross sections are plotted as shown in Fig. 8.6. In Fig. 8.6(a) and 8.6(b), we can clearly see there are wavelets overlapping the sinusoidal wave. From Fig. 8.6(c)-8.6(f), the sinusoidal wave becomes smoother without any obvious overlapping wavelets.

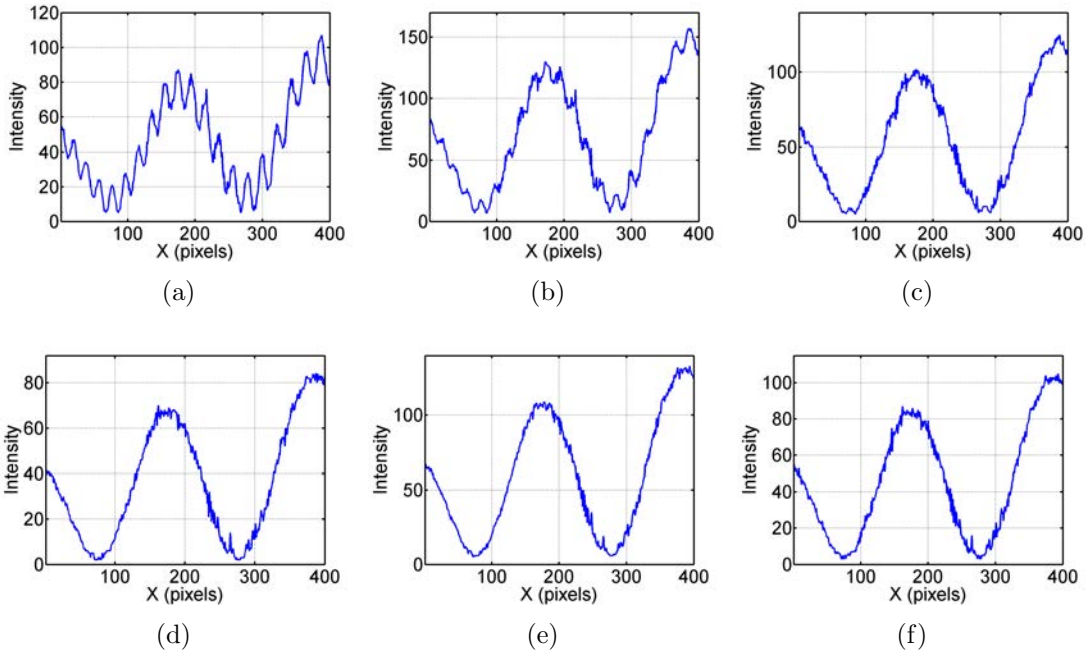

Figure 8.6 Cross sections of the fringe patterns shown in Fig. 8.5. (a) 2 kHz projection rate with 494 μs illumination time; (b) 1 kHz projection rate with 994 μs illumination time; (c) 500 Hz projection rate with 1994 μs illumination time; (d) 2 kHz projection rate with 200μs illumination time; (e) 1 kHz projection rate with 300μs illumination time; (f) 500 Hz projection rate with 800μs illumination time.

8.4.4 Phase Measurement Error Analysis

In order to test the performance of the DLP LightCommander projector, we carried out experiments to measure and analyze the phase error. A flat white board was used in this experiment. To obtain phase error, we first projected sinusoidal patterns one by one to ensure that there are no coupling issues, from which the reference phase was extracted. By comparing with the reference phase, we can obtain the phase error of the binary patterns under different conditions (Wang and Zhang, 2012a). Figure 8.7(a)-8.7(c) show the cross sections of the phase errors under 2 kHz, 1 kHz, and 500 Hz respectively with the maximum illumination time. And the standard error are respectively 0.176 rad, 0.067 rad, and 0.026 rad. Since the measured object is a flat board, the standard error represents the measurement accuracy. Figure 8.7(d)-8.7(f) show the corresponding

results with a shorter illumination time, while the standard error are 0.018 rad, 0.019 rad, and 0.016 rad. We find that if the maximum illumination times are used, the phase error is large when the projection speeds are higher than 1 kHz. When the projection speeds are set to a comparably lower value (less than 500 Hz), the phase error decreases considerably. This is understandable since the transient response of the DMD has relatively less impact overall. In contrast, if a shorter illumination time is used, the phase error for all projection speeds is much smaller, with the higher speeds having larger reduction. For the 2 kHz projection speed, the phase error decrease by nearly 90% to a rms value of 0.018 rad, which is negligible even for high quality measurement.

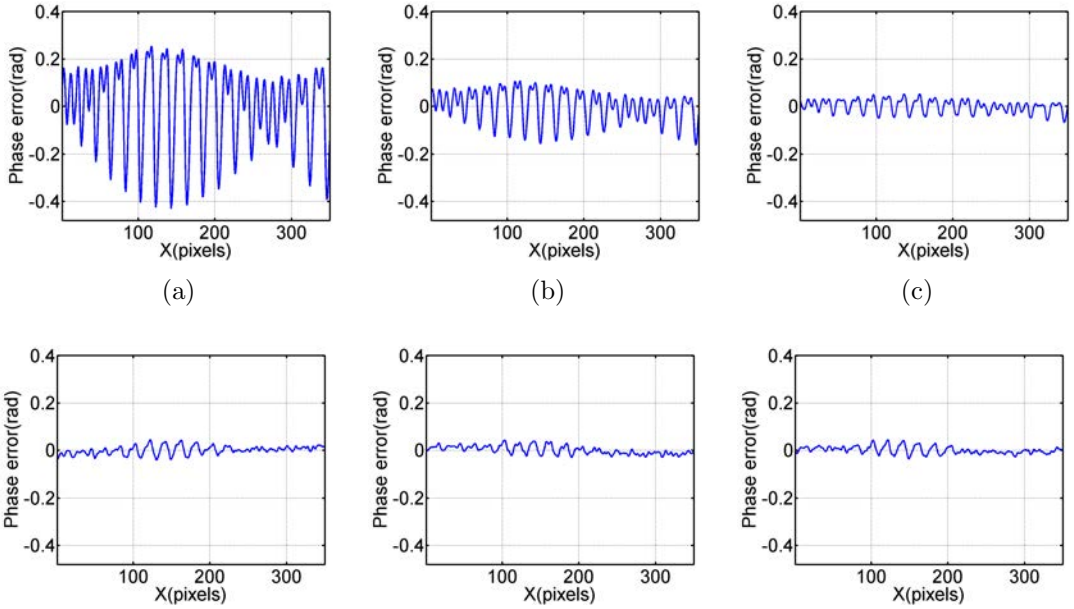

Figure 8.7 Phase measurement error under different different conditions. These figures show the same cross sections of the corresponding phase error maps. (a) 2 kHz projection rate with 494 μs illumination time; (b) 1 kHz projection rate with 994 μs illumination time; (c) 500 Hz projection rate with 1994 μs illumination time; (d) 2 kHz projection rate with 200μs illumination time; (e) 1 kHz projection rate with 300μs illumination time; (f) 500 Hz projection rate with 800μs illumination time.

8.4.5 3D Shape Measurement for Static Object

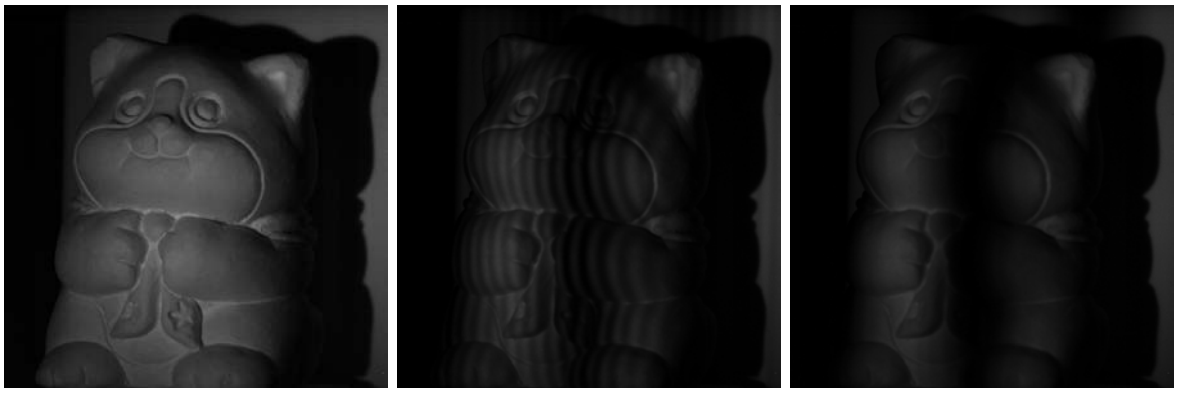

(a) (b) (c)

Figure 8.8 Experimental results of a static object. (a) Photograph of the object; (b) Captured fringe pattern with lower frequency for 2000 FP; (c) Captured fringe pattern with lower frequency for 2000 SP.

To further verify the performance of the DLP LightCommander projector under different conditions, we carried out more experiments to measure the 3D shape of a static object. In this research, we adopted the same reference-plane-based calibration method as described in Ref. (Xu et al., 2011). A 3D sculpture of a cat was measured and reconstructed under the same conditions experimented previously. Figure 8.8(a) shows the photograph of the 3D sculpture. Figure 8.8(b) shows a severely coupled pattern of 2 kHz with the maximum illumination time, while the corresponding pattern of 2 kHz with a shorter illumination time is shown in Fig. 8.8(c). By visually observing these patterns, we can clearly see the improvement brought about by reducing the illumination time.

Figure 8.9(a)-8.9(c) respectively show the recovered 3D results of 2 kHz, 1 kHz, and 500 Hz with the maximum illumination time, while Fig. 8.9(d)-8.9(f) show the corresponding 3D results with a shorter illumination time. Comparing the results among the figures in the first row where the projection illumination time is full, it can be found that the reconstructed surface becomes smoother when the projecting speed decreases. At approximately 500 Hz, the 3D result is already very good. Meanwhile, by comparing

the results in the first and the second row images, we can conclude that by using a shorter illumination time, the quality of the reconstructed 3D results are significantly improved for all different projection speeds, with higher speeds having more improvement. This is consistent with our previous experimental findings. Therefore, we recommend that to measure static objects with high-quality, it is better to either lower the projection speed to 500 Hz or less and increase the illumination time, or shorten the illumination time and increase the projector speed.

8.4.6 Superfast 3D Shape Measurement

Since our ultimate goal is to mitigate the coupling effect of the DLP LightCommander projector for high-speed measurement, we conducted an experiment to capture and recover the motion of a pendular ball. In this experiment, a ball is suspended by a string and released from the same height each time to ensure the motions are almost identical under varying projection and capture conditions. The important difference to keep in mind between this and the previous experiment is that the motion itself could also contribute to the phase measurement error. Figure 8.10(a) shows the photograph of the pendular ball. Figure 8.10(b) shows a severely coupled pattern of 2 kHz with the maximum illumination time, while the corresponding pattern of 2 kHz with a shorter illumination time is shown in Fig. 8.10(c).

Figure 8.11 as well as the associated medias (Media 1, Media 2, and Media 3) show the 3D recovered results under different conditions. Figure 8.11(a)-8.11(c) shows the results of 2 kHz, 1kHz and 500 Hz with the maximum illumination time, while Fig. 8.11(d)-8.11(f) show the corresponding results with a shorter illumination time, as used before. Comparing all the results in Fig. 8.11, we can clearly see that the best result is from 2 kHz with a shorter illumination time. All the other results have evident stripe noise on the recovered 3D surfaces. This finding is different from that of measuring a static object because the lower projection speed (less than 2 kHz) could have motion induced artifacts,

as evident from these experimental results. 1 kHz capturing speed has some artifacts caused by motion, while the 500 Hz capturing speed has more motion artifacts, albeit the error caused by motion and the error caused by coupling appear to be similar. The similarity between these two artifacts actually made the coupling problem more difficult to be identified and solved since the motion-induced artifact is well known and easy to be responsible for this types of error. Therefore, we recommend that to capture high-speed motion, a good solution is to use a shorter illumination time with a high speed instead of lowering the projection speed due the motion artifacts.

8.5 Conclusion

This paper has presented the limitation of the DLP LightCommander projector when operated under high speeds. It specifically looked into the transient effect of the DMD response on phase measurement quality when binary structured patterns are used. We find that the coupling effect influences the measurements significantly especially when the projection speed is higher than 1 kHz. By lowering the projection speed, considerably better results can be obtained for static or slow-speed objects measurement. In order to capture highly dynamic events or objects, a high projection speed is required, coupled with a shorter illumination time for the projector. Experimental results of both static and high-speed moving objects were presented and verified the success of the proposed method.

It is important to note that not only the DLP LightCommander projector has the issues we discovered, our research also found that the newer versions high-speed DLP projectors (i.e., DLP LightCrafter 3000 and DLP LightCrafter 4500) also have the same problems, albeit at different significance levels. We verified that the method presented in this paper could also be applied to those projectors to solve such similar issues.

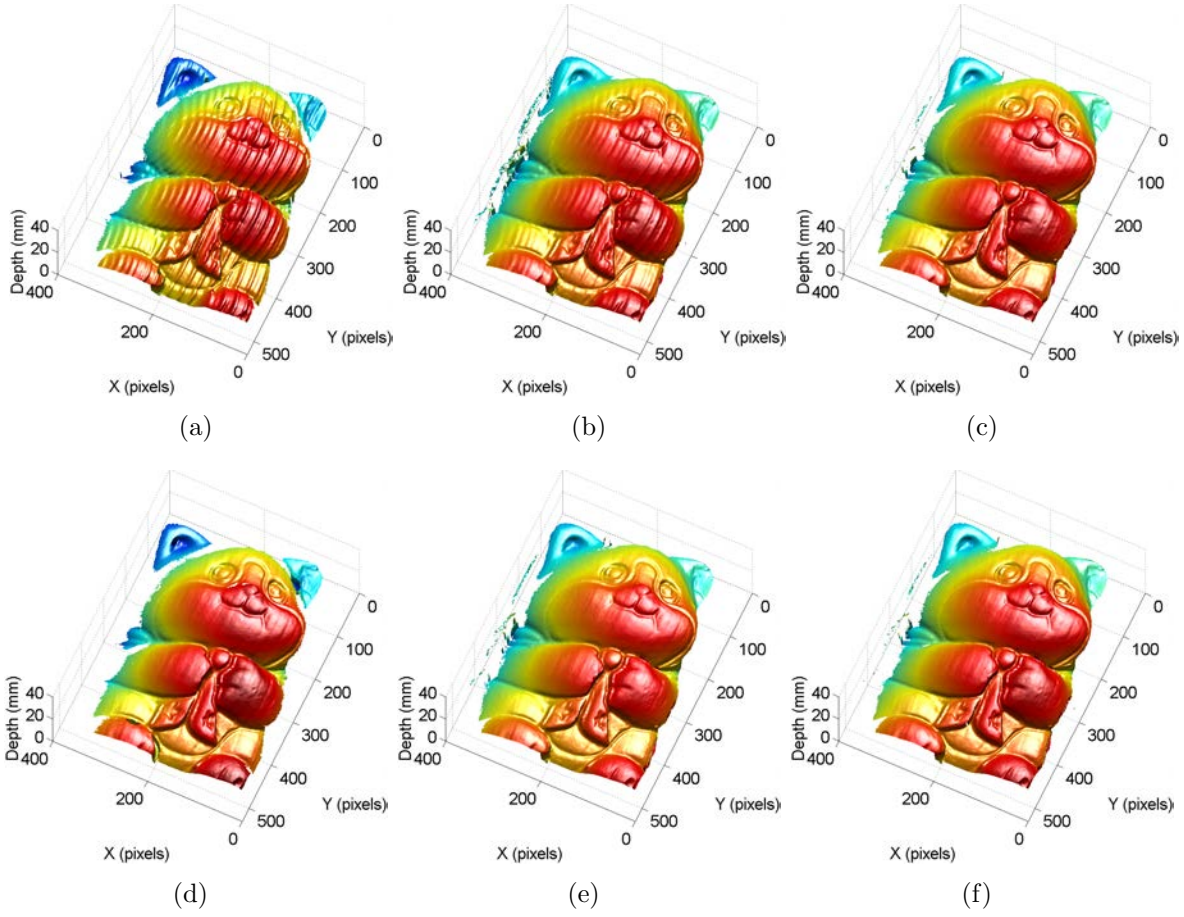

Figure 8.9 3D shape measurement results of the sculpture shown in Fig.8.10 under different conditions. (a) 2 kHz projection rate with 494 μs illumination time; (b) 1 kHz projection rate with 994 μs illumination time; (c) 500 Hz projection rate with 1994 μs illumination time; (d) 2 kHz projection rate with 200μs illumination time; (e) 1 kHz projection rate with 300μs illumination time; (f) 500 Hz projection rate with 800μs illumination time.

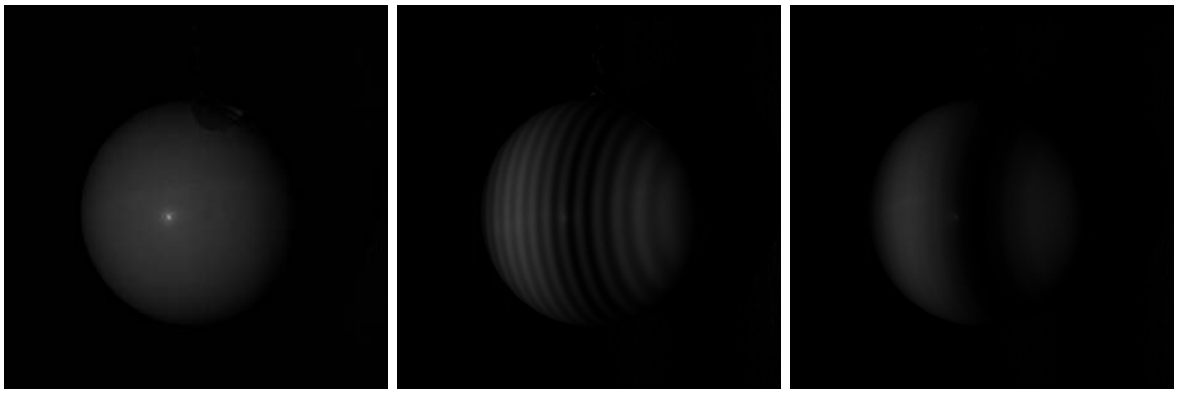

(a) (b) (c)

Figure 8.10 Experimental results of a pendular ball. (a) Photograph of the ball; (b) Captured fringe pattern with lower frequency for 2000 FP; (c) Captured fringe pattern with lower frequency for 2000 SP.

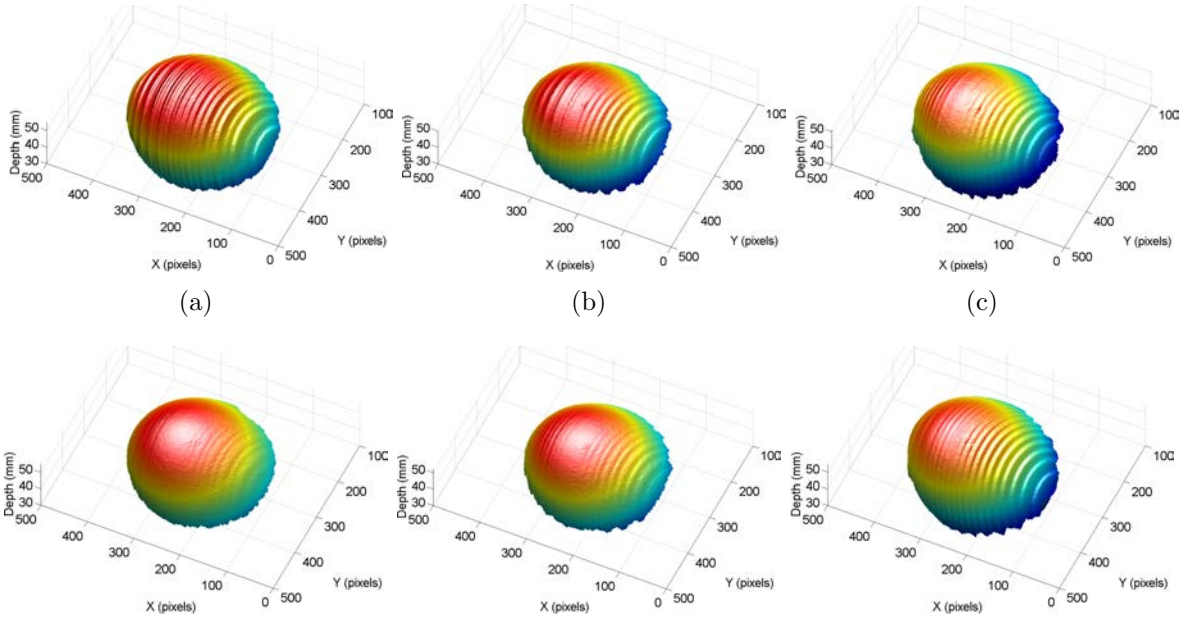

(a) (b) (c)

(d) (e) (f)

Figure 8.11 3D shape measurement results of a moving pendular ball under different conditions. (a) 2 kHz projection rate with 494 μs illumination time; (b) 1 kHz projection rate with 994 μs illumination time; (c) 500 Hz projection rate with 1994 μs illumination time; (d) 2 kHz projection rate with 200μs illumination time; (e) 1 kHz projection rate with 300μs illumination time; (f) 500 Hz projection rate with 800μs illumination time. (Media 1 for (a) and (d), Media 2 for (b) and (e), Media 3 for (c) and (f)).

CHAPTER 9. 3D ABSOLUTE SHAPE MEASUREMENT OF LIVE RABBIT HEARTS WITH A SUPERFAST TWO-FREQUENCY PHASE-SHIFTING TECHNIQUE

A paper published in the Journal of Optics Express in September 2012.[1]

Yajun Wang[2,7], Jacob I. Laughner[3,5], Igor R. Efimov[4,5], and Song Zhang[6,7]

9.1 Abstract

This paper presents a two-frequency binary phase-shifting technique to measure three-dimensional (3D) absolute shape of beating rabbit hearts. Due to the low contrast of the cardiac surface, the projector and the camera must remain focused, which poses challenges for any existing binary method where the measurement accuracy is low. To conquer this challenge, this paper proposes to utilize the optimal pulse width modulation (OPWM) technique to generate high-frequency fringe patterns, and the error-diffusion dithering technique to produce low-frequency fringe patterns. Furthermore, this paper will show that fringe patterns produced with blue light provide the best quality measure-

[1]This paper was published in the Journal of Optics Express and is made available as an electronic reprint with the permission of OSA. The paper can be found at the following URL on the OSA website: http://www.opticsinfobase.org/oe/abstract.cfm?URI=oe-21-5-5822. Systematic or multiple reproduction of distribution to multiple locations via electronic or other means is prohibited and is subject to penalties under law.

[2]Primary researcher and author.

[3]Graduate student collaborator.

[4]Professor and Jacob I. Laughner's advisor.

[5]Department of Biomedical Engineering, Washington University, Saint Louis.

[6]Assistant professor and Yajun Wang's advisor.

[7]Department of Mechanical Engineering, Iowa State University.

ments compared to fringe patterns generated with red or green light; and the minimum data acquisition speed for high quality measurements is around 800 Hz for a rabbit heart beating at 180 beats per minute.

9.2 Introduction

Visualizing 3D geometry of the heart with the corresponding optical cardiac mapping of the electrical activities with voltage- and/or calcium-sensitive dyes is a very powerful tool for studying complex rhythms and arrhythmias. Recent studies demonstrated that by immobilizing the heart to capture one panoramic 3D model, and then map the time-varying fluorescence images onto this static 3D model is very useful (Lou et al., 2008). However, it is impossible to know the mechanical function if the heart is immobilized. Therefore, accurate measure of the 3D dynamic surface geometry of the beating heart is vital to improving our understanding of mechanics in health and disease. Because the optical properties of heart surfaces (i.e., partially shiny and highly absorbing), it is quite challenging for an optical method to perform such measurement with minimum error. The measurement becomes even more challenging when the heart is rapidly beating (e.g., around 180 beats/min, or 3 Hz, for an explanted rabbit heart) since a very high-speed 3D shape measurement system is required. This paper presents a novel 3D shape measurement technique to conquer these challenges.

Optical methods have been extensively adopted in measuring various objects (e.g., human faces (Zhang, 2010b), honeybee (Zhang et al., 2008)). Phase-shifting-based fringe analysis techniques have the advantage of measuring challenging surfaces (e.g. low surface contrast) while achieving high spatial and temporal resolution. Digital fringe projection (DFP) methods have been extensively adopted due to the flexibility of system development and high achievable speed (Zhang, 2010b). However, it is extremely difficult for conventional DFP techniques to achieve faster than 120 Hz which is the maximum

refresh rate of a digital video projector. Therefore, it is difficult for such techniques to precisely measure beating hearts, like that of the rabbit.

Binary defocusing has enabled tens of kHz rate 3D shape measurement speed because it only requires 1-bit structured patterns rather than 8-bit grayscale patterns (Zhang et al., 2010). However, measurement error is large if the projector is not properly defocused (Xu et al., 2011). Unfortunately, due to the low contrast of the heart surface, the projector has to be nearly focused to achieve the highest possible fringe contrast. Thus, measurement accuracy and determination of mechanical parameters like surface strain becomes compromised. Techniques based on 1-D pulse width modulation (PWM) (Wang and Zhang, 2010; Ajubi et al., 2010) have been proposed to improve the binary defocusing technique. They are proved to be successful when the fringe stripes are narrow, yet fail when fringe stripes are wide. The PWM technique has been successfully applied to measure beating rabbit hearts, but requires a gray-coding method and employs a computational framework to recover absolute 3D shape (Laughner et al., 2002). As a result of the gray-coding method, more than six (ten in our previous study) images are required to recover one 3D frame. For high-speed applications, it is desirable to use fewer number of fringe patterns to reduce motion induced artifacts.

Dithering techniques have been successfully used in printing technology to represent grayscale images with binary structured images (Schuchman, 1964). Recently, we have introduced the ordered-Bayer dithering technique to the 3D shape measurement field to generate high quality fringe patterns even for wide fringe stripes (Wang and Zhang, 2012b). We found that the dithering technique cannot substantially improve measurement quality when the fringe stripe is narrow, yet it provides the potential to generate high-quality sinusoidal fringe patterns with low spatial frequency using the binary defocusing method.

This paper proposes to combine the PWM technique with the dithering technique to obtain absolute phase with only six fringe patterns. Specifically, we utilize the optimal

pulse width modulation (OPWM) technique (Wang and Zhang, 2010) to generate three high-frequency sinusoidal fringe patterns, and the dithering technique to produce three low-frequency fringe sinusoidal fringe patterns. By adopting a two-frequency phase-shifting technique, the absolute phase is determined. Instead of using the ordered-Bayer dithering technique, a better technique called error-diffusion dithering is introduced to generate better low-frequency fringe patterns. Since measuring beating rabbit hearts is the ultimate goal of this study, this paper also addresses some practical considerations for measuring the cardiac deformation. First, we investigation the effect of wavelength of the projected fringe patterns on measurement quality. Optical properties of cardiac tissue (i.e., absorption, reflectance, and transmission) play an important role in measurement error. Experimental data will be presented to show the differences for beating hearts and formalin-fixed hearts. Additionally, we investigate the the minimum measurement speed to minimize both data size and motion induced artifacts.

Section 9.3 explains the principles of proposed techniques. Section 9.4 shows some experimental results, and Section 9.5 summarizes the paper.

9.3 Principle

9.3.1 Two-Frequency Phase-Shifting Technique for Absolute Phase Retrieval

Phase-shifting methods have been extensively adopted in optical metrology because of their measurement speed and accuracy. Over the years, a variety of phase-shifting algorithms have been developed, that include three-step, four-step, and least-square algorithms (Malacara, 2007). For high-speed 3-D shape measurement, a three-step phase-shifting algorithm with a phase shift of $2\pi/3$ is commonly used. The three fringe images

can be described as:

$$I_1(x,y) = I'(x,y) + I''(x,y)\cos(\phi - 2\pi/3), \tag{9.1}$$

$$I_2(x,y) = I'(x,y) + I''(x,y)\cos(\phi), \tag{9.2}$$

$$I_3(x,y) = I'(x,y) + I''(x,y)\cos(\phi + 2\pi/3). \tag{9.3}$$

Where $I'(x,y)$ is the average intensity, $I''(x,y)$ the intensity modulation, and $\phi(x,y)$ the phase to be solved for. Simultaneously solving Eq. (9.1)-(9.3), the phase can be obtained

$$\phi(x,y) = \tan^{-1}\left[\sqrt{3}(I_1 - I_3)/(2I_2 - I_1 - I_3)\right]. \tag{9.4}$$

This equation provides the wrapped phase with 2π discontinuities. A spatial or temporal phase unwrapping algorithm can be applied to obtain continuous phase.

We utilized a two-frequency temporal phase-unwrapping algorithm to unwrap the phase. Essentially, two wrapped phase maps, low frequency phase ϕ^l and high-frequency $\phi^h(x,y)$. $\phi^l(x,y)$ is obtained from wide fringe patterns with a single fringe covering the whole measuring range, such that no phase unwrapping is required. By referring to $\phi^l(x,y)$ point by point, $\phi^h(x,y)$ is unwrapped to obtain a continuous phase map, $\Phi(x,y)$. Because 3D information is carried on by the phase, 3D shape can be reconstructed from the unwrapped phase $\Phi(x,y)$ using a phase-to-height conversion algorithm (Xu et al., 2011).

9.3.2 Optimal Pulse Width Modulation (OPWM) Technique to Modulate High-Frequency Patterns

The recently proposed binary defocusing technique can greatly improve the measurement speed of DFP methods. However, when the projector is nearly focused, serious phase errors will arise due to the effects of high-order harmonics (Wang and Zhang, 2012a). Therefore, in this paper, OPWM is adopted to generate high-frequency patterns. This technique selectively eliminates undesired frequency components by inserting

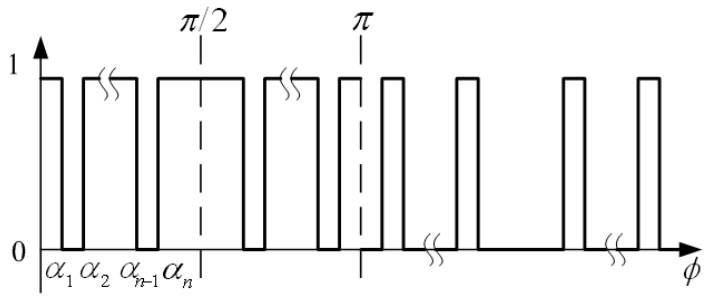

Figure 9.1 Quarter-wave symmetric OPWM waveform.

different types of notches in a conventional binary square wave. With slight projector defocusing, ideal sinusoidal fringe patterns can then be generated.

Figure 9.1 illustrates a general quarter-wave symmetric OPWM pattern. The square wave is chopped n times per-half cycle. For a periodic waveform with a period of 2π, because it is an odd function, only the sine terms are left with the coefficients being described as:

$$b_k = \frac{4}{\pi} \int_{\theta=0}^{\pi/2} f(\theta) \sin(k\theta) d\theta. \tag{9.5}$$

The n chops in the waveform provide n degrees of freedom to eliminate $n-1$ selected harmonics while keeping the fundamental frequency component within a certain magnitude. Due to the ability to eliminate undesired high-order harmonics, OPWM waveform could become sinusoidal after applying a small low-pass filter, which is similar to a small degree of defocusing. Our previous research has shown the success of OPWM technique (Wang and Zhang, 2012a).

9.3.3 Error-Diffusion-Based Dithering Technique to Modulate Low-Frequency Patterns

Due to the high-order harmonics, it is very difficult to achieve low-frequency patterns for the binary defocusing technique. We have recently introduced the dithering technique to generate high-quality fringe patterns for wide fringe stripes (Wang and Zhang,

2012b). Binary dithering is one of the techniques extensively used to render color or grayscale images with only 1-bit images. It has been used to process both digital audio and video data. There are numerous dithering techniques developed including random dithering (Purgathofer et al., 1994), ordered dithering (Bayer, 1973) and error-diffusion dithering (Kite et al., 2000). Among these dithering techniques, the sophisticated error-diffusion dithering techniques have been most extensively adopted because they can represent the original image or signal with higher fidelity compared to simpler dithering algorithms. In this method, the pixels are quantized in a specific order, and the error of quantization for the current pixel is propagated forward to local unprocessed pixels. By this means, the local average of the converted image is close to the original one.

The process of modifying an input pixel by prior quantization errors can be mathematically described as,

$$\tilde{f}(i,j) = f(i,j) + \sum_{k,l \in S} h(k,l)e(i-k, j-l). \tag{9.6}$$

Here, $f(i,j)$ is the original image, and error $e(i,j)$ is the difference between the quantized image pixel and the diffused image pixel including the prior processed pixel influences. The error $e(i,j)$ of quantizing the current pixel is further diffused to its neighboring pixels by means of a two-dimensional weighting function $h(i,j)$, known as the diffusion kernel. There are numerous error-diffusion dithering algorithms differing on the diffusion kernel selection. In this paper, we use the kernel proposed by Stucki (Stucki, 1981),

$$h = \begin{bmatrix} - & - & * & 8/42 & 4/42 \\ 2/42 & 4/42 & 8/42 & 4/42 & 2/42 \\ 1/42 & 2/42 & 4/42 & 2/42 & 1/42 \end{bmatrix}. \tag{9.7}$$

Here, $-$ represents the previously processed pixels, and $*$ represents the pixel in processing. It should be noted that the kernel coefficients sum to one, and thus the local average value of the quantized image will be equal to the local average of the original one.

In this paper, we introduce this dithering technique to convert 8-bit sinusoidal fringe pattern into 1-bit binary patterns. By combining with the defocusing technique, high-quality sinusoidal patterns with wide fringe stripes can be achieved. Figure 9.2 illustrates a simulation example with generating a sinusoidal fringe pattern with a fringe pitch (number of pixels per fringe period) of 150 pixel. The original sinusoidal fringe pattern is dithered with the ordered-Bayer dithering technique (Wang and Zhang, 2012b) and the error-diffusion dithering technique with the kernel described in Eq. (9.7). This simulation results show that the resultant image (Fig. 9.2(d)) from the error-diffusion dithering appears better than that (Fig. 9.2(a)) from the ordered-Bayer dithering before defocusing (or blurring). Three phase-shifted fringe patterns are generated for each dithering technique, and these patterns are smoothed by a small Gaussian filter (9×9 pixels in dimension with a standard deviation of 3 pixels) to emulate the effect introduced by a small amount of defocusing. After smoothing, the cross sections of these patterns are shown in Fig. 9.2(b) and Fig. 9.2(e). These smoothed patterns are further processed to obtain the phase maps using a three-step phase-shifting algorithm. The phase errors can be determined by comparing with the ideal phase obtained from the ideal sinusoidal fringe patterns. Figure 9.2(c) and Fig. 9.2(f) show the cross sections of the phase errors. It clearly shows that the error-diffusion dithering method is significantly better than the ordered-Bayer dithering method. Therefore, instead of using the ordered-Bayer dithering technique, we utilize the error-diffusion dithering technique to generate the low-frequency sinusoidal fringe patterns.

9.4 Experiments

9.4.1 Experimental System Setup

Figure 9.3 shows a photograph of the system we developed. It is composed of a digital-light-processing (DLP) projector (DLP LightCrafter, Texas Instruments, TX), a

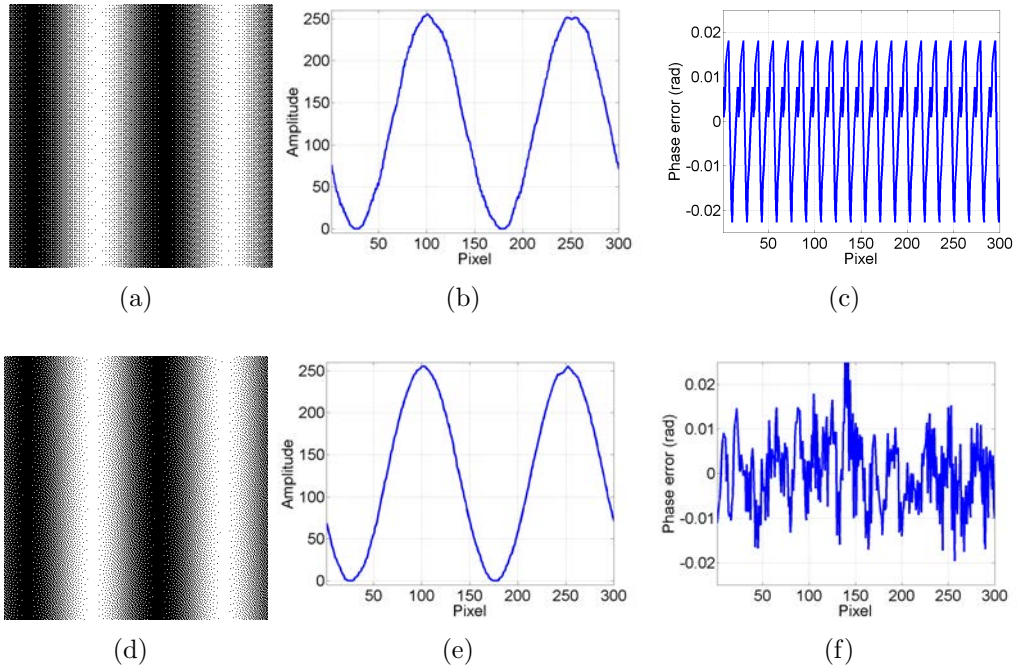

(a) (b) (c)

(d) (e) (f)

Figure 9.2 Comparison of Bayer dithering and error-diffusion dithering. (a) Bayer-dithering pattern; (b) Cross section of (a) after Gaussian smoothing; (c) Phase error (rms error of 0.012 rad); (d) Error-diffusion dithered pattern; (e) Cross section of (c) after Gaussian smoothing; (f) Phase error (rms 0.008 rad).

high-speed CMOS camera (Phantom V9.1, Vision Research, NJ). The RGB LEDs used in this projector are (R: OSRAM LEAS2W 617 nm; G: OSRAM LCG H9RN 529 nm; B: OSRAM LEBS2W 464 nm). The camera is triggered by an external electronic circuit that senses timing signal of the DLP projector. For all experiments conducted in this research, the camera was set to capture images with a resolution of 576 $\times$ 576, and both the the projector and the camera were focused and remained fixed. The camera lens aperture was adjusted to ensure that the brightest possible fringe patterns were captured.

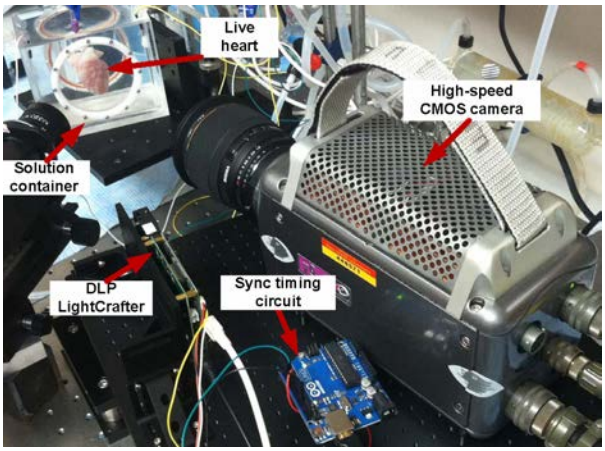

Figure 9.3 Photograph of live heart measurement system.

9.4.2 Live and Fixed Rabbit Heart Preparation

We imaged both formalin-fixed (10% formalin, n = 1) and *Langendorff-perfused* hearts (n = 2) isolated from New Zealand white rabbits. All studies were approved by the Institutional Animal Care and Use Committee of Washington University in St. Louis. The formalin-fixed heart was used for experimental validation of a stationary heart as described below. *Langendorff-perfused* hearts, conversely, were used to verify motion-induced artifacts. While this ex vivo, *Langendorff-perfused* model does not completely capture in vivo cardiac mechanics due to unloading during removal, it nevertheless provides a means to validate our system on a dynamically deforming heart. Each heart was removed via a mid-sternal thoracotamy and immediately perfused with oxygenated (95% O2, 5% CO_2) Tyrode's solution at a constant pressure of 60 ± 5 mmHg and temperature of 37 °C. Insulin (200 mg/dL) was also added to the perfusate to improve glucose utilization by the heart. Once cannulated, hearts were placed in a custom superfusion chamber with an optical window for structured light imaging. Ag/AgCl electrodes were placed near the atrioventricular (AV) groove to record ECG measurements during experimentation.

The formalin-fixed and Langendorff-perfused hearts were isolated from two differ-

ent rabbits. Anatomical differences between the two hearts are minimal as a result of breeding control in our rabbit supplier.

9.4.3 Experimental Verification

9.4.3.1 Formalin-Fixed Rabbit Heart Measurement

Figure 9.4 illustrates the phase-shifting algorithms we adopted by measuring a formalin-fixed rabbit heart. Figures 9.4(a)-9.4(c) show three high-frequency phase-shifted fringe patterns that used the OPWM patterns. It is important to note that these patterns have very obvious binary structures, but we will show that high-quality 3D shape measurement can still be achieved due to the use of OPWM technique. Figures 9.4(e)-9.4(g) show three low-frequency fringe patterns that used the dithered patterns. Applying Eq. (9.4) to three phase-shifted fringe patterns, the wrapped phase of both frequencies can be obtained. Figure 9.4(d) shows the high-frequency wrapped phase map, which possesses 2π phase discontinuities. The low-frequency wrapped phase, as shown in Fig. 9.4(h), is continuous without 2π discontinuities. By referring to the phase map obtained from the low frequency patterns, the high-frequency wrapped phase can be unwrapped point by point. Figure 9.5(a) shows the unwrapped phase. In this research, we used the approximate phase-to-height conversion approach introduced in Reference (Xu et al., 2011) to calibrate the system. After calibration, the 3D shape can be recovered. Figure 9.5(b) shows the 3D shape measurement results of the heart surface.

Figure 9.6 shows a comparison of different projection wavelengths on the formalin-fixed heart with blue, green, and red lighting sources. The contrast of Fig. 9.6(a) is better than Fig. 9.6(b) and Fig. 9.6(c). Figures 9.6(d)-9.6(f) show the corresponding reconstructed 3D shapes of the fixed heart. There are slight differences among these measurement, but surface measurement quality is high regardless of the spectrum of light used.

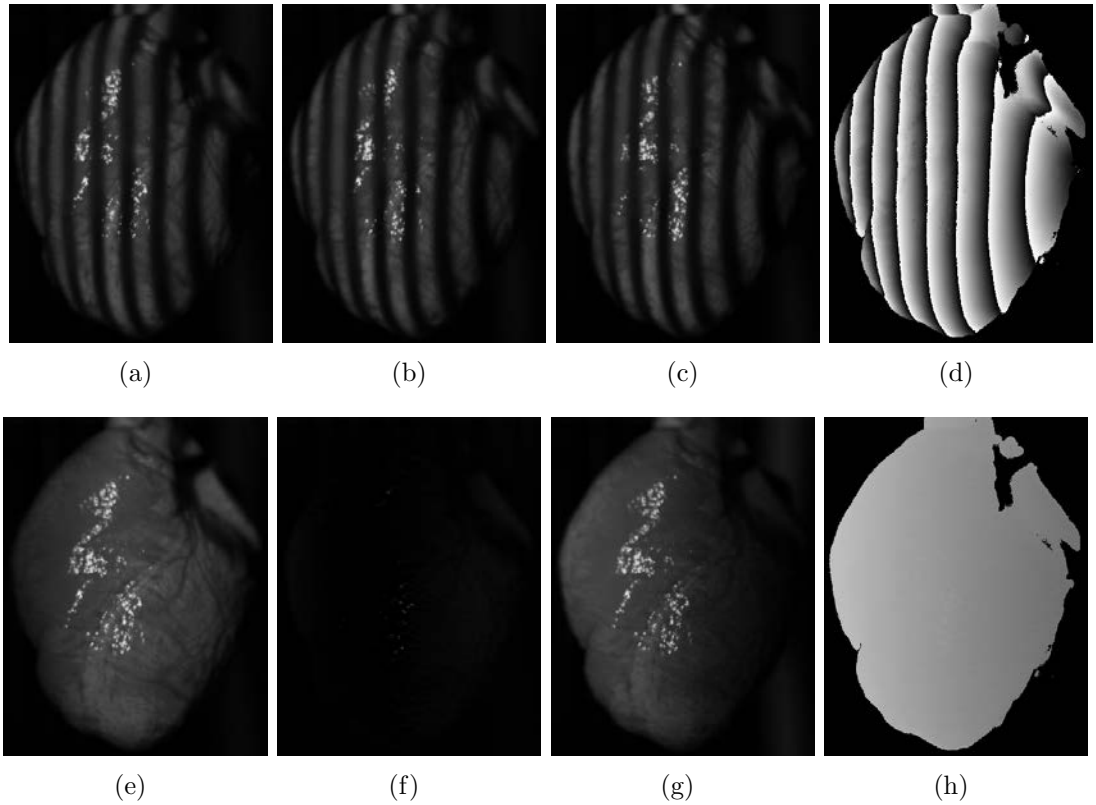

Figure 9.4 Wrapped phase maps for dead heart measurement. (a)-(c) High-frequency fringe patterns; (d) Wrapped phase map of high frequency patterns; (e)-(g) Low-frequency fringe patterns; (h) Wrapped phase map of low frequency pattern

9.4.3.2 Beating Rabbit Heart Measurement: Spectrum of Light Influence

As mentioned previously, we measured a beating rabbit heart with different projection wavelengths to investigate the combination of motion artifacts and light-tissue interaction on surface measurement quality. Figure 9.7 and the associated videos show the comparing results. Figures 9.7(a)- 9.7(c) respectively show the fringe patterns when the blue, green and red light was used. In comparison with fringe patterns captured for a fixed heart shown in Figs. 9.6(a)-9.6(c), the fringe contrast varies drastically for different wavelengths. Figures 9.7(d)- 9.7(f) show the corresponding reconstructed 3D results. Here, we used the projection speed of 2,000 Hz to ensure no motion induced artifacts. To fairly compare data recorded from red, green, and blue wavelengths, frames were

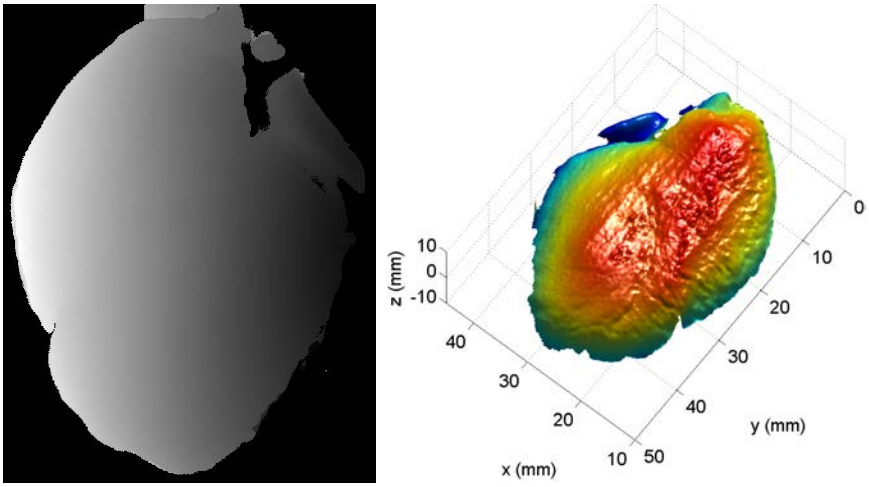

(a) (b)

Figure 9.5 Unwrapped phase map for dead heart measurement. (a) Unwrapped phase map; (b) 3D reconstructed shape of the heart surface

selected from the same specific phase in the cardiac cycle. Unlike the fixed heart, the beating rabbit heart measurement results vary drastically the projector light wavelength, with blue light giving the best results and red light giving the worst results. Specifically, surface reconstructions from blue light appear to have smoother surface geometry and fewer fringe artifacts. We believe one possible cause for this is the optical properties of rabbit cardiac tissue for blue light relative to green or red. Blue light with a wavelength of 464 nm will have low penetration into cardiac tissue and high scattering compared to green or red light. As a result, measurement error from red and green light could be a result of light contributions from mid-myocardial light scattering and not simply light reflecting from the epicardial surface (Bowen, 1949). Fixation of cardiac tissues increasing scattering and may explain the wavelength independence we observed in our formalin fixed heart measurements. Based on these observations, only blue light was utilized for our other beating heart experiments.

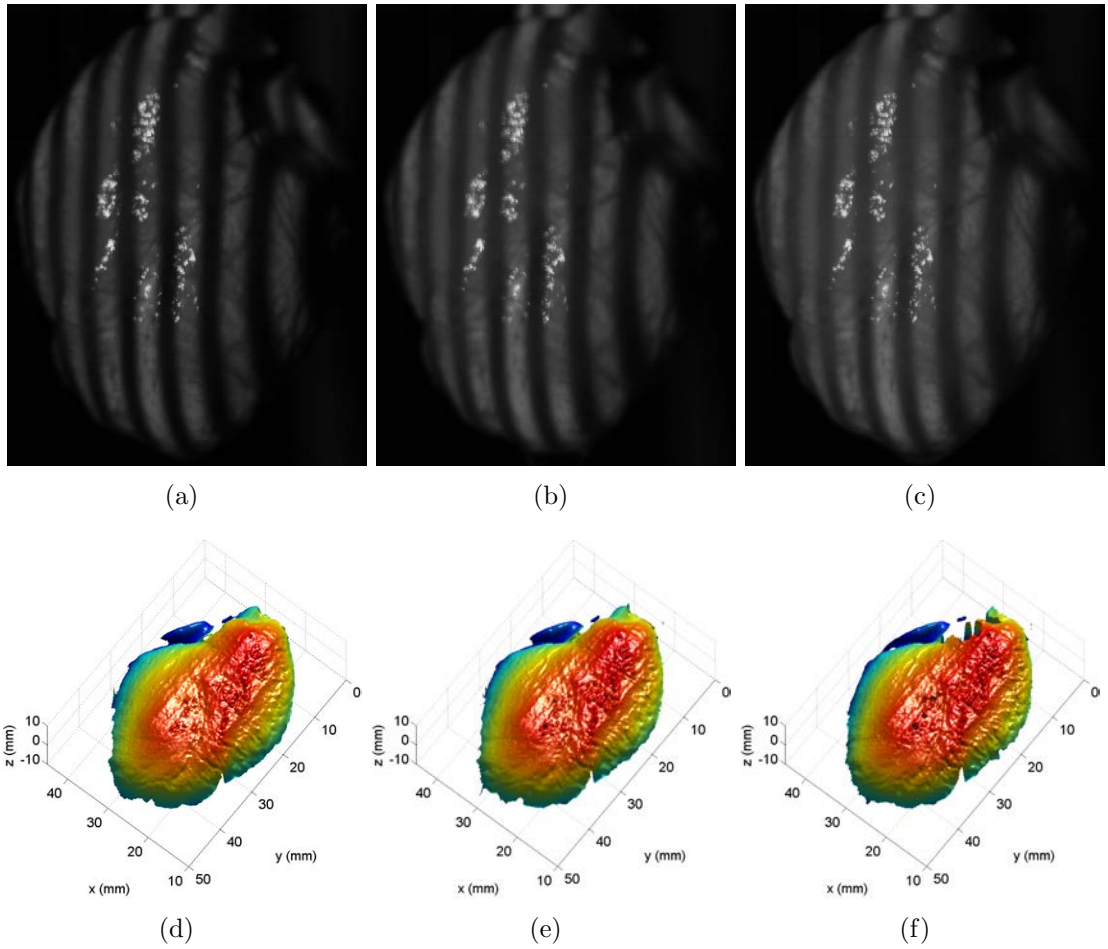

Figure 9.6 Comparison of different spectrum for fixed heart measurements. (a) One fringe pattern using blue light; (b) One fringe pattern using green light; (c) One fringe pattern using red light; (d) 3D result using blue light; (e) 3D result using green light; (f) 3D result using red light.

9.4.3.3 Live Rabbit Heart Measurement: Measurement Speed Influence

Typically, an explanted rabbit heart beats at approximately 180 beats/min. The 3D shape measurement technique discussed requires the capture of a sequence of fringe patterns to reconstruct one 3D frame. The fundamental assumption during acquisition is that the heart surface is static during the projection and acquisition of the fringe patterns. Yet, for a beating heart, the surface is constantly deforming. Therefore, in order to properly capture such a dynamically deforming object, the sampling rate must

be high enough such that the motion-induced artifacts can be negligible. To determine the minimum frame rate to *properly* capture the heart surface without obvious motion artifacts, we measured the heart at frame rates of 200, 300, 400, 500, 800 and 1000 Hz. Figure 9.8 and the associated video (Media 3) show the 3D reconstructed results with these speeds when the heart surface displays greatest deformation. Figures 9.8(a) and 9.8(b) show the results with large bumpy striping artifacts, which were induced by motion. As a comparison, when the capturing speed increases to above 800 Hz, the results, such as those shown in Fig. 9.8(e)- 9.8(f), become rather smooth. Based on these results, we determine that in order to properly capture a beating rabbit heart with an ex vivo intrinsic rate of 180 beats/min, the minimum capturing speed required is approximately 800 Hz when a two-frequency phase-shifting technique is adopted.

It important to note that, to our knowledge, there was no existing "better" technology that could measure the dynamic geometric surface motion of the beating rabbit heart, and thus there was no quantitative measure for these comparisons besides qualitative measure.

9.5 Conclusion

This paper presents a two-wavelength phase-shifting-based system to measure rabbit hearts. Our system requires binary structured patterns and can achieve up to 4,000 Hz 3D shape measurement speed. Due to the low contrast of cardiac tissue, the projector and the camera must remain focused. An OPWM technique was used to generate high-frequency fringe patterns, and a dithering technique was employed to generate low frequency fringe patterns. Two-frequency phase-shifting was utilized in this system to achieve highest possible absolute 3D shape measurement speed. Our experiments found that for a formalin-fixed rabbit heart, the projection wavelength does not substantially influence the measurement quality; but for a beating rabbit heart, the projection

wavelength drastically alters the measurement quality with blue light generating the best results. Furthermore, we observed the motion induced artifacts for a beating rabbit heart are minimized at a minimum capture speed of 800 Hz when a two-frequency phase-shifting technique is adopted.

In summary, the major contributions of this paper are: (1) presented the first 3D shape measurement system that combines the OPWM method with the error-diffusion dithering method using the binary defocusing technique to achieve superfast absolute shape measurement; (2) introduced the error-diffusion based dithering technique, for the first time, to the field of 3D shape measurement; (3) successfully conquered the challenges of measuring live rabbit hearts; and (4) presented the guidelines for measuring live rabbit heart in terms of selecting spectrum of light and minimum capturing speed.

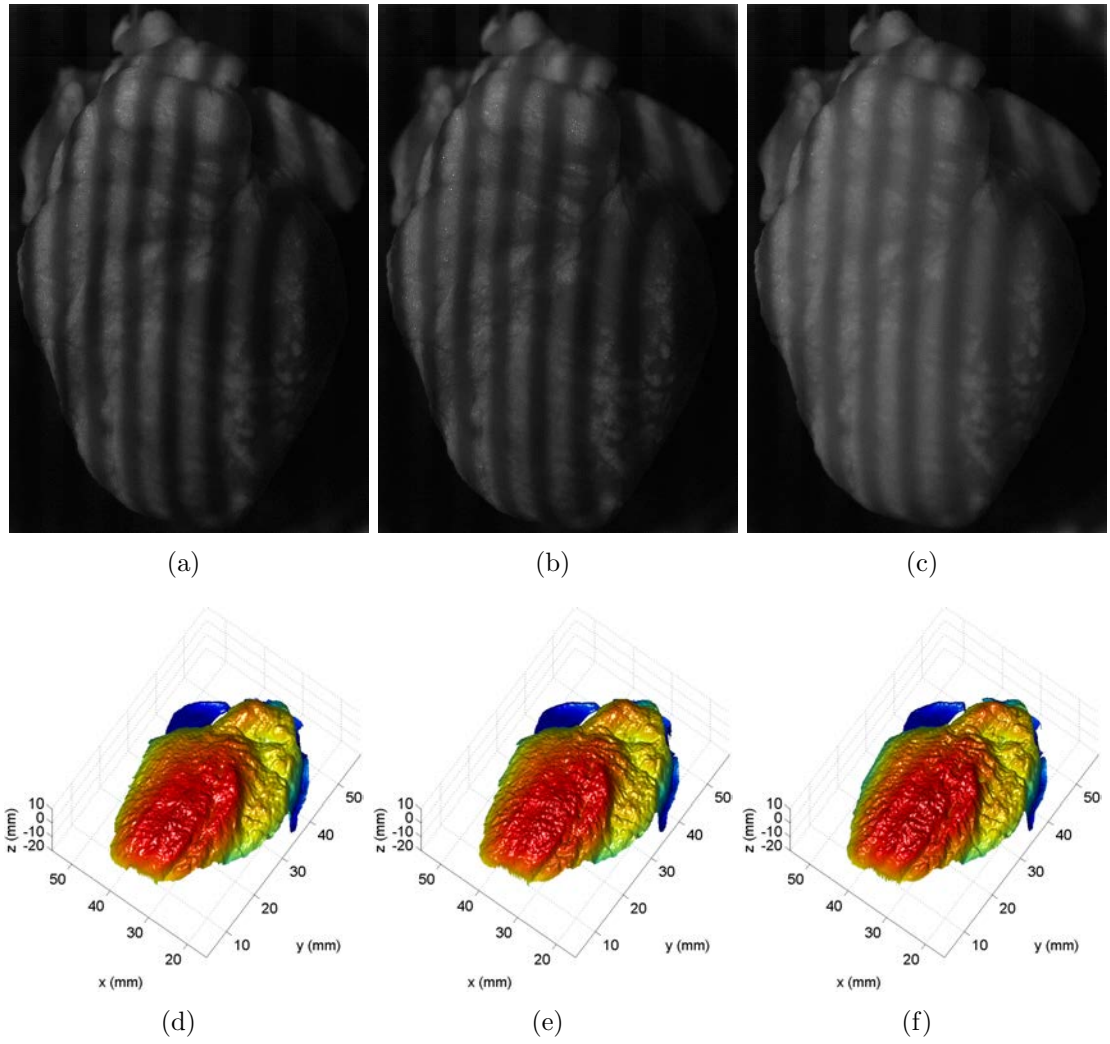

Figure 9.7 Comparison of different spectrum for beating heart measurements (Media 1 and Media 2). (a) One fringe pattern using blue light; (b) One fringe pattern using green light; (c) One fringe pattern using red light; (d) 3D result using blue light; (e) 3D result using green light; (f) 3D result using red light.

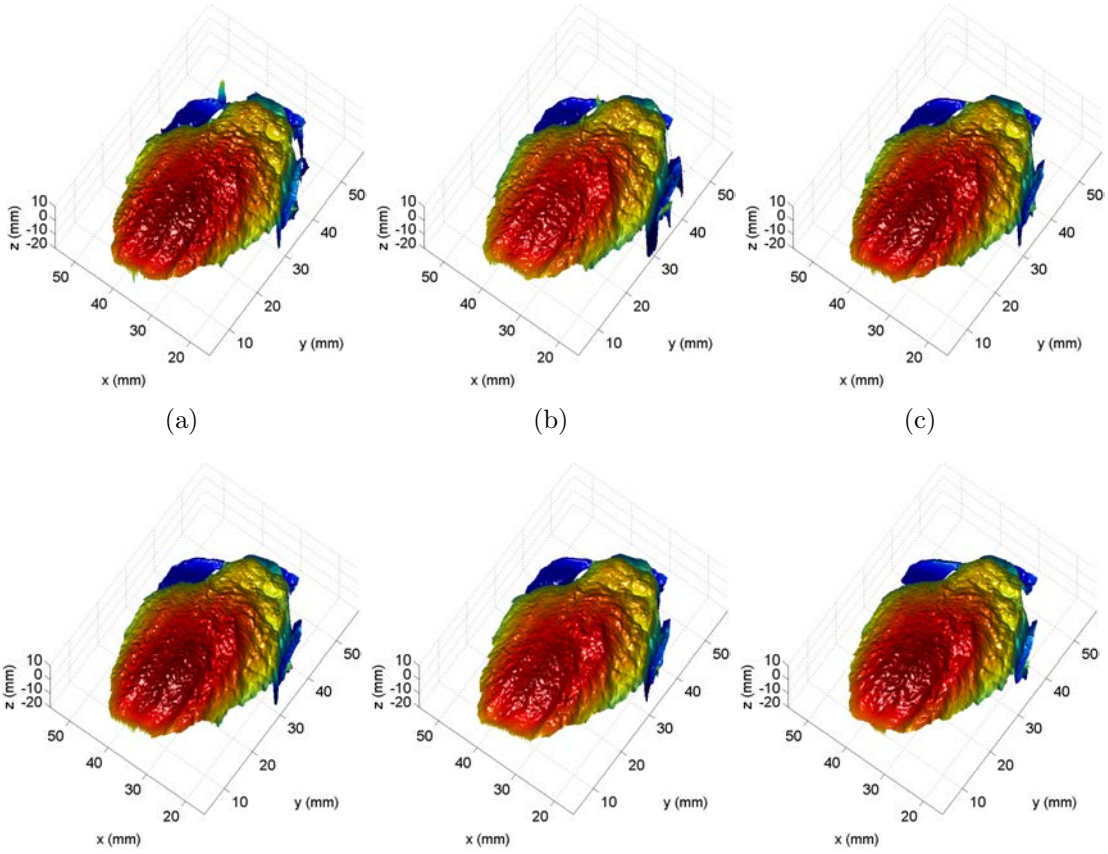

Figure 9.8 Comparison of different speed for beating heart measurements (Media 3). (a)-(f) respectively shows the 3D results with 200, 300, 400, 500, 800 and 1000 Hz.

CHAPTER 10. GENERAL CONCLUSION

In the previous chapters, this dissertation research on superfast 3D shape measurement with binary defocusing techniques and its applications has been presented. This chapter summarizes the major contributions of this dissertation research and discusses the potentials for extending this research.

10.1 Conclusions

To achieve superfast 3D shape measurement with high accuracy, this dissertation research has made the following major contributions:

1. **An optimal pulse width modulation (OPWM) method to improve the measurement quality of the squared binary defocusing technique.** This dissertation research developed the OPWM technique to overcome the major limitations of the squared binary method (SBM), influence of high-frequency harmonics, by selectively eliminating undesired high-frequency harmonics. Simulation and experimental results demonstrated that the OPWM technique can generate substantially higher quality sinusoidal fringe patterns than the SBM. Furthermore, the OPWM technique also allows the generation of high-quality sinusoidal fringe patterns with a wide range of fringe periods (i.e., 30-300 pixels) even when the projector is nearly focused.

2. **A multi-frequency phase-shifting (MFPS) algorithm to measure multiple rapidly moving objects.** It is challenging for the squared binary defocusing

technique to realize a multi-frequency phase-shifting (MFPS) algorithm because it is difficult to simultaneously generate high-quality sinusoidal fringe patterns with different periods under the same amount of defocusing. Since the developed OPWM method has the merits of generating a wide range of fringe patterns, an MFPS algorithm was developed utilizing the OPWM technique. A 556-Hz 3D system was successfully developed utilizing a three-frequency algorithm for simultaneously measuring multiple rapidly moving objects.

3. **The binary dithering techniques for 3D shape measurement.** The previously proposed binary defocusing technique and its variations (OPWM) have proven successful for high-quality three-dimensional (3D) shape measurement when fringe stripes are within a certain range, yet they fail to achieve high-quality measurement when fringe stripes are very wide (more than 300 pixels). To address this challenge, the binary dithering techniques were developed. Both simulation and experimental results showed the phase error is always less than 0.6% even when the fringe stripes are wide (about 600 pixels) and the projector is nearly focused. With the OPWM and dithering techniques, the binary defocusing method could reach very large depth measurement range with high measurement quality, detailed evaluation is presented in Appendix 10.2.

4. **An optimal fringe angle selection method for DFP technique.** The existing DFP systems mainly either use horizontal or vertical fringe patterns for three-dimensional (3D) shape measurement. However, our research found that these two fringe directions are usually not optimal where the phase change is the largest to a given depth variation. To address this, a novel and efficient method was developed to determine the optimal fringe angle by projecting a set of horizontal and vertical fringe patterns onto a step-height object and by further analyzing two resultant phase maps. Experimental results demonstrated the existence of the optimal angle

and the success of the proposed optimal angle determination method.

5. **A novel calibration method for the binary defocusing technique with high accuracy.** Due to the use of an out-of-focus projector, the existing calibration methods can not be directly employed to calibrate our system. To address this problem, a novel calibration method was developed that relates depth z with the phase pixel by pixel without the requirement of projector calibration. Because this method does not require estimation of the projector's parameters, it can be adopted for any phase measurement system including those employing out-of-focus projectors. By this means, very high accuracy depth measurement is achieved: for a depth measurement of 100 mm, the root-mean-squared (rms) error is approximately 70 μm.

6. **A method to solve the problems associated with the hardware limitations when conducting superfast 3D shape measurement.** The high refresh rate of the DMD has enabled superfast 3D shape measurement using the binary defocusing technique. However, under high-speed operations, the transient response of the DMD induces the coupling issue (i.e., two neighboring patterns blend together) that may cause substantial measurement error. Since this type of error is systematic, a novel method was developed by properly controlling the timing of the projector and the camera. This developed method is capable to reduce the error to a negligible level and thus successfully capture high-speed motions.

7. **A superfast 3D shape measurement platform with the application to the dynamic shape measurement of live rabbit hearts.** Taking advantage of the advanced binary defocusing techniques developed in this research, a superfast 3d shape measurement platform was developed. Furthermore, we applied this platform to measure the cardiac motion of live, beating rabbit hearts. We found that, to successfully capture the 3D geometric motion of the live rabbit hearts, the minimum

capturing speed required is approximately 800 Hz when a two-frequency three-step phase-shifting technique is adopted. This research also found that, due to the optical properties of live tissue, the blue light is recommended for the measurement of live rabbit hearts since it provides the best results comparing with the green or red light.

10.2 Future Work

Throughout this dissertation research, several advancements have been made towards achieving high-speed and high-accuracy 3D shape measurement. However, there are still numerous research issues to be studied and broad applications to be explored. The potential improvements could be done in the following areas:

1. **Multi-view high-speed 3D shape measurement.** With one 3D shape measurement system, only a portion of the full 3D model can be obtained, which might not be sufficient for many applications. To reconstruct a full 360° model, multi-view high-speed 3D shape measurements are required. Since multiple systems will be adopted, there will be challenges associated with accurately calibrating multiple systems and stitching all 3D patches. Moreover, to achieve high-speed measurement, all systems must be operated in parallel, leading to the issue of avoiding the interference among all these systems.

2. **Near infrared (NIR) high-speed 3D shape measurement.** The current high-speed 3D shape measurement system uses visible light, whose measurement quality is substantially influenced by ambient light, making it difficult for out-door applications. Furthermore, it is undesirable to use white light for many applications such as capturing human faces in biometrics applications. The challenge associated with NIR system is the availability of cameras and projectors, the quality of those hardware components, and their associated costs for high-speed cases.

3. **Minimization of the high-speed 3D system.** The current high-speed 3D systems are physically large, making it difficult to be applied to space-confined applications, such as cell phones, or endoscopes. Even though efforts have been made to achieve 3D shape measurement with small-scale hardwares or with optical fibers for light transmission (Schmalza et al., 2012; Penne et al., 2009), challenges still remain on achieving high speed and high accuracy for such hardware systems.

4. **More applications.** High-speed and high-accuracy 3D shape measurement has the potential to be applied in numerous application fields. For example, in biometrics area, it can be used to capture human physical information such as finger prints or human faces. With the high-speed systems, not only static 3D information but also motion (e.g., facial expressions) can be captured, which can then be used to improve the recognition success rate. For each application area, there are some challenges. Studies still need to be performed to conquer those challenges to ensure its success of applying high-speed and high-accuracy 3D shape measurement techniques to solve for particular problems.

APPENDIX
EVALUATION OF PHASE QUALITY AT DIFFERENT DEPTHS FOR THE SBM, OPWM, AND DITHERING TECHNIQUES

In this dissertation research, several different binary defocusing techniques were examined, including the squared binary method (SBM), the optimal pulse width modulation (OPWM) method, and the binary dithering techniques. The OPWM techique and dithering technique was developed to overcome the major limitation of the SBM technique, small depth range for high-quality 3D shape measurement. This appendix provides additional experimental data to evaluate the performance of the OPWM and dithering techniques comparing against the SBM.

Experimental Results

Figure A.1 shows the experimental system setup. The system used in our experiments consists of a digital-light-processing (DLP) projector (Samsung SP-P310MEMX) and digital charge-coupled-device (CCD) camera (Jai Pulnix TM-6740CL). The camera uses a 16 mm focal length Mega-pixel lens (Computar M1614-MP). The camera resolution is 640 $\times$ 480 with a maximum frame rate of 200 frames/sec. The projector has a resolution of 800 $\times$ 600 with a projection distance of 0.49-2.80 m. The camera remains in focus all the time, and adjustments are performed when needed. However, the projector remains untouched for all the experiments to understand the defocusing effects of the binary patterns at different depth ranges.

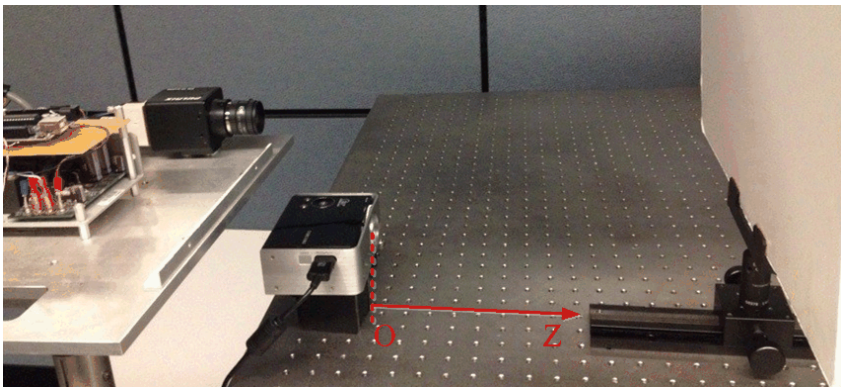

Figure A.1 The system setup.

In all the following experiments, a uniform flat white board was used for evaluation. The phase error was calculated by comparing with the ideal phase obtained from squared binary patterns using a nine-step phase-shifting algorithm with a small fringe period ($T = 18$ pixels) (Ekstrand and Zhang, 2011). In addition, the focal plane of the projector was set to be further away from the projector to emulate the real measurement conditions for the binary defocusing technique. In these experiments, the Stucki dithering technique was used for evaluation because it performs the best overall comparing with different types of binary dithering techniques.

Figure A.2 shows the captured squared binary patterns at different depths ($z = 300$ mm, 732 mm, and 1300 mm) when the fringe period is 18 pixels. As shown in Fig. A.1, the depth z starts from from the projector lens ($z = 0$ mm) and increases when it is further away from the projector. Figures 2(a) and 2(d) show that the binary pattern is significantly defocused when the board is place at $z = 300$ mm, the fringe contrast is quite low. Figure 2(c) and 2(f) show that the pattern is nearly focused when the board is placed at $z = 1300$ mm, where the binary structures are clearly visible. When the board is placed in the middle at $z = 732$ mm, the pattern is well defocused for fringe period of 18 pixels as shown in Fig. 2(b) and 2(e).

We first evaluated the performances of different binary defocusing techniques when the fringe pattern is dense (a fringe period of $T = 18$ pixels). Figure 3(a) shows the

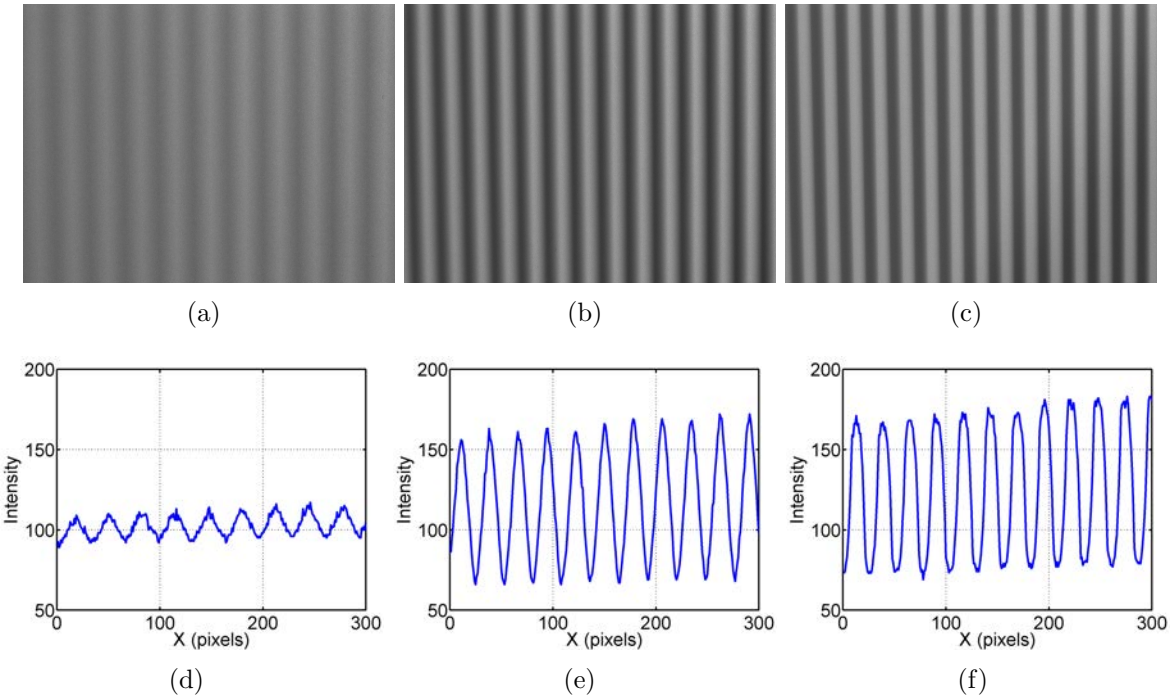

Figure A.2 The captured patterns with the fringe period of $T = 18$ pixels when the board is at different depths. (a) A captured pattern at $z = 300$ mm; (b) A captured pattern at $z = 732$ mm; (c) A captured pattern at $z = 1300$ mm; (d)-(f) are the corresponding cross sections of (a)-(c).

results when the flat board was placed at different depths (z). It should be noted that with only 18 pixels to operate, the OPWM technique yields the same pattern as square binary pattern since there are not sufficient pixels to optimize. The results show that when the fringe pattern is defocused too much, the phase error for all the methods is very large. But when the fringe pattern is nearly focused, the error becomes smaller, meaning that the phase quality is better. It is interesting to note that the SBM performs better than the dithering technique. This experiment indicates that when the fringe pattern is very dense (e.g. $T = 18$ pixels), there is no need to optimize either using the OPWM method or the dithering technique.

Experiment was also carried out for wider fringe patterns ($T = 42$ pixels) and the results are shown in Fig. 3(b). When the fringe pattern is significantly defocused, all the techniques result in moderate phase error; and the phase error slightly decreases if

the projector is more defocused. However, when the fringe pattern is nearly focused, the phase error for the SBM is significant while both of the OPWM and dithering techniques can still provide good results. The experimental result indicates the success of OPWM and dithering techniques can indeed substantially improve the depth range for high-quality 3D shape measurement.

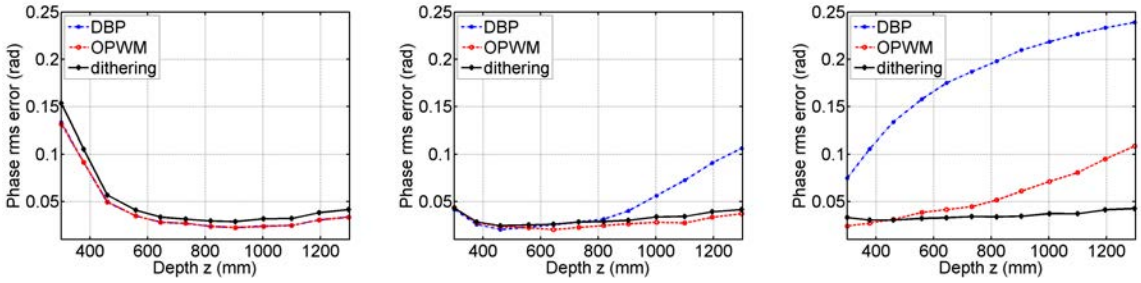

(a) (b) (c)

Figure A.3 Experimental results of the SBM, OPWM and dithering techniques when the board is at different depths. (a) $T = 18$ pixels; (b) $T = 42$ pixels; (c) $T = 150$ pixels.

We also performed experiment to evaluate the performances of these different binary techniques when the fringe period is very large ($T = 150$ pixels). Figure 3(c) shows the results. This experiment shows that the phase error is always very large for the SBM because the high-frequency harmonics cannot be properly suppressed by the defocusing effect of the projector. The OPWM technique performs the best when the fringe pattern is significantly defocused ($z < 400$ mm). However, overall, the dithering technique performs the best for the majority of measurement depth range.

Summary

In summary, the SBM performs well when the fringe period is very small (e.g. $T = 18$ pixels), and no optimization is necessary. When the fringe period increases (e.g. $T = 42$ pixels), the SBM only works well for a small depth range; and both OPWM and dithering techniques can substantially increase the depth range, while OPWM slightly performs

better than the dithering technique. When the fringe period is very large (e.g. $T = 150$ pixels), the SBM completely fails to provide reasonable quality phase, the OPWM method works well only within a small depth range, but the dithering technique can consistently provides high-quality measurement for a large depth range.

BIBLIOGRAPHY

Agelidis, V. G., Balouktsis, A., and Balouktsis, I. (2004). On applying a minimization technique to the harmonic elimilation pwm control: The bipolar waveform. *IEEE Power Electronics Letters*, 2:41–44.

Ajubi, G. A., Ayubi, J. A., Martino, J. M. D., and Ferrari, J. A. (2010). Pulse-width modulation in defocused 3-d fringe projection. *Optics Letters*, 35:3682–3684.

Bayer, B. (1973). An optimum method for two-level rendition of continuous-tone pictures. *IEEE International Conference on Communications*, 1:11–15.

Ben-Ari, R. and Raveh, G. (2011). Variational depth from defocus in real-time. *IEEE International Conference on Computer Vision Workshops*, 522–529.

Bouguet, J.-Y. Camera calibration toolbox for matlab. *Online available at: http://www.vision.caltech.edu/bouguetj/calib_doc.*

Bowen, W. J. (1949). The absorption spectra and extinction coefficients of myoglobin. *Journal of Biological Chemistry*, 179:235–245.

Calderon, H., Ortiz, J., and Fontaine, J.-G. (2010). High parallel disparity map computing on fpga. *Proceedings of the International Conference on Mechatronics and Embedded Systems and Applications (MESA)*, 307–312.

Carrihill, B. and Hummelr, R. (1985). Experiments with the intensity ratio depth sensor. *Computer Vision, Graphics, and Image Processing*, 32:337–358.

Caspi, D., Kiryati, N., and Shamir, J. (1998). Range imaging with adaptive color structured light. *IEEE Transactions on Pattern Analysis and Machine Intelligence*, 20(5):470–480.

Chen, W., Su, X., Cao, Y., Xiang, L., and Zhang, Q. (2008). Fourier transform profilometry based on a fringe pattern with two frequency components. *Optik*, 119:57–62.

Chen, Y.-S. and Chen, B.-T. (2003). Measuring of a three-dimensional surface by use of a spatial distance computation. *Applied Optics*, 42(11):1958–1972.

Cheng, Y.-Y. and Wyant, J. C. (1985). Multiple-wavelength phase shifting interferometry. *Applied Optics*, 24:804–807.

Chiang, F. K. and Treiber, J. (1970). A note on ligtenberg's reflective moiré method. *Experimental Mechanics*, 10(12):537–538.

Chiasson, J. N., Tolbert, L. M., Mckenzie, K. J., and Du, Z. (2004). A complete solution to the harmonics elimination problem. *IEEE Transactions on Power Electronics*, 19:491–498.

Chin, C. T., Lance, C., Borsboom, J., Mastik, F., Frijlink, M. E., de Jong, N., Versluis, M., and Lohse, D. (2003). Brandaris 128: A digital 25 million frames per second camera with 128 highly sensitive frames. *Review of Scientific Instruments*, 74(12):5026.

Creath, K. (1987). Step height measurement using two-wavelength phase-shifting interferometry. *Applied Optics*, 26(14):2810–2816.

Cuevas, F., Servin, M., Stavroudis, O., and Rodriguez-Vera, R. (2000). Multi-layer neural networks applied to phase and depth recovery from fringe patterns. *Optics Communications*, 181(4):239–259.

Dai, J., Li, B., and Zhang, S. High-quality fringe patterns generation using binary pattern optimization through symmetry and periodicity. *Optics and Lasers in Engineering*, 52:195-200.

D'Apuzzo, N. and Zurich, E. (2002). Modeling human faces with multi-image photogrammetry. *Proceedings of SPIE, San Jose, California*, 4661.

Davis, J., Ramamoorthi, R., and Rusinkiewicz, S. (2005). Spacetime stereo: A unifying framework for depth from triangulation. *IEEE Transactions on Pattern Analysis and Machine Intelligence*, 27(2):1–7.

Du, H. and Wang, Z. (2007). Three-dimensional shape measurement with an arbitrarily arranged fringe projection prolometry system. *Optics Letters*, 32(16):2438–2440.

Ekstrand, L. and Zhang, S. (2011). Three-dimensional profilometry with nearly focused binary phase-shifting algorithms. *Optics Letters*, 36(23):4518-4520.

Favaro, P. and Soatto, S. (2005). A geometric approach to shape from defocus. *IEEE Transactions on Pattern Analysis and Machine Intelligence*, 27(3):406–417.

Filiberto, C., Roberto, C., Dario, P., and Fulvio, R. (2009). Sensors for 3d imaging: Metric evaluation and calibration of a ccd/cmos time-of-flight camera. *Sensors*, 9(12):10080–10096.

Franca, J., Gazziro, M. A., Ide, A. N., and Saito, J. H. (2005). A 3d scanning system based on laser triangulation and variable field of view. *IEEE International Conference on Image Processing (ICIP)*, 11:I–425–8.

Fujiwara, H., Otani, Y., and Yoshizawa, T. (1996). Flatness measurement by reflection moiré technique. *Proceedings of SPIE*, 2862:172–176.

Gao, W., Wang, L., and Hu, Z. (2008). Flexible method for structured light system calibration. *Optical Engineering*, 47(8):083602.

Geng, G. (2011). Structured-light 3d surface imaging: a tutorial. *Advances in Optics and Photonics*, 3(2):128–160.

Ghiglia, D. C. and Pritt, M. D. (1998). *Two-Dimensional Phase Unwrapping: Theory, Algorithms, and Software*. John Wiley and Sons, Inc.

Gong, Y. and Zhang, S. (2010). Ultrafast 3-d shape measurement with an off-the-shelf dlp projector. *Optics Express*, 18(19):19743–19754.

Gorthi, S. and Rastogi, P. (2010). Fringe projection techniques: Whither we are? *Optics and Lasers in Engineering*, 48:133–140.

Grosse, M., Schaffer, M., Harendt, B., and Kowarschik, R. (2011). Fast data acquisition for three-dimensional shape measurement using fixed-pattern projection and temporal coding. *Optical Engineering*, 50(10):100503.

Guan, C., Hassebrook, L. G., and Lau, D. L. (2003). Composite structured light pattern for three-dimensional video. *Optics Express*, 11(5):406–417.

Guo, H., Chen, M., and Zheng, P. (2006). Least-squares tting of carrier phase distribution by using a rational function in fringe projection prolometry. *Optics Letters*, 31(24):3588–3590.

Guo, H., He, H., Yu, Y., and Chen, M. (2005). Least-squares calibration method for fringe projection profilometry. *Optical Engineering*, 44(3):033603.

Hanafi, A., Gharbi, T., and Cornu, J. (2005). In vivo measurement of lower back deformations with fourier-transform profilometry. *Applied Optics*, 44(12):2266–2273.

Harding, K. G. and Harris, J. S. (1983). Projection moiré interferometer for vibration analysis. *Applied Optics*, 22:856–861.

Heist, S., Sieler, M., Breitbarth, A., Khmstedt, P., and Notni, G. (2013). High-speed 3d shape measurement using array projection. *Proc. SPIE, Optical Measurement Systems for Industrial Inspection VIII*, 8788:15.

Horn, E. and Kiryati, N. (1999). Toward optimal structured light patterns. *Image and Vision Computing*, 17(2):87–89.

Hu, Q., Huang, P., Fu, Q., and Chiang, F. (2003). Calibration of a 3-d shape measurement system. *Optical Engineering*, 42(2):487–493.

Huang, L., Chua, P. S. K., and Asundi, A. (2010). Least-squares calibration method for fringe projection profilometry considering camera lens distortion. *Applied Optics*, 49:1539–1547.

Huang, P., Zhang, C., and Chiang, F. (2003). High-speed 3-d shape measurement based on digital fringe projection. *Optical Engineering*, 42:163–168.

Huang, P. and Zhang, S. (2006). Fast three-step phase-shifting algorithm. *Applied Optics*, 45(21):5086–5091.

Huntley, J. M. and Saldner, H. O. (1993). Temporal phase-unwrapping algorithm for automated interferogram analysis. *Applied Optics*, 32:3047–3052.

Inokuchi, S., Sato, K., and Matsuda, F. (1984). Range imaging system for 3-d object recognition. *International Conference on Pattern Recognition*, 806–808.

Jin, L., Kodera, Y., Otani, Y., and Yoshizawa, T. (2000). Shadow moiré profilometry using the phase-shifting method. *Optical Engineering*, 39(8):2119–2213.

Kite, T. D., Evans, B. L., and Bovik, A. C. (2000). Modeling and quality assessment of halftoning by error diffusion. *IEEE International Conference on Image Processing*, 9(5):909 – 922.

Kolb, A., Barth, E., and Koch, R. (2010). Time-of-flight cameras in computer graphics. *Computer Graphics Forum*, 29(1):141–159.

Kothiyal, M. P. and Delisle, C. (1985). Shearing interferometer for phase shifting interferometry with polarization phase shifter. *Applied Optics*, 24:4439–4442.

Lange, R. and Seitz, P. (2001). Solid-state time-of-flight range camera. *IEEE Journal of Quantum Electronics*, 37:390–397.

Laughner, J. I., Zhang, S., Li, H., Shao, C. C., and Efimov, I. R. (2002). Mapping cardiac surface mechanics with structured light imaging. *American Journal of Physiology - Heart and Circulatory Physiology*, 303(6):H712–H720.

Lazaros, N., Sirakoulis, G. C., and Gasteratos, A. (2008). Review of stereo vision algorithms: From software to hardware. *International Journal of Optomechatronics*, 2(4):435–462.

Legarda-Saenz, R., Bothe, T., and Juptner, W. P. (2004). Accurate procedure for the calibration of a structured light system. *Optical Engineering*, 43(2):464–471.

Lei, S. and Zhang, S. (2009). Flexible 3-d shape measurement using projector defocusing. *Optics Letters*, 34(20):3080–3082.

Lei, S. and Zhang, S. (2010). Digital sinusoidal fringe generation: defocusing binary patterns vs focusing sinusoidal patterns. *Optics and Lasers in Engineering*, 48(5):561–569.

Li, M. and Jia, Y. (2006). Stereo vision system on programmable chip (svsoc) for small robot navigation. *Proceedings of International Conference on Intelligent Robots and Systems*, 1359–1365.

Li, Y., Zhao, C., Qian, Y., Wang, H., and Jin, H. (2010). High-speed and dense three-dimensional surface acquisition using defocused binary patterns for spatially isolated objects. *Optics Express*, 18(21):21628–21635.

Li, Z., Shi, Y., Wang, C., and Wang, Y. (2008). Accurate calibration method for a structured light system. *Optical Engineering*, 47(5):053604.

Liu, K., Wang, Y., Lau, D. L., Hao, Q., and Hassebrook, L. G. (2010). Dual-frequency pattern scheme for high-speed 3-d shape measurement. *Optics Express*, 18(5):5229–5244.

Lohry, W. and Zhang, S. (2012). 3d shape measurement with 2d area modulated binary patterns. *Optics and Lasers in Engineering*, 50(7):917–921.

Lohry, W. and Zhang, S. (2013). Genetic method to optimize binary dithering technique for high-quality fringe generation. *Optics Letters*, 38(4):540–542.

Lou, Q., Ripplinger, C. M., Bayly, P. V., and Efimov, I. R. (2008). Quantitative panoramic imaging of epicardial electrical activity. *Annals of Biomedical Engineering*, 36:1649–1658.

Malacara, D., editor (2007). *Optical Shop Testing*. John Wiley and Sons, New York, 3rd edition.

Mao, X., Chen, W., and Su, X. (2007). Improved fourier-transform profilometry. *Applied Optics*, 46(5):664–668.

M.A.Sidahmed and Boraie, M. T. (1990). Dual camera calibration for 3d machine vision metrology. *IEEE Transactions on Instrumentation and Measurement*, 39:512–516.

Merner, L., Wang, Y., and Zhang, S. (2013). Accurate calibration for 3d shape measurement system using a binary defocusing technique. *Optics and Lasers in Engineering*, 51(5):514–519.

Ou, P., Li, B., Wang, Y., and Zhang, S. (2013). Flexible real-time natural 2d color and 3d shape measurement. *Optics Express*, 21(14):16736–16741.

Penne, J., Hller, K., Strmer, M., Schrauder, T., Schneider, A., Engelbrecht, R., Feussner, H., Schmauss, B., and Hornegger, J. (2009). Time-of-flight 3-d endoscopy. *Medical Image Computing and Computer-Assisted Intervention (MICCAI)*, 467–474.

Pentland, A. P. (1987). A new sense for depth of field. *IEEE Transactions on Pattern Analysis and Machine Intelligence*, 9(4):523–531.

Posdamer, J. and Altschuler, M. (1982). Surface measurement by space-encoded projected beam systems. *Computer Graphics and Image Processing*, 18(1):1–17.

Purgathofer, W., Tobler, R., and Geiler, M. (1994). Forced random dithering: improved threshold matrices for ordered dithering. *IEEE International Conference on Image Processing*, 2:1032–1035.

Quan, C., Tay, C. J., He, X. Y., Kang, X., and Shang, H. M. (2002). Microscopic surface contouring by fringe projection method. *Optics and Laser Technology*, 34(7):547–552.

Salvi, J., Pags, J., and Batlle, J. (2004). Pattern codification strategies in structured light systems. *Pattern Recognition*, 37(4):827–849.

Sansoni, G., Carocci, M., and Rodella, R. (1999). Three-dimensional vision based on a combination of gray-code and phase-shift light projection: analysis and compensation of the systematic errors. *Applied Optics*, 38(31):6565–6573.

Schaffer, M., Groβe, M., Harendt, B., and Kowarschik, R. (2013). Coherent two-beam interference fringe projection for highspeed three-dimensional shape measurements. *Applied Optics*, 52:2306–2311.

Schaffer, M., Grosse, M., Harendt, B., and Kowarschik, R. (2011). High-speed three-dimensional shape measurements of objects with laser speckles and acousto-optical deflection. *Optics Letters*, 36(16):3097–3099.

Schaffer, M., Grosse, M., and Kowarschik, R. (2010). High-speed pattern projection for three-dimensional shape measurement using laser speckles. *Applied Optics*, 49(18):3622–3629.

Schechner, Y. Y. and Kiryati, N. (1998). Depth from defocus vs. stereo: How different really are they? *Proceedings of the International Conference on Pattern Recognition*, 1784–1786.

Schmalza, C., Forster, F., Schick, A., and Angelopoulou, E. (2012). An endoscopic 3d scanner based on structured light. *Medical Image Analysis*, 16(5):1063–1072.

Schuchman, T. L. (1964). Dither signals and their effect on quantization noise. *IEEE Transactions on Communication Technology*, 12(4):162–165.

Siebert, J. P. and Marshall, S. J. (2000). Human body 3d imaging by speckle texture projection photogrammetry. *Sensor Review*, 20(3):218–226.

Sitnik, R., Ska, M. K., and Nicki, J. W. (2002). Digital fringe projection system for large volume 360-deg shape measurement. *Optical Engineering*, 41(2):443–449.

Srinivasan, V., Liu, H. C., and Halioua, M. (1984). Automated phase-measuring profilometry of 3-d diffuse objects. *Applied Optics*, 23(18):3105–3108.

Stucki, P. (1981). Mecca - A multiple-error correcting computation algorithm for bilevel image hardcopy reproduction. *Research Report, IBM Research Laboratory, Zurich, Switzerland*.

Su, X. and Chen, W. (2001). Fourier transform profilometry: a review. *Optics and Lasers in Engineering*, 35:263–284.

Su, X.-Y., Zhou, W.-S., Bally, G. V., and Vukicevic, D. (1992). Automated phase-measuring profilometry using defocused projection of a ronchi grating. *Optics Communications*, 94(13):561–573.

Subbarao, M. and Surya, G. (1994). Depth from defocus: A spatial domain approach. *International Journal of Computer Vision*, 13:271–294.

T.A.Clarke and J.G.Fryer (1998). The development of camera calibration methods and models. *Photogrammetric Record*, 16:51–66.

Towers, C. E., Towers, D. P., and Jones, J. D. (2003). Optimum frequency selection in multifrequency interferometry. *Optics Letters*, 28(11):887–889.

Tsai, R. Y. (1987). A versatile camera calibration technique for high-accuracy 3d machine vision metrology using off-the-shelf tv cameras and lenses. *IEEE Journal on Robotics and Automation*, 3:323–344.

Vo, M., Wang, Z., Pan, B., and Pan, T. (2012). Hyper-accurate exible calibration technique for fringe-projection-based three-dimensional imaging. *Optics Express*, 20(15):16926–16941.

Wang, Y., Laughner, J. I., Efimov, I. R., and Zhang, S. (2013a). 3d absolute shape measurement of live rabbit hearts with a superfast two-frequency phase-shifting technique. *Optics Express*, 21(5):5822–5632.

Wang, Y., Li, Y., Zhou, J., Zhang, J., and Fang, J. (2013b). A non-encoding structured light approach with infrared illumination for 3d large field shape measurement. *Optics and Laser Technology*, 49(0):28–32.

Wang, Y. and Zhang, S. (2010). Optimum pulse width modulation for sinusoidal fringe generation with projector defocusing. *Optics Letters*, 35(24):4121–4123.

Wang, Y. and Zhang, S. (2011). Superfast multifrequency phase-shifting technique with optimal pulse width modulation. *Optics Express*, 19(6):5143–5148.

Wang, Y. and Zhang, S. (2012a). Comparison among square binary, sinusoidal pulse width modulation, and optimal pulse width modulation methods for three-dimensional shape measurement. *Applied Optics*, 51(7):861–872.

Wang, Y. and Zhang, S. (2012b). Three-dimensional shape measurement with binary dithered patterns. *Applied Optics*, 51(27):6631–6636.

Wang, Y. and Zhang, S. (2013). Optimal fringe angle selection for digital fringe projection technique. *Applied Optics*, 52(29):7094–7098.

Watanabe, M., Nayar, S. K., and Noguchi, M. N. (1996). Real-time computation of depth from defocus. *Proceedings of SPIE: Three-Dimensional and Unconventional Imaging for Industrial Inspection and Metrology*, 2599:A–03.

Weise, T., Leibe, B., and Gool, L. V. (2007). Fast 3d scanning with automatic motion compensation. *IEEE Conference on Computer Vision and Pattern Recognition*, 1–8.

Weng, J., Cohen, P., and Herniou, M. (2010). An accurate stereo vision system using cross-shaped target self-calibration method based on photogrammetry. *Optics and Lasers in Engineering*, 48:1252–1261.

Williams, B. W. (2006). *Principles and Elements of Power Electronics*. Glasgow.

Woodll, J. I., Gordon, G., and Buck, R. (2004). Tyzx deepsea high speed stereo vision system. *Proceedings of the IEEE Conference on Computer Vision and Pattern Recognition Workshops (CVPRW04)*, 3:41–48.

Wyant, J. C. (1982). Interferometric optical metrology: basic principles and new systems. *Laser Focus*, 5:65–71.

Wyant, J. C. and Shagam, R. N. (1978). Use of electronic phase measurement techniques in optical testing. *Proceedings ICO-11*, 659–662.

Xian, T. and Su, X. (2001). Area modulation grating for sinusoidal structure illumination on phase-measuring profilometry. *Applied Optics*, 40(8):1201–1206.

Xu, Y., Ekstrand, L., Dai, J., and Zhang, S. (2011). Phase error compensation for three-dimensional shape measurement with projector defocusing. *Applied Optics*, 50(17):2572–2581.

Yang, R., Cheng, S., and Chen, Y. (2008). Flexible and accurate implementation of a binocular structured light system. *Optics and Lasers in Engineering*, 46(5):373–379.

Yang, R. and Pollefeys, M. (2003). Multi-resolution real-time stereo on commodity graphics hardware. *Proceedings of the IEEE Conference on Computer Vision and Pattern Recognition (CVPR03)*, 1:211–217.

Yin, Y., Peng, X., Li, A., Liu, X., and Gao, B. Z. (2012). Calibration of fringe projection profilometry with bundle adjustment strategy. *Optics Letters*, 37(4):542–544.

Yoshizawa, T. and Tomisawa, T. (1993). Shadow moir*é* topography by means of the phase-shift method. *Optical Engineering*, 32(7):1668–1674.

Zappa, E. and Busca, G. (2009). Fourier-transform profilometry calibration based on an exhaustive geometric model of the system. *Optics and Lasers in Engineering*, 47(7-8):754–767.

Zhang, C., Huang, P., and Chiang, F. (2002). Microscopic phase-shifting profilometry based on digital micromirror device technology. *Applied Optics*, 41(28):5896–5904.

Zhang, G., Sun, J., Chen, D., and Wang, Y. (2008). Flapping motion measurement of honeybee bilateral wings using four virtual structured-light sensors. *Sensor Actuat. A-Phys.*, 148:19–27.

Zhang, L., Snavely, N., Curless, B., and Seitz, S. M. (2004). Spacetime faces: High-resolution capture for modeling and animation. *ACM Annual Conference on Computer Graphics*, 548–558.

Zhang, Q. and Su, X. (2005). High-speed optical measurement for the drumhead vibration. *Optics Express*, 13(8):3110–3116.

Zhang, S. (2010a). Flexible 3-d shape measurement using projector defocusing: Extended measurement range. *Optics Letters*, 35(7):931–933.

Zhang, S. (2010b). Recent progresses on real-time 3-d shape measurement using digital fringe projection techniques. *Optics and Lasers in Engineering*, 48(2):149–158.

Zhang, S., editor (2013). *Handbook of 3D machine vision: Optical metrology and imaging*. CRC Press, New York, NY, 1st edition.

Zhang, S. and Huang, P. S. (2006a). High-resolution real-time three-dimensional shape measurement. *Optical Engineering*, 45(12):123601.

Zhang, S. and Huang, P. S. (2006b). Novel method for structured light system calibration. *Optical Engineering*, 45(8):083601.

Zhang, S., van der Weide, D., and Oliver, J. (2010). Superfast phase-shifting method for 3-d shape measurement. *Optics Express*, 18(9):9684–9689.

Zhang, S. and Yau, S.-T. (2006). High-resolution, real-time 3-d absolute coordinate measurement based on a phase-shifting method. *Optics Express*, 14(7):2644–2649.

Zhang, X., Lin, Y., Zhao, M., Niu, X., and Huang, Y. (2005). Calibration of a fringe projection profilometry system using virtual phase calibrating model planes. *Journal of Optics A: Pure and Applied Optics*, 7:192.

Zhang, Z. (2000). A flexible new technique for camera calibration. *IEEE Transactions on Pattern Analysis and Machine Intelligence*, 22:1330–1334.

Zuo, C., Chen, Q., Feng, S., Feng, F., Gu, G., and Sui, X. (2012). Optimized pulse width modulation pattern strategy for three-dimensional profilometry with projector defocusing. *Applied Optics*, 51(19):4477–4490.

Zuo, C., Chen, Q., Gu, G., Feng, S., Feng, F., Li, R., and Shen, G. (2013). High-speed three-dimensional shape measurement for dynamic scenes using bi-frequency tripolar pulse-width-modulation fringe projection. *Optics and Lasers in Engineering*, 51(8):953–960.